INSTITUTO SUPERIOR DE ENGENHARIA DO PORTO
MESTRADO EM ENGENHARIA MECÂNICA




Otimização estrutural computacional da estrutura do rocker bogie de um rover espacial através de métodos sem malha

JOÃO PEDRO BASÍLIO SILVA
outubro de 2025

POLITÉCNICO
DO PORTO

ISEP INSTITUTO SUPERIOR DE ENGENHARIA DO PORTO

The computational structural optimization of the rocker bogie structure of a space Rover using meshless methods

João Pedro Basílio Silva

Dissertação de

Mestrado em Engenharia Mecânica

Área de Especialização em

Construções Mecânicas

Orientador: Professor Doutor Jorge Américo de Oliveira Pinto Belinha

Coorientador: Professor Doutor Daniel Espírito Santo Rodrigues

Júri: Professor Doutor Hernâni Miguel Reis Lopes

Júri: Professor Doutor Jorge Américo de Oliveira Pinto Belinha

Júri: Professor Doutor Raul Domingos Ferreira Moreira

Porto, outubro 2025

Acknowledgements

I would like to express my sincere gratitude to my professors and thesis supervisors, Jorge Belinha, Ana Pais and Daniel Rodrigues. Their unwavering support, availability, and insightful guidance have been fundamental throughout the course of this work. Their ability to provide clarity in moments of doubt and to encourage the exploration of different perspectives not only helped me overcome obstacles but also enriched my academic and personal growth.

I would also like to acknowledge my colleague Rui Monteiro, whose companionship and readiness to assist whenever challenges arose offered me both practical help and moral support. His presence during this journey made difficult moments far more manageable and less discouraging.

Furthermore, I would like to express my heartfelt appreciation to my girlfriend and her family, whose constant care and reassurance throughout each day and every challenge strengthened my belief in the success of this thesis.

Above all, I owe my deepest gratitude to my parents and my grandmother. Their constant encouragement, belief in my abilities, and unconditional support have been the driving force that sustained me through the most demanding phases of this process. Their trust in me gave me the strength to persevere, to remain motivated, and to approach each challenge with resilience and determination.

Thank you.

Abstract

The cost of planetary missions is influenced by the mass of the components being transported into space. For this purpose, structural optimization techniques which reduce mass without compromising the mechanical performance of the component can be employed. Through finite element and meshless methods, planetary rovers can be effectively analysed and optimized, resulting in enhanced overall performance and better resilience to the extreme conditions encountered on Mars. This thesis includes a comprehensive literature review on space exploration technologies, as well as on meshless and finite element methods, with particular emphasis on the Radial Point Interpolation Method (RPIM) and the Natural Neighbours Radial Point Interpolation Method (NNRPIM). The accuracy and effectiveness of the selected methods and structural optimization techniques are validated through benchmark examples. After this validation, these methods are applied to the optimization of the suspension system of NASA's Perseverance Rover, resulting in significantly improved structural performance, including lower Von Mises stress values and increased stiffness compared to the current design. By utilizing meshless methods in the suspension system optimization and analysis, this thesis aims to contribute to ongoing and future research in structural optimization and meshless methods, thereby enriching the existing literature on the subject.

Keywords

Meshless methods; Finite element methods; Structural optimization; Perseverance Rover

Resumo

O custo das missões planetárias é influenciado pela massa dos componentes que são transportados para o espaço. Para isso, podem ser utilizadas técnicas de otimização estrutural que reduzam a massa sem comprometer o desempenho mecânico do componente. Através de elementos finitos e métodos sem malha, os rovers planetários podem ser efetivamente analisados e otimizados, resultando num melhor desempenho geral e melhor resiliência às condições extremas encontradas em Marte. Esta tese inclui uma revisão abrangente da literatura sobre tecnologias de exploração espacial, bem como métodos sem malha e de elementos finitos, com particular ênfase no Método de Interpolação de Pontos Radiais (RPIM) e no Método de Interpolação de Pontos Radiais de Vizinhos Naturais (NNRPIM). A precisão e eficácia dos métodos selecionados e técnicas de otimização estrutural são validadas através de exemplos de benchmark. Após esta validação, estes métodos são aplicados à otimização do sistema de suspensão do Perseverance Rover da NASA, resultando num desempenho estrutural significativamente melhorado, incluindo valores de tensão Von Mises mais baixos e maior rigidez em comparação com o design atual. Ao utilizar métodos sem malha na otimização e análise de sistemas de suspensão, esta tese pretende contribuir para a investigação em curso e futura relativa a otimização estrutural e métodos sem malha, enriquecendo assim a literatura existente sobre o assunto.

Palavras-chave:

Métodos sem malha; Métodos de elementos finitos; Otimização estrutural; Perseverance Rover

Index

List of Figures xi

List of Tables xvii

Acronyms and symbols xix

1. Introduction 1
   1.1. Context 1
   1.2. Motivation 1
   1.3. Objectives 2
   1.4. Structure 2
2. SPACE EXPLORATION 5
   2.1. Use of space 5
      2.1.1. Applications of space technology 5
      2.1.2. Costs 7
   2.2. Space vehicles 7
      2.2.1. Earth observation 8
      2.2.2. Communications Satellites 9
      2.2.3. Planetary Missions 9
   2.3. Space robots 10
      2.3.1. Mobility systems 10
      2.3.2. Planetary environment 15
      2.3.3. Material selection 16
   2.4. Perseverance rover 18
      2.4.1. Wheels and suspension system 19
      2.4.2. Rover speed 19
      2.4.3. Additional technology 20
3. NUMERICAL METHODS 21
   3.1. Solid mechanics fundamentals 21
      3.1.1. Stress/ principal stress 21
      3.1.2. Constitutive Equations 22
      3.1.3. Strong and weak form formulation 23
   3.2. Meshless methods 25
      3.2.1. Radial Point Interpolation Method 25
      3.2.2. Natural Neighbour Radial Point Interpolation Method 26
      3.2.3. Nodal connectivity 26
      3.2.4. Numerical integration 27
   3.3. Shape functions 31

3.4. System of equations 32
3.5. Bone remodelling 33
3.6. Bi-directional Evolutionary Structural Optimization 34

4. COMPUTATIONAL APPLICATIONS 37
4.1. Finite element method 37
4.2. Meshless methods 38
4.3. Numerical methods applied in space technology 39
4.3.1. Wheels-soil interaction 39
4.3.2. Rover Structural Components 41
4.3.3. Thermal and fluid analysis 43

5. PRELIMINARY NUMERICAL STUDIES 45
5.1. Cantilever beam 45
5.1.1. Cantilever beam 2D analysis 46
5.1.2. Cantilever beam 3D analysis 50
5.2. Structural optimization 54
5.2.1. Bone remodelling 56
5.2.2. BESO 60
5.3. Elastostatic studies 66

6. Perseverance rover rocker-bogie 73
6.1. Rocker-bogie structure 73
6.2. Rocker-bogie numerical analysis 74
6.2.1. Initial geometry and meshing 74
6.2.2. Boundary conditions 75
6.2.3. Initial structural optimization 77
6.2.4. Elastostatic studies 78
6.2.5. 3D structures 83

7. Conclusions 89
7.1. Conclusions 89
7.2. Limitations 91
7.3. Future works 91

References 93

Declaração de Integridade 97

List of Figures

Figure 1. Assimilated data from AMV'S and conventional satellites by ECMWF [1] 6
Figure 2. a) Launch cost for Mars missions converted to the fiscal year of 2022 (FY22) in USD [2]; b) Spacecraft development cost converted to the fiscal year of 2022 (FY22) in USD [2].....7
Figure 3. a) Illustration of the fixed observation interval of a CEOS [5]; b) Comparison between CEOS and AEOS [6].....8
Figure 4. CAPS concept [7].....9
Figure 5. a) Rocker-bogie suspension sketch [12]; b) Rocker-bogie suspension system [10] ... 11
Figure 6. a) Nanokhod robot [11]; b) SCORPION robot [10] 12
Figure 7. DLR in wheel mode and legged mode [10] 14
Figure 8. a) Legged-track hybrid robots [11];b) Hop-roll hybrid systems [10]..... 14
Figure 9. Critical resolved shear stress for different metallic materials, depending on the temperature [19] 17
Figure 10. Perseverance rover [23] 18
Figure 11. Comparison between Curiosity and Perseverance wheels [23] 19
Figure 12. a) Fixed rectangular shape domain. b) Fixed circular domain. c) Flexible circular domain [24] 27
Figure 13. a) First quadrilateral from the grid cell. b) isoparametric square shape from the initial quadrilateral. c) Return to the initial shape [24] 28
Figure 14. a) Voronoï cell with its intersection points. b) Middle points and the respective quadrilaterals. c) Quadrilateral generated [24] 29
Figure 15. a) Voronoï cell with its intersection points. b) Middle points and the respective triangles. c) Triangle generated [24] 29
Figure 16. Cell shapes with integration points. a) triangular. b) quadrilateral [24]..... 30
Figure 17. Gauss-Legendre integration for a) quadrilateral and b) triangular cells with 9 points each [24] 30
Figure 18. BONE remodelling algorithm [28] 34
Figure 19. BESO algorithm [29] 35
Figure 20. Finite Element Publications per year since 1966 [33] 38
Figure 21. Meshless Methods Publications per year since 1996 [37] 39
Figure 22. RPK simulation (blue) and Lagrangian simulation (green), adapted from [38] 40
Figure 23. Different computational models: a) first; b) second; c) third (adapted from[42]) ... 42
Figure 24. Different FEA analysis: a) Von Mises stress; b) Global factor of safety (adapted from [44]) 43
Figure 25. Flow velocity surrounding the rover using CFD and PIV [46] 44
Figure 26. Sketch of the Cantilever Beam 46
Figure 27. 2D Mesh divisions. a) triangular 4×2; b) quadrangular 4×2; c) triangular 8×4; d) quadrangular 8×4; e) triangular 16×8; f) quadrangular 16×8..... 47
Figure 28. a) Displacements in triangular mesh; b) Displacements in quadrangular mesh 48
Figure 29. a) $\sigma xy(x)$ in triangular mesh; b) $\sigma xy(x)$ in quadrangular mesh 48
Figure 30. a) $\sigma xx(x)$ in triangular mesh; b) $\sigma xx(x)$ in quadrangular mesh 48

Figure 31. σxx colour map; a) FEM 3n ($\sigma\max = 19.24$ MPa, $\sigma\min = -19.24$ MPa); b) FEM 4n ($\sigma\max = 19.42$ MPa, $\sigma\min = -19.42$ MPa); c) RPIM 3n ($\sigma\max = 19.07$ MPa, $\sigma\min = -19.07$ MPa); d) RPIM 4n ($\sigma\max = 19.36$ MPa, $\sigma\min = -19.36$ MPa); e) NNRPIM V1 ($\sigma\max = 19.59$ MPa, $\sigma\min = -19.59$ MPa); f) NNRPIM V2 ($\sigma\max = 19.39$ MPa, $\sigma\min = -19.39$ MPa) 49
Figure 32. τxy colour map; a) FEM 3n ($\tau min = -3.32\ Pa;\ \tau max = 0\ Pa$); b) FEM 4n ($\tau min = -4.12\ Pa;\ \tau max = 0\ Pa$); c) RPIM 3n ($\tau min = -3.85\ Pa;\ \tau max = 0\ Pa$); d) RPIM 4n ($\tau min = -4.01\ Pa;\ \tau max = 0\ Pa$); e) NNRPIM V1 ($\tau min = -4.22\ Pa;\ \tau max = 0\ Pa$); f) NNRPIM V2 ($\tau min = -3.99\ Pa;\ \tau max = 0\ Pa$) 50
Figure 33. 3D Mesh divisions. a) tetrahedral $4 \times 2 \times 2$; b) hexahedral $4 \times 2 \times 2$; c) tetrahedral $8 \times 4 \times 2$; d) hexahedral $8 \times 4 \times 2$ 51
Figure 34. a) Displacements in tetrahedral mesh; b) Displacements in hexahedral mesh 52
Figure 35. a) $\sigma xy(x)$ in tetrahedral mesh; b) $\sigma xy(x)$ in hexahedral mesh 52
Figure 36. $\sigma xx(x)$ in tetrahedral mesh; b) $\sigma xx(x)$ in hexahedral mesh 52
Figure 37. σxx colour map; a) FEM 3n ($\sigma\max = 15.52$ MPa, $\sigma\min = -15.52$ MPa); b) FEM 4n ($\sigma\max = 15.72$ MPa, $\sigma\min = -15.72$ MPa); c) RPIM 3n ($\sigma\max = 14.82$ MPa, $\sigma\min = -14.82$ MPa); d) RPIM 4n ($\sigma\max = 15.04$ MPa, $\sigma\min = -15.04$ MPa); e) NNRPIM V1 ($\sigma\max = 15.30$ MPa, $\sigma\min = -15.30$ MPa); f) NNRPIM V2 ($\sigma\max = 15.22$ MPa, $\sigma\min = -15.22$ MPa) 53
Figure 38. τxy colour map; a) FEM 3n ($\tau min = -1.975\ Pa; \tau max = 0\ Pa$); b) FEM 4n ($\tau min = -2.77\ Pa; \tau max = 0\ Pa$); c) RPIM 3n ($\tau min = -2.44\ Pa; \tau max = 0\ Pa$); d) RPIM 4n ($\tau min = -2.72\ Pa; \tau max = 0\ Pa$); e) NNRPIM V1 ($\tau min = -2.67\ Pa; \tau max = 0\ Pa$); f) NNRPIM V2 ($\tau min = -2.56\ Pa; \tau max = 0\ Pa$) 54
Figure 39. Structural optimization study full beam 55
Figure 40. Structural optimization study beam 55
Figure 41. Benchmark beam results [47] 55
Figure 42. Bone remodelling FEM analysis 56
Figure 43. Bone remodelling RPIM analysis 57
Figure 44. Bone remodelling NNRPIM V1 analysis 57
Figure 45. Bone remodelling NNRPIM V2 analysis 58
Figure 46. Bone remodelling for FEM analysis 59
Figure 47. Bone remodelling for RPIM analysis 59
Figure 48. Bone remodelling for NNRPIM V1 analysis 60
Figure 49. Bone remodelling for NNRPIM V2 analysis 60
Figure 50. Simply supported beam FEM BESO analysis 61
Figure 51. Simply supported beam RPIM BESO analysis 62
Figure 52. Simply supported beam NNRPIM V1 BESO analysis 62
Figure 53. Simply supported beam NNRPIM V2 BESO analysis 63
Figure 54. Fully supported beam FEM BESO analysis 63
Figure 55. Fully supported beam RPIM BESO analysis 64
Figure 56. Fully supported beam NNRPIM V1 BESO analysis 64
Figure 57. Fully supported beam NNRPIM V2 BESO analysis 65

Figure 58. a) FEM (90x30;0.02) study with a 10 iteration interval; b) FEM (90x30;0.02) study with a 30 iteration interval 65
Figure 59. a) RPIM (90x30;0.02) study with a 10 iteration interval; b) RPIM (90x30;0.02) study with a 30 iteration interval 66
Figure 60. FEM Simply supported beam; a) FEM ($\sigma ef\ max = 3.92\ \times 106\ Pa;\ \sigma ef\ min = 2.09\ \times 104\ Pa$); b) RPIM ($\sigma ef\ max = 3.97\ \times 106\ Pa;\ \sigma ef\ min =\ 1.40\ \times 104\ Pa$); c) NNRPIM V1 ($\sigma ef\ max = 3.43\ \times 106\ Pa;\ \sigma ef\ min = 1.48\ \times 104\ Pa$); d) NNRPIM V2 ($\sigma ef\ max = 3.35\ \times 106\ Pa;\ \sigma ef\ min = 1.42\ \times 104\ Pa$) 67
Figure 61. FEM Simply supported beam. a) FEM ($umax = 0;\ umin = -6.78 \times 10 - 5\ m$); b) RPIM ($umax = 0;\ umin = -6.82 \times 10 - 5\ m$); c) NNRPIM V1 ($umax = 0;\ umin = -6.81 \times 10 - 5\ m$); d) NNRPIM V2 ($umax = 0;\ umin = -6.77 \times 10 - 5\ m$) 67
Figure 62. RPIM Simply supported beam; a) FEM ($\sigma ef\ max = 3.89\ \times 106\ Pa;\ \sigma ef\ min = 8.63\ \times 103\ Pa$); b) RPIM ($\sigma ef\ max = 4.12\ \times 106\ Pa;\ \sigma ef\ min = 7.00\ \times 103\ Pa$); c) NNRPIM V1 ($\sigma ef\ max = 3.67\ \times 106\ Pa;\ \sigma ef\ min =\ 9.84\ \times 103\ Pa$); d) NNRPIM V2 ($\sigma ef\ max = 3.55\ \times 106\ Pa;\ \sigma ef\ min =\ 1.05\ \times 104\ Pa$) 68
Figure 63. RPIM Simply supported beam. a) FEM ($umax = 0;\ umin = -7.19 \times 10 - 5\ m$); b) RPIM ($umax = 0;\ umin = -7.24 \times 10 - 5\ m$); c) NNRPIM V1 ($umax = 0;\ umin = -7.23 \times 10 - 5\ m$); d) NNRPIM V2 ($umax = 0;\ umin = -7.20 \times 10 - 5\ m$) 68
Figure 64. NNRPIM V1 Simply supported beam; a) FEM ($\sigma ef\ max = 3.91\ \times 106\ Pa;\ \sigma ef\ min = 1.12\ \times 104\ Pa$); b) RPIM ($\sigma ef\ max = 4.00\ \times 106\ Pa;\ \sigma ef\ min = 1.18\ \times 104\ Pa$); c) NNRPIM V1 ($\sigma ef\ max = 3.53\ \times 106\ Pa;\ \sigma ef\ min = 9.51\ \times 103\ Pa$); d) NNRPIM V2 ($\sigma ef\ max = 3.42\ \times 106\ Pa;\ \sigma ef\ min = 7.87\ \times 103\ Pa$) 69
Figure 65. NNRPIM V1 Simply supported beam. a) FEM ($umax = 0;\ umin = -6.38 \times 10 - 5\ m$); b) RPIM ($umax = 0;\ umin = -6.42 \times 10 - 5\ m$); c) NNRPIM V1 ($umax = 0;\ umin = -6.42 \times 10 - 5\ m$); d) NNRPIM V2 ($umax = 0;\ umin = -6.39 \times 10 - 5\ m$) 69
Figure 66. NNRPIM V2 Simply supported beam; a) FEM ($\sigma ef\ max = 3.95\ \times 106\ Pa;\ \sigma ef\ min = 1.48\ \times 104\ Pa$); b) RPIM ($\sigma ef\ max = 4.24\ \times 106\ Pa;\ \sigma ef\ min = 1.19\ \times 104\ Pa$); c) NNRPIM V1 ($\sigma ef\ max = 3.74\ \times 106\ Pa;\ \sigma ef\ min = 1.52\ \times 104\ Pa$); d) NNRPIM V2 ($\sigma ef\ max = 3.59\ \times 106\ Pa;\ \sigma ef\ min = 1.26\ \times 104\ Pa$) 70
Figure 67. NNRPIM V2 Simply supported beam. a) FEM ($umax = 0;\ umin = -8.92 \times 10 - 5\ m$); b) RPIM ($umax = 0;\ umin = -8.97 \times 10 - 5\ m$); c) NNRPIM V1 ($umax = 0;\ umin = -8.96 \times 10 - 5\ m$); d) NNRPIM V2 ($umax = 0;\ umin = -8.90 \times 10 - 5\ m$) 70
Figure 68. Fully supported beam; a) FEM ($\sigma ef\ max = 5.28\ \times 106\ Pa;\ \sigma ef\ min = 1.89\ \times 104\ Pa$); b) RPIM ($\sigma ef\ max = 6.31\ \times 106\ Pa;\ \sigma ef\ min = 1.62\ \times 104\ Pa$); c) NNRPIM V1 ($\sigma ef\ max = 7.12\ \times 106\ Pa;\ \sigma ef\ min =\ 1.52\ \times 104\ Pa$); d) NNRPIM V2 ($\sigma ef\ max = 6.63\ \times 106\ Pa;\ \sigma ef\ min =\ 1.62\ \times 104\ Pa$) 71
Figure 69. Fully supported beam. a) FEM ($umax = 0;\ umin = -4.54 \times 10 - 5\ m$); b) RPIM ($umax = 0;\ umin = -4.59 \times 10 - 5\ m$); c) NNRPIM V1 ($umax = 0;\ umin = -4.65 \times 10 - 5\ m$); d) NNRPIM V2 ($umax = 0;\ umin = -4.58 \times 10 - 5\ m$) 71
Figure 70. Initial geometry dimensions sketch 74
Figure 71. a) Initial rectangular geometry; b) Non-removable region 75

Figure 72. Bogie force distribution..... 76
Figure 73. Rocker force distribution 76
Figure 74. Force distribution sketch..... 77
Figure 75. Structure with full reactions a) Bone Remodelling ($\rho ef\ max = 4.43g/cm3;\ \rho ef\ min = 0g/cm3$); b) BESO ($\rho ef\ max = 4.43g/cm3;\ \rho ef\ min = 0\ g/cm3$)... 78
Figure 76. Structure without the x-direction reactions a) Bone Remodelling ($\rho ef\ max = 4.43g/cm3;\ \rho ef\ min = 0g/cm3$); b) BESO ($\rho ef\ max = 4.43g/cm3;\ \rho ef\ min = 0g/cm3$)..... 78
Figure 77. BONE with both reactions (Von Misses stress). a) FEM ($\sigma ef\ max = 3.86 \times 106\ Pa;\ \sigma ef\ min = 1.67 \times 104\ Pa$); b) RPIM ($\sigma ef\ max = 3.82 \times 106\ Pa;\ \sigma ef\ min = 1.93 \times 104\ Pa$); c) NNRPIM V1 ($\sigma ef\ max = 3.85 \times 106\ Pa;\ \sigma ef\ min = 1.94 \times 104\ Pa$); d) NNRPIM V2 ($\sigma ef\ max = 3.91 \times 106\ Pa;\ \sigma ef\ min = 1.90 \times 104\ Pa$)..... 79
Figure 78. BONE with both reactions (Displacements). a) FEM ($umax = 0;\ umin = -2.18 \times 10 - 3m$); b) RPIM ($umax = 0;\ umin = -2.61 \times 10 - 3m$); c) NNRPIM V1 ($umax = 0;\ umin = -2.78 \times 10 - 3m$); d) NNRPIM V2 ($umax = 0;\ umin = -2.45 \times 10 - 3m$) 79
Figure 79. BONE with vertical reactions (Von Misses stress). a) FEM ($\sigma ef\ max = 6.25 \times 106\ Pa;\ \sigma ef\ min = 4.06 \times 104\ Pa$); b) RPIM ($\sigma ef\ max = 7.20 \times 106\ Pa;\ \sigma ef\ min = 4.58 \times 104\ Pa$); c) NNRPIM V1 ($\sigma ef\ max = 6.61 \times 106\ Pa;\ \sigma ef\ min = 2.21 \times 104\ Pa$); d) NNRPIM V2 ($\sigma ef\ max = 7.09 \times 106\ Pa;\ \sigma ef\ min = 4.72 \times 104\ Pa$)..... 80
Figure 80. BONE with vertical reactions (Displacements). a) FEM ($umax = 0;\ umin = -2.35 \times 10 - 5m$); b) RPIM ($umax = 0;\ umin = -2.40 \times 10 - 5m$); c) NNRPIM V1 ($umax = 0;\ umin = -2.40 \times 10 - 5m$); d) NNRPIM V2 ($umax = 0;\ umin = -2.30 \times 10 - 5m$) 80
Figure 81. BESO with vertical reactions (Von Misses stress). a) FEM ($\sigma ef\ max = 4.27 \times 106\ Pa;\ \sigma ef\ min = 1.47 \times 104\ Pa$); b) RPIM ($\sigma ef\ max = 3.59 \times 106\ Pa;\ \sigma ef\ min = 6.36 \times 103\ Pa$); c) NNRPIM V1 ($\sigma ef\ max = 3.95 \times 106\ Pa;\ \sigma ef\ min = 1.67 \times 104\ Pa$); d) NNRPIM V2 ($\sigma ef\ max = 3.47 \times 106\ Pa;\ \sigma ef\ min = 2.01 \times 104\ Pa$)..... 81
Figure 82. BESO with vertical reactions (Displacements). a) FEM ($umax = 0;\ umin = -2.32 \times 10 - 5m$); b) RPIM ($umax = 0;\ umin = -2.40 \times 10 - 5m$); c) NNRPIM V1 ($umax = 0;\ umin = -2.50 \times 10 - 5m$); d) NNRPIM V2 ($umax = 0;\ umin = -2.40 \times 10 - 5m$) 81
Figure 83. Original suspension system. a) FEM ($\sigma ef\ max = 1.39 \times 107\ Pa;\ \sigma ef\ min = 1.54 \times 104\ Pa$); b) RPIM ($\sigma ef\ max = 1.55 \times 107\ Pa;\ \sigma ef\ min = 2.66 \times 104\ Pa$); c) NNRPIM V1 ($\sigma ef\ max = 1.28 \times 107\ Pa;\ \sigma ef\ min = 2.28 \times 104\ Pa$); d) NNRPIM V2 ($\sigma ef\ max = 1.40 \times 107\ Pa;\ \sigma ef\ min = 2.48 \times 104\ Pa$)..... 82
Figure 84. Original suspension system displacements. a) FEM ($umax = 0;\ umin = -3.39 \times 10 - 4m$); b) RPIM ($umax = 0;\ umin = -3.66 \times 10 - 4m$); c) NNRPIM V1 ($umax = 0;\ umin = -3.76 \times 10 - 4m$); d) NNRPIM V2 ($umax = 0;\ umin = -3.58 \times 10 - 4m$) 82
Figure 85. BONE with both reactions (Von Misses stress). a) FEM ($\sigma ef\ max = 3.96 \times 106\ Pa;\ \sigma ef\ min = 1.35 \times 104\ Pa$); b) RPIM ($\sigma ef\ max = 4.02 \times 106\ Pa;\ \sigma ef\ min = 1.70 \times 104\ Pa$); c) NNRPIM V1 ($\sigma ef\ max = 4.01 \times 106\ Pa;\ \sigma ef\ min = 1.88 \times 104\ Pa$); d) NNRPIM V2 ($\sigma ef\ max = 3.75 \times 106\ Pa;\ \sigma ef\ min = 1.61 \times 104\ Pa$)..... 84

Figure 86. BONE with both reactions (Displacements). a) FEM ($umax = 0$; $umin = -2.12 \times 10 - 3m$); b) RPIM ($umax = 0$; $umin = -2.60 \times 10 - 3m$); c) NNRPIM V1 ($umax = 0$; $umin = -2.68 \times 10 - 3m$); d) NNRPIM V2 ($umax = 0$; $umin = -2.53 \times 10 - 3m$) 84
Figure 87. BONE with vertical reactions (Von Misses stress). a) FEM ($\sigma ef\ max = 6.27 \times 106\ Pa$; $\sigma ef\ min = 3.27 \times 104\ Pa$); b) RPIM ($\sigma ef\ max = 8.82 \times 106\ Pa$; $\sigma ef\ min = 1.71 \times 104\ Pa$); c) NNRPIM V1 ($\sigma ef\ max = 7.90 \times 106\ Pa$; $\sigma ef\ min = 2.78 \times 104\ Pa$); d) NNRPIM V2 ($\sigma ef\ max = 6.38 \times 106\ Pa$; $\sigma ef\ min = 1.38 \times 104\ Pa$)..... 85
Figure 88. BONE with vertical reactions (Displacements). a) FEM ($umax = 0$; $umin = -2.49 \times 10 - 5m$); b) RPIM ($umax = 0$; $umin = -2.50 \times 10 - 5m$); c) NNRPIM V1 ($umax = 0$; $umin = -2.50 \times 10 - 5m$); d) NNRPIM V2 ($umax = 0$; $umin = -2.40 \times 10 - 5m$) 85
Figure 89. BESO with vertical reactions (Von Misses stress). a) FEM ($\sigma ef\ max = 4.24 \times 106\ Pa$; $\sigma ef\ min = 1.24 \times 104\ Pa$); b) RPIM ($\sigma ef\ max = 3.86 \times 106\ Pa$; $\sigma ef\ min = 1.32 \times 104\ Pa$); c) NNRPIM V1 ($\sigma ef\ max = 3.80 \times 106\ Pa$; $\sigma ef\ min = 1.39 \times 104\ Pa$); d) NNRPIM V2 ($\sigma ef\ max = 3.44 \times 106\ Pa$; $\sigma ef\ min = 1.69 \times 104\ Pa$)..... 86
Figure 90. BESO with vertical reactions (Displacements). a) FEM ($umax = 0$; $umin = -2.47 \times 10 - 5m$); b) RPIM ($umax = 0$; $umin = -2.50 \times 10 - 5m$); c) NNRPIM V1 ($umax = 0$; $umin = -2.60 \times 10 - 5m$); d) NNRPIM V2 ($umax = 0$; $umin = -2.40 \times 10 - 5m$) 86
Figure 91. Original suspension system. a) FEM ($\sigma ef\ max = 1.32 \times 107\ Pa$; $\sigma ef\ min = 1.44 \times 104\ Pa$); b) RPIM ($\sigma ef\ max = 1.44 \times 107\ Pa$; $\sigma ef\ min = 1.86 \times 104\ Pa$); c) NNRPIM V1 ($\sigma ef\ max = 1.45 \times 107\ Pa$; $\sigma ef\ min = 1.68 \times 104\ Pa$); d) NNRPIM V2 ($\sigma ef\ max = 1.39 \times 107\ Pa$; $\sigma ef\ min = 2.06 \times 104\ Pa$)..... 87
Figure 92. Original 3D suspension system displacements. a) FEM ($umax = 0$; $umin = -3.43 \times 10 - 4m$); b) RPIM ($umax = 0$; $umin = -3.90 \times 10 - 4m$); c) NNRPIM V1 ($umax = 0$; $umin = -4.02 \times 10 - 4m$); d) NNRPIM V2 ($umax = 0$; $umin = -3.85 \times 10 - 4m$) 87

List of Tables

Table 1. Launches of mobile robots [10] 15
Table 2. Coordinates 46
Table 3. Divisions and number of nodes 47
Table 4. Divisions of the 3D analysis, thickness and number of nodes 50
Table 5. Structure stiffness values 72
Table 6. Mechanical properties of Ti-6Al-4V STA [48][49] 73
Table 7. Suspension systems normalized stiffnesses 83
Table 8. 3D Suspension systems normalized stiffnesses 88
Table 9. Percentual difference between stiffnesses 88

Acronyms and symbols

List of Acronyms

ABS	*Acrylonitrile butadiene styrene*
AEOS	*Agile Earth Observation Satellite*
AMV	*Atmospheric Motion Vectors*
CAD	*Computer-Aided Design*
CAPS	*Chinese Area Positioning System*
CEOS	*Conventional Earth Observation Satellites*
CFD	*Computational Fluid Dynamics*
DARPA	*Defense Advanced Research Projects Agency*
DC	*Direct Current*
DEM	*Discrete Element Method*
DLR	*German Aerospace Center*
DR	*Decrease Ratio*
ECMWF	*European Centre for Medium-range Weather Forecast*
EDUSAT	*Educational Satellite*
EFGM	*Element-Free Galerkin Method*
EO	*Earth Observation*
ESA	*European Space Agency*
FEA	*Finite Element Analysis*
FEM	*Finite Element Method*
GEO	*Geostationary Orbits*
GLONASS	*Global Navigation Satellite System*
GNSS	*Global Navigation Satellite Systems*
GPS	*Global Positioning System*
ISEP	Instituto Superior de Engenharia do Porto
JAXA	*Japan Aerospace Exploration Agency*
JPL	*Jet Propulsion Laboratory*
LEO	*Low Earth orbits*
LPS	*Laser Power Supply*
MEDA	*Mars Environmental Dynamics Analyzer*

MER	*Mars Exploration Rovers*
MIT	*Massachusetts Institute of Technology*
MLPG	*Local Petrov-Galerkin Method*
MMs	*Meshless Methods*
MQ-RBF	*Multiquadric Radial Basis Function*
MSLS	*Mars Science Laboratory*
NASA	*National Aeronautics and Space Administration*
NEM	*Natural Element Method*
NNRPIM	*Natural Neighbour Radial Point Interpolation Method*
OTW	*Observation Time Window*
P.Porto	Instituto Politécnico do Porto
PDE	*Partial Differential Equations*
PIM	*Point Interpolation Method*
PIV	*Particle Image Velocimetry*
PRN	*Pseudorandom Noise*
PWA	*Printed Wiring Assembly*
PWB	*Printed Wiring Board*
RBF	*Radial Basis Function*
RKPM	*Reproducing Kernel Particle Method*
RPIM	*Radial Point Integration Method*
SAR	*Search and Rescue*
SIS	*Secondary Injector System*
SPH	*Smooth Particle Hydrodynamics*
UV	*Ultraviolet*
VTW	*Visible Time Window*

List of Symbols

m	Mass
T	Temperature
$\boldsymbol{\sigma}$	Stress tensor
$\boldsymbol{\varepsilon}$	Strain tensor
$\boldsymbol{c}$	Constitutive matrix
E	Young's elastic modulus
L	Lagrangian function

T	Kinetic Energy
V_i	Voronoï Cell
U	Strain energy
x_C	Centre of each geometric shape
$\boldsymbol{X}$	Nodal Coordinates Vector
W_f	Work created by external forces
Ω	Space Domain
$\boldsymbol{u}$	Displacement vector
$\boldsymbol{b}$	Body forces
ρ	Density
$\bar{\boldsymbol{t}}$	Traction on the natural boundary
$\boldsymbol{d}$	Dimensions
$\boldsymbol{k}$	Scaling factor
F	Force
$\widehat{w_i}$	Weight of the integration point
n	Number of nodes inside the influence domain
A_{V_I}	Size of the Voronoï cell
S_{Ii}	Quadrilateral sub-cells
$\boldsymbol{p}(\boldsymbol{x}_I)$	PBF vector
M_{Ii}	Middle point
Γ_t	Essential domain
Φ	Interpolation function

1. Introduction

This chapter provides context on the topic under discussion, aiming to guide the reader through the thesis. It outlines the objectives of the report and the motivations behind it. Finally, the structure of the monograph is presented to facilitate its reading. At the beginning of each chapter, a brief description of its content is provided.

1.1. Context

Numerical methods have become indispensable tools in mechanical engineering, particularly over the past century, due to significant technological advancements. These methods enable engineers to simulate real-world mechanical behaviours under specific boundary conditions and loads, leading to more accurate, efficient and cost-effective designs. Among these methods, the Finite Element Method (FEM) remains the most widely used due to is versatility and reliability. However, FEM can face challenges when dealing with highly complex geometries, which has led to the development of meshless methods, such as the Radial Point Interpolation Method (RPIM) and the Natural Neighbour radial Point Interpolation Method (NNRPIM). These newer approaches offer great modelling flexibility and accuracy in certain scenarios.

The present work focuses on the structural optimization of the suspension system of NASAs' Perseverance Rover, a subsystem responsible for maintaining stability, load distribution and terrain adaptability during planetary exploration. Although, the rovers' current suspension system has succeeded in previous missions, it still leaves room for improvement in terms of stress distribution and stiffness. Given the extreme operating conditions on Mars, including high impact loads and uneven terrain, optimizing this structure can lead to lower Von Misses stress values and improved stiffness. With the application of numerical methods, this work aims to redesign and optimize the suspension system by reducing the maximum Von Misses stress values without compromising structural integrity.

1.2. Motivation

The motivation behind this thesis arises primarily from a limited number of studies currently available in the literature that focus on the specific topic addressed in this work. This lack of research highlights a clear gap in the field and clarifies the need for further investigation and

development. By contributing to an underexplored area, this thesis aims to provide valuable insights and lay the groundwork for future advancements.

In addition, a key motivating factor is the possibility to significantly reduce the costs associated with the construction and launch of the Rover. Usually the global cost of the Rover can be expensive ($2.4 billion), therefore, if the suspension system could be redesigned and optimized into a more cost-effective design without compromising its safety under loading conditions could have substantial benefits, not only for the scientific community, enabling more frequent research mission, but also for the industry that opens new horizons for commercial applications of robotic mobility systems as well as bringing down the cost of the Rover.

1.3. Objectives

The main objective of this thesis is to explore the structural optimization of a suspension system used in the NASA Perseverance Rover. Even though the previous design proved to be reliable in severe working conditions, further structural analysis through novel numerical methods offer new opportunities to potential improvements. Primarily it is necessary to validate both the FEM, and the meshless methods approaches with the assistance of benchmark examples. Then, utilizing the same procedure, the goal is to generate more stable, efficient and mechanically robust configurations. The work focusses not only on achieving a structure with a lower maximum Von misses stress than the original but also investigating more complex geometries that can enhance the overall structure. The specific objectives are as follows:

- Validate different study approaches trough benchmark examples;
- Evaluate the potential for improvements in the existing suspension system;
- Design optimized structures with reduced Von misses stress values for improved durability and performance;
- Explore more complex geometries with greater stability.

1.4. Structure

The structure of this report is organized into chapters, each addressing a specific aspect of the research for clarity and coherence. The report begins with an **Introduction**, where the context, objectives and the structure of the work are presented to provide the reader with an overview of the research's scope. The second chapter, **Space exploration**, delves into the technological and scientific aspects of space studies. It covers space vehicles, their mobility systems, materials, and specific applications, including a detailed analysis of the Perseverance Rover. The chapter, **Numerical Methods**, discusses the theoretical foundations of solid mechanics, introduces meshless methods and explores their mathematical formulation, nodal connectivity, numerical integration and system of equations. The next chapter, **Computational applications**, provides a comprehensive review of the evolution and application of numerical methods, such

as finite elements and meshless methods, within the field of space technology. It includes case studies on computational simulations related to space vehicles. In the fifth chapter **Preliminary Numerical Studies**, a cantilever beam is analysed in order to prove that the methods utilized are coherent and the results obtained corresponded to the benchmark results. Moreover, the optimization methods (BONE and BESO) are also considered when structurally optimizing a benchmark example. The sixth chapter, **Perseverance Rover rocker-bogie**, further details the suspensions system structure, as well as its materials, dimensions and acting reactions. This chapter also aims to analyse the possibility to improve the structure of the system and deciding whether the original structure is optimal or not. The final chapter, **Conclusions**, summarizes the key findings and conclusions related to the research work as well as the limitations encountered throughout the work process and some future work that could be done.

2. SPACE EXPLORATION

This chapter discusses the development of space exploration and related technologies by humans, considering both scientific and economic perspectives. Topics such as how Earth is viewed from space, the various types of rovers and spacecraft used in missions, and some challenges encountered by space robots will be explored. Furthermore, the chapter explains the functioning and structure of the Perseverance Rover, which is the central focus of this research work.

2.1. Use of space

The starting point of space exploration was the interest in using space for economic benefits as well as scientific studies. The United States and the Soviet Union made significant investments in space technologies, which led to the development of studies, practices, and technologies. They also benefited from space exploration, due to military objectives [1]. Today, space and its technologies are applied in many other areas, because of all the discoveries and improvements made over time.

2.1.1. Applications of space technology

There are various uses of space technology, and some go well beyond its initial objectives. Space applications such as communication satellites, weather forecasting, and Global Positioning System (GPS) navigation have revolutionized daily life on Earth.

2.1.1.1. Operational Meteorology

In 1960, TIROS-1 was launched to provide weather forecasters with more accurate data using space observations. This was the first weather satellite [1]. Nowadays, seven countries and regions (Europe counting as one), possess a group of satellites, consistently tracing Earth's weather from two main orbits, with them being near polar orbits (about 900 km altitude) and geosynchronous orbits (36,000 km above the Earth). According to Figure 1, satellites produced significantly more data per 24-hour period than conventional data, due to the fact that satellites have a higher dominance of usage. When analysing the graph shown in Figure 1, it possible to observe that conventional data is assisted by Atmospheric Motion Vectors (AMVs) that determine wind patterns by tracking cloud movement. The European Centre for Medium-range Weather Forecast (ECMWF) stated that without the inclusion of the AMVs, conventional data

would be even inferior, making conventional forecast data rather worthless. ECMWF also stated that, even with the addition of AMVs, satellite data has shown to be much more precise, than the conventional data [1]. Therefore, the use of satellites to forecast weather has become significantly superior, so has the data quantity that they produce, due to the fact that they present results with better accuracy compared to Conventional and AMVs [1].

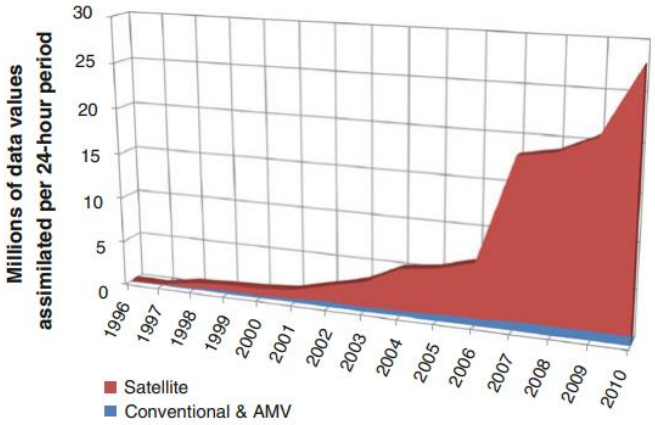

Figure 1. Assimilated data from AMV'S and conventional satellites by ECMWF [1]

2.1.1.2. Education

In addition to serving as a source of inspiration for students, space technologies play a vital role in education, particularly through telecommunications. Poor countries, for instance, India, have greatly benefited from the use of satellites. Such technologies allowed schools across remote and dispersed regions to connect with other schools around the globe [1]. In 2004, following the success previously obtained, the launch of the Education Satellite (EDUSAT) (GSAT-3) took place. This satellite was specifically designed to facilitate educational connectivity throughout the subcontinent, however, EDUSAT is still a long-term mission to enhance education through space technology [1].

2.1.1.3. Global Navigation Satellite System

Several governments around the world have invested in satellite-based navigation and non-military users globally benefit from the free availability of signals from Global Navigation Satellite Systems (GNSS). GNSS receivers have become commonplace in mass-market devices, often integrated within multipurpose gadgets such as smartphones [1]. However, many are specifically built for vehicles, incorporating general-purpose processors that support digital maps, algorithms that allow route planning, points of interest, and many other useful features. The appeal of satellite navigation systems lies in several key features, including the fact that it is a free service, although it is financed through military budgets or large-scale contracts, and the privacy of the user is secured since GPS is a receive-only product/service [1].

2.1.1.4. Search and Rescue (SAR)

Around a dozen polar orbiting satellites are currently equipped to pick up emergency signals from Cospas-Sarsat beacons. While most emergencies occur at sea, there are a lot of incidents involving individuals in distress on land or aircraft. To be rescued, ships, planes and other users must purchase specialized beacons, mandatory in certain cases. When Cospas-Sarsat detects an alert, it relays the information to SAR authorities across the 41 member countries [1].

2.1.2. Costs

Over the years, and all the missions carried out to study Mars's surface, many scientific discoveries and developments have been made. The development of these missions (formulation and implantation) ranged from large-scale and high-budget projects such as the Viking 1 and 2 missions (1970), which cost $6.2 billion for two lander and orbiters, to more recent initiatives like the Perseverance costing $2.4 billion [2], shown in Figure 2a). Across the years, missions with more moderate budgets took place for example Phoenix (costing around $441 million) and InSight (around $683 million). When analysing the graph presented in Figure 2b) it is examined that the costs of development of spacecrafts, particularly for missions with a longer duration have been reduced. The cheapest mission recorded was the Pathfinder mission to Mars with a budget of $371 million. The costs of launching are expressed in Figure 2b), and according to the graph it is possible to observe that the potential range cost of launching of the 2030s and 2040s will be reduced.

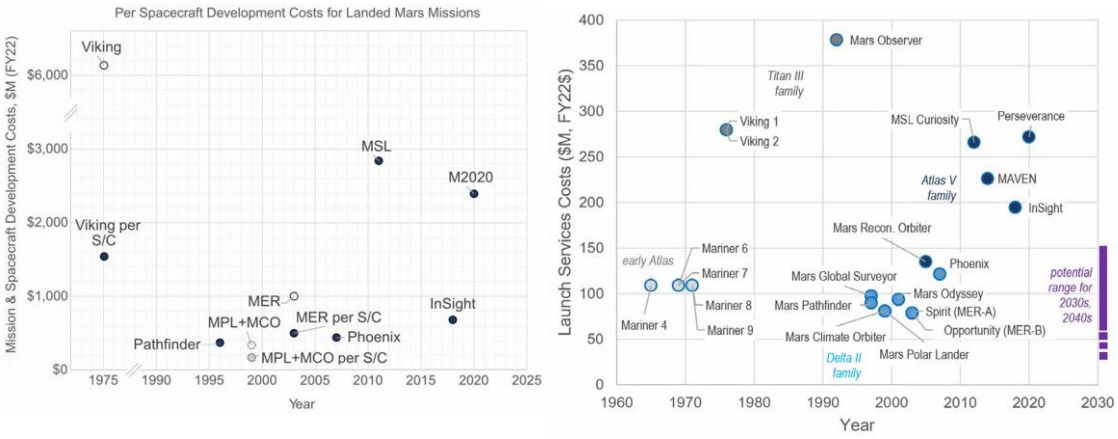

a) b)

Figure 2. a) Spacecraft development cost converted to the fiscal year of 2022 (FY22) in USD[2]; b) Launch cost for Mars missions converted to the fiscal year of 2022 (FY22) in USD [2]

2.2. Space vehicles

Space vehicles are intrinsically linked to the specific mission they are intended to perform. For instance, their requirements are dictated by the type and the objectives of the mission. Key challenges in space vehicles include propulsion, thermal protection and life support systems, all

of which must be optimized to operate in space extreme environments [3]. Outlined here are the primary types of spacecrafts along with their focus.

2.2.1. Earth observation

Earth observation missions range from scientific research to practical applications to analyse the Earth's surface, atmosphere, and magnetic field. These missions often utilize Low Earth Orbits (LEO) for optimal data collection and observation [3]. Polar and sun-synchronous orbits are commonly employed for comprehensive coverage, usually for weather and military applications. Earth observation (EO) satellites play an important role in monitoring the Earth's ecosystems, such as land, oceans and atmosphere, providing crucial data for environmental management and sustainable development [4]. The first EO satellite, Vanguard 2, was launched in 1959 with the purpose to study cloud cover. EO satellite data is extensively applied across various research fields, particularly for environmental studies, where its measurements are essential. Such satellite data is also essential in areas such as education, forestry, ecosystem services, agriculture, geology, and public health. A distinct type of satellite, known as Agile Earth Observation Satellite (AEOS), offers greater flexibility and capabilities compared to conventional systems [5]. The AEOS, with enhanced attitude control across three axes, represents the next generation of Earth observation systems. Unlike Conventional Earth Observation Satellites (CEOS), which can only adjust along the roll axis, AEOS offers improved scheduling efficiency when it comes to observation tasks. As shown in Figure 3a), CEOS are limited to observing a target during a fixed visible time window, which is determined by the satellite orbit. In contrast, AEOS can perform multiple observations within an extended visible time window, provided that all operational constraints are satisfied [5].

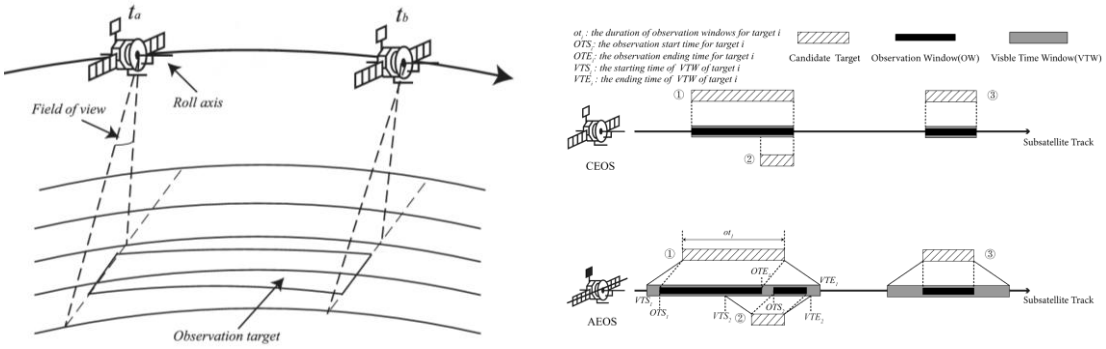

a) b)

Figure 3. a) Illustration of the fixed observation interval of a CEOS [5]; b) Comparison between CEOS and AEOS [6]

Figure 3b) highlights the key differences between CEOS and AEOS observation capabilities. For CEOS, the Observation Time Window (OTW) is identical to the Visible Time Window (VTW). However, AEOS benefit from a longer VTW due to the fact that they can adjust its pitch axis to observe ahead or behind, allowing for more flexible observation times [6].

2.2.2. Communications Satellites

Communications satellites are commonly placed in geostationary orbits (GEO) because this provides broad coverage and allows for continuous, easy communication with the satellite from fixed ground stations. Due to the high cost of launching a satellite and the significant commercial value of each communication channel, there is a strong push to maximize the capacity of every satellite. The lifespan and dependability of satellites are key considerations, with simpler designs often being preferred to boost overall reliability [3]. Achieving communication and navigation functionality within a satellite system has been a long-standing goal worldwide. The Chinese Area Positioning System (CAPS) concept was first introduced, followed by extensive research and development on key technical aspects to create a CAPS demonstration system. This system is successfully integrated into communication and navigation satellites [7]. According to the CAPS concept, a network of ground facilities supporting navigation functions is established in addition to the existing satellite communication system. These ground facilities predict and determine the satellite's orbit, measure and compute signal transmission times, adjust the satellite signals to a specific frequency, edit navigation messages, and generate signals in PRN (Pseudorandom Noise) codes, making the transmitted signal behave like that of a typical navigation satellite. Users within the system's coverage area can determine their real-time position, velocity, and time using receivers similar to those used in current satellite navigation systems like GPS, Global Navigation Satellite System (GLONASS), and GALILEO. [7] The CAPS concept is presented in Figure 4.

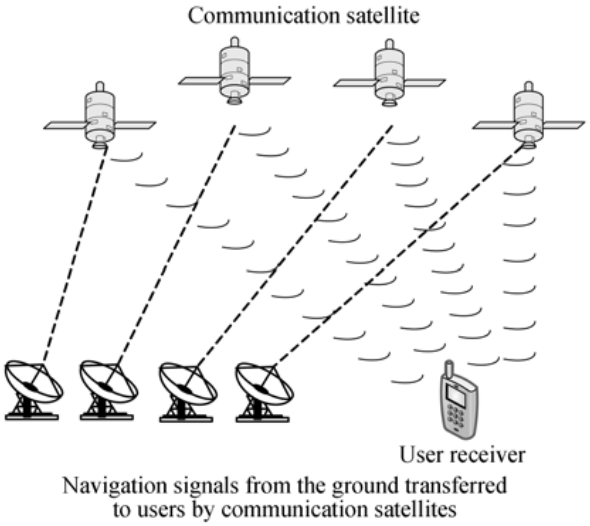

Figure 4. CAPS concept [7]

2.2.3. Planetary Missions

Planetary missions can be divided into inner and outer planetary missions. They usually vary in conditions and distances involved. Therefore, vehicles will have different designs depending on their assigned missions. Inner missions target planets from Mercury to the inner reaches of the asteroid belt (which are close to the sun). These shuttles usually rely on solar power and have

shorter travel times. In contrast, outer missions target planets beyond the asteroid belt and utilize nuclear power, due to the great distances from Sun. Hence, outer planetary vehicles require systems that function in lower temperatures, unlike inner vehicles [3]. In certain cases, such as the inner moons of Jupiter or the surface of Venus, extreme radiation or thermal conditions make human exploration impossible. For other destinations, particularly in the outer solar system, round-trip missions with current propulsion technologies would take almost an entire human lifetime. Therefore, robotic rovers present a compelling alternative for advancing exploration efforts [8]. Due to the significant communication delay between Earth and Mars, as well as other planets, direct teleoperation of a rover from Earth is impractical. Teleoperation relies on real-time human perception and feedback control, which becomes inefficient with such long signal times. As a result, some level of autonomy is required for rovers.

2.3. Space robots

Space robotics are essential for current and future space exploration, enabling specialized machines to operate in harsh space environments. These robots are designed to carry out tasks such as exploration, assembly, construction, maintenance and repair. They also conduct scientific investigations on distant lunar and planetary surfaces [9]. The ability to move allows these missions to gather data from various locations, enhancing scientific returns compared to static landers. Technological progress over the years has resulted in the development of diverse mobile systems, some based on terrestrial vehicles such as cars or military tanks with tracks. Some are uniquely engineered for space, such as hoppers and hybrid models [10].

2.3.1. Mobility systems

As research and technology have progressed, a variety of mobile systems with distinct shapes, sizes and configurations have emerged. Each system is suited to different operational environments, with unique strengths and limitations in areas such as slope navigation, obstacle crossing, speed and power usage. The selection of the mobility system depends on the specific goal, demands and reliability. To date, several robotic vehicles have been deployed to explore and study lunar and planetary surfaces, operating autonomously or through human control [10]. Various types of locomotion systems have been developed, depending on the terrain, and can be classified as aerial, sliding, rolling, wheel-enabled, leg-enabled, track-enabled, hoppers and hybrid. Although many mobility systems exist, a few are used more frequently. Therefore, these will be the focus of the discussion.

2.3.1.1. Wheel-enabled systems

Wheels have long been a standard solution for enabling movement in terrestrial applications, such as in various on-road and off-road vehicles. Wheel-based systems, or rovers, can be classified according to the number of wheels they use. Therefore, the available robots are the eight-wheel system and the six-wheel system [10]. The Eight-Wheel Drive System was first used in space exploration missions during the Soviet Union’s Lunokhod-1 and 2 missions to the lunar

surface in 1970 and 1973, respectively. The Lunokhod-1 rover had a total mass of 750 kg, with the suspension system weighing 105 kg [10]. The wheels were fixed and not swivel, so the rover turned by adjusting the rotational speeds of the wheels on each side. Over the past decade, Six-Wheeled Drive systems have become a hallmark of several high-profile rovers, particularly those developed by NASA's Jet Propulsion Laboratory (JPL) at the California Institute of Technology [11]. Notable examples include the JPL test-bed rover Rocky 7, the Sojouner rover from the Mars Pathfinder mission, the Mars Exploration Rovers (MERs), Spirit and Opportunity, as well as the Mars Science Laboratory (MSLS). These rovers are equipped with the "rocker-bogie" suspension system, shown in Figure 5a), which has demonstrated excellent mobility and performance. This system has been key to the success of Mars rover missions, allowing rovers like Spirit and Opportunity to exceed their lifetimes by a significant margin. The upcoming lunar rovers from JPL are also expected to incorporate this advanced suspension design [11].

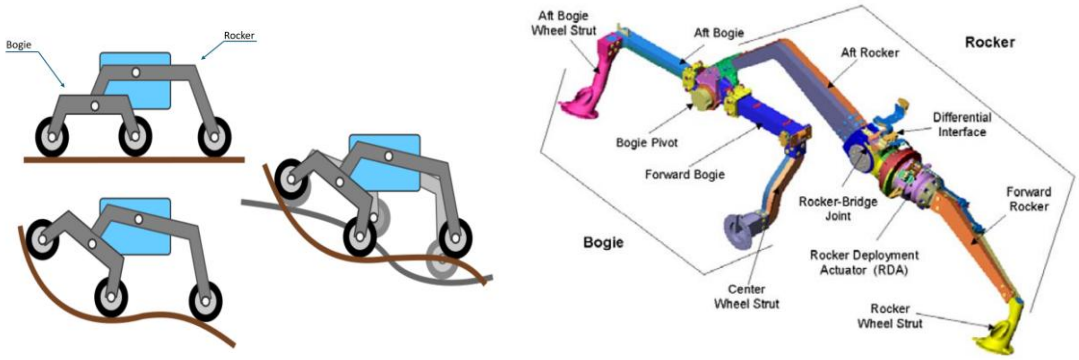

a) b)

Figure 5. a) Rocker-bogie suspension sketch [12]; b) Rocker-bogie suspension system [10]

The rocker-bogie suspension system operates with a 6x6x4 wheel configuration, meaning it has six wheels, all of which are driven independently by Direct Current (DC) motors. Additionally, the front and rear wheels are steered using identical DC motors. A differential mechanism inside the rover's body connects the left and right rocker-bogie assemblies. This suspension design allows the rover to maintain continuous contact between all six wheels and the ground, even on extremely uneven terrain. Typically, rovers equipped with this system can overcome obstacles that are at least as tall as the diameter of their wheels, and testing has shown that they can navigate objects up to 1.5 times the wheel diameter [10]. The suspension system also assists with climbing loose-soil surfaces by distributing the pressure across all wheels, preventing any one wheel from sinking into soft terrain due to excessive pressure. This is essential for maintaining mobility on such surfaces. However, a major challenge observed in Martian missions is wheel slippage, which can result in the rover becoming stuck. These issues arise from design limitations, such as surface unpredictability and the need for compact rover designs [10]. Figure 5b) presents a more technical view of the rocker-bogie suspension system.

2.3.1.2. Track-enabled systems

Tracked rovers utilize crawler tracks, which are commonly found in terrestrial vehicles like military tanks and off-road vehicles. These tracks are particularly effective for navigating

challenging or rough terrain. Presently, tracked systems are being evaluated for potential use in extraterrestrial surface exploration [11]. One of the Mars rover configurations, known as the Bendix rover, features a four-track module design. The inclusion of articulated suspension arms for each module greatly enhanced the mobility of this model. In the Soviet Union, and later in Russia, the development of tracked locomotion systems for planetary rovers was conducted by VNIITRANSMASH, the organization responsible for designing and building the chassis of Lunokhod-1 and 2 [13]. The control system allowed for differential speeds on each side of the rover, enabling it to turn by varying the speed of the tracks. Additionally, it could perform on-the-spot turns by rotating the tracks in opposite directions, similar to a tractor's turning mechanism [13]. The Nanokhod is a small, **twin-tracked** robot (shown in Figure 6a)) developed using Russian technology. Originally intended to be launched with the Beagle-1 lander as part of European Space Agency (ESA's) 2003 Mars Express mission, the plan was ultimately cancelled. The track system was later adapted for the BepiColombo mission to Mercury, but that too was cancelled. Since then, the Nanokhod has been the subject of extensive research for potential use in lunar and other planetary missions [10].

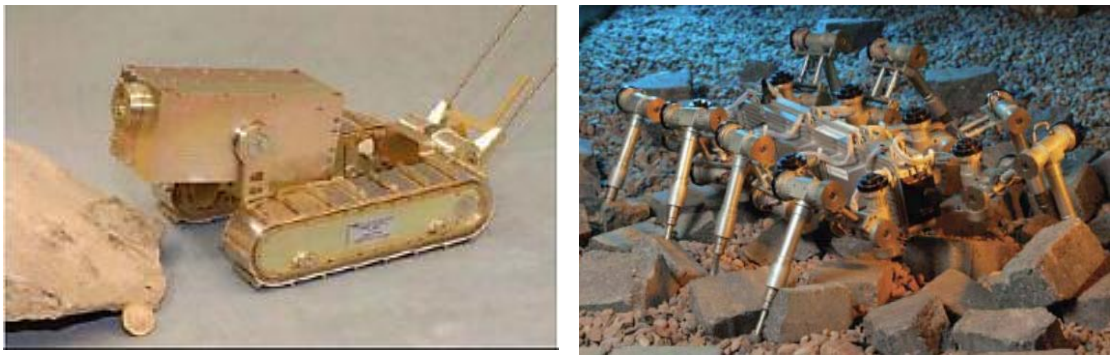

a) b)

Figure 6. a) Nanokhod robot [11]; b) SCORPION robot [10]

Japan Aerospace Exploration Agency (JAXA) Advanced Scape Technology research group has proposed a tracked system for the SELENE-II lunar mission. The mobility system features Four Caterpillar Crawl units, with two units on each side. These units utilize mesh structures, where the links are interlocked and equipped with small L-shaped lugs to ensure traction. Each crawl unit is fitted with metal mesh belts for added durability [10].

2.3.1.3. Leg-enable system

Legged robots offer versatile mobility, making them well-suited for use in both structured environments and on uneven terrain. However, they tend to be relatively slow and require significant energy to operate. In general, legged robots feature numerous actuators and have complex control systems [14]. The design of these robots is heavily inspired by biology, with models ranging from two-legged robots to four-legged robots and even eight-leg robots. While the number of legs is a common way to classify these robots, their most important feature is their gait, which can be either static or dynamic [14]. SCORPION is an octapod developed by the German Research Center for Artificial Intelligence, Defense Advanced Research Projects Agency

(DARPA), and NASA, designed for navigating rough and hazardous terrain. It measures 65 cm in length, with a ground clearance of 28 cm, and each leg has three degrees of freedom. The legs feature joints powered by 24V, 6W DC motors, and are equipped with a spring element to reduce stress and measure ground contact forces [10]. The SCORPION robot is shown in Figure 6b). The German Aerospace Center (DLR) Walker is a Six-Legged Robot developed by the institute of Robotics and Mechatronics at the German Aerospace Center. Its legs are adapted from the DLR Hand-II design, featuring three independently actuated joints that are enable omni-directional walking. Each leg uses brushless DC motors, belts and harmonic and bevel gears for movement, with the base joint offering two degrees of freedom. The medial joint has lower power to balance the leg in stretched positions, while the third joint is passive [10].

2.3.1.4. Hopping robots

Hopping systems for planetary mobility were initially proposed as a potential method of transportation for astronauts in lunar environments. Developing a hopping system offers several advantages such as reducing the number of actuators and enabling the use of a televisions camera and basic scientific sensors. Moreover, it is possible to deploy multiple units due to the minimized size and weight and provide sufficient mobility for scientific exploration. The simultaneous control of hopping height, direction, body stability, and camera orientation are achieved by sequencing operations instead of performing them concurrently. The mobility system of the first hopper prototype consists of a simple linear spring powered by a motor with the assistance of an over-running clutch [15].

2.3.1.5. Hybrid systems

Hybrid locomotion systems are particularly appealing for mobile robots because they combine the strengths of different mobility types while aiming to minimize their weakness. Legged locomotion, for instance, is highly effective in navigating unstructured terrains. However, for increased speed and energy efficiency, wheels or tracks are often preferred, offering a practical component to legged movement [14]. Leg-Wheels Hybrid Systems can be designed to be modular, reusable, redundant and reconfigurable, offering flexibility and reliability. A notable example is the DLR's hybrid concept, which integrates two modules, a six-wheeled rover paired with a six-legged walking system [10]. The legged system can either carry the entire rover or detach from the main body while still transporting the payload, as can be seen in Figure 7.

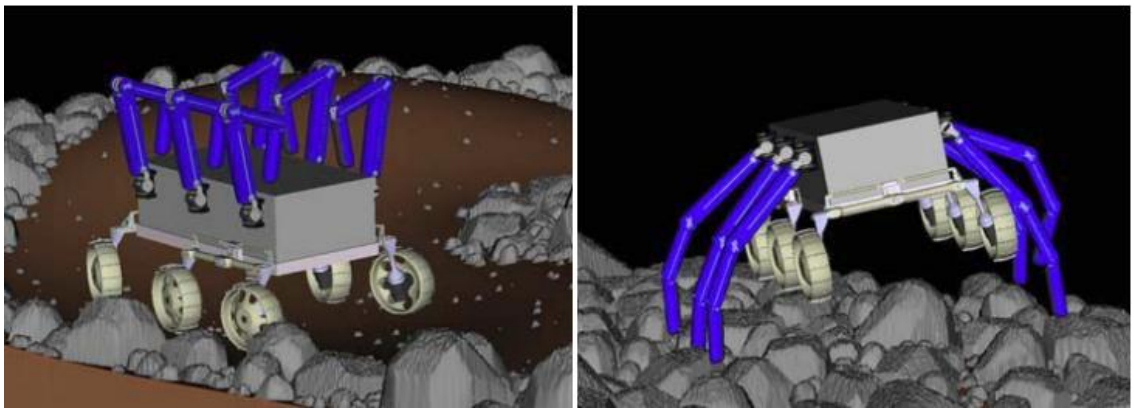

Figure 7. DLR in wheel mode and legged mode [10]

While wheel-legged robots offer significant advantages, other hybrid vehicles also exist, such as legged-track vehicles and hop-roll robots, each providing unique mobility solutions for different terrains and challenges. Legged-Track Hybrid Robots developed by researchers in Japan, feature a unique locomotion system combining legs and tracks. This system consists of four leg-crawl units, two on each side of the robot. Each includes two links equipped with crawl tracks and two rotational joints. In total, the robot operates with 16 motors, with four motors powering each unit. The design allows the robot to switch between multi-legged and tracked configurations, enabling it to adapt to various terrains however, the robot is still under development [11]. Hop-Roll Hybrid Systems combine the mobility advantages of both hopping and rolling mechanisms. These systems can hop to navigate obstacles and feature a ball-shaped design for efficient rolling on inclined surfaces. A notable example is the Microbot, developed by the Massachusetts Institute of Technology. This design is intended to operate as part of a swarm, enabling large-scale exploration and communication between multiple microbots, enhancing both coverage and coordination [10]. Figure 8 shows both the Legged-track hybrid robots (Figure 8a)) and Hop-roll hybrid systems in (Figure 8b))

a) b)

Figure 8. a) Legged-track hybrid robots [11];b) Hop-roll hybrid systems [10]

2.3.1.6. Mobility systems and their missions

Table 1 highlights various ground missions that have taken place, where some of the robots discussed above where used.

Table 1. Launches of mobile robots [10]

Robot name	Mission	Year	Body	Country	Mobility system		
					Wheels	Skids	Hoppers
Lunokhod-1	Luna 17	1970	Moon	Soviet Union	✓		
Prop-M	Mars 2	1971	Mars	Soviet Union		✓	
Lunar Roving Vehicle	Apollo 15-17	1971-1972	Moon	USA	✓		
Lunokhod-2	Luna 21	1973	Moon	Soviet Union	✓		
Sojourner	Mars Pathfinder	1996	Mars	USA	✓		
MINERVA	Hayabusa	2003	Asteroid Itokawa	Japan			✓
Spirit	MER-A	2003	Mars	USA	✓		
Opportunity	MER-B	2003	Mars	USA	✓		
Curiosity	Mars mission	2011	Mars	USA	✓		
Preseverance	Mars mission	2020	Mars	USA	✓		

2.3.2. Planetary environment

Understanding environmental parameters is crucial for defining the design requirements of space vehicles and related equipment. These parameters are necessary to outline the design conditions for various phases, including fabrication, storage, transportation, testing, pre-flight activities, in-flight operations, and on-orbit performance. Both the overall system and its components must be considered.

2.3.2.1. Lunar environment

In the context of the lunar environment, the most concerning factors are the severe temperature to which astronauts are exposed, the low gravity, and the deficiency of an atmosphere. Of all the factors, the most relevant is ionizing radiation, because there exists a large flux of high-energy solar-winds particles and a low flux of high-energy galactic cosmic rays. Since the moon has a harmful ionizing environment, robots must be engineered with materials that can handle such extreme conditions. A concerning factor about the moon's environment is the severe dust that surrounds the atmosphere. Dust wraps mechanical elements and joints, leading to fractures and abrasions. Moreover, the layer of dust formed serves as a thermal insulator, making it difficult to remove and manage heat in the robot’s components. The temperature felt on the moon can vary from 101°C to -181°C. It is therefore necessary to make an exceptional choice of materials and vehicle design to minimize the probability of failure [16].

2.3.2.2. Mars environment

On Mars, there is no greenhouse effect, derived from the thin existing atmosphere. Such phenom leads to extreme temperature variations. The lowest temperature measured, at the poles, was -143 °C. In contrast, the highest was during summertime, reaching a value of 27 °C [17]. While being composed primarily of carbon dioxide, Mars exhibits an atmosphere esteeming 1% of the density of Earth. Mars also lacks a global magnetic field however, magnetic anomalies do occur. According to previous missions, Mars surface can be categorized into rocks, drift material and soil, with soil covering 80-90% of the landing sites [17].

2.3.3. Material selection

The selection of material is one of the most important phases of designing the space rover. As mentioned before, space presents adverse environments for the vehicle, with extreme situations. It is therefore necessary for the material to be able to withstand severe conditions, as well as the ability to maintain its original form and be reliable. In the following sections, the properties of several materials will be reviewed.

2.3.3.1. Metal alloys

Aluminium alloys are widely known for their exceptional capacity to withstand corrosive environments, being lightweight and high specific strength. Utilizing aluminium alloys in space can be advantageous since they have a good low-temperature resistance (if used on planets afar from the Sun). In rover missions, aluminium alloys are frequently employed on wheels [18]. Compared to steels, aluminium has a less constrained core, mainly due to the lower modulus of elasticity (approximately one-third of that of steel) [19].

Steels can be used to retain high-pressure gas which is needed for parachute propulsion [18]. It is possible to do it since steels are used as structural components for heavily loaded applications. As mentioned earlier, the severe environment observed in space can lead to corrosion, due to dust and radiation. Therefore, the use of carbon steel is restrained and to prevent that, the use of stainless steel is a solution. Moreover, stainless steel can be subjected to low temperatures since it has a low ductile-to-brittle transition temperature [3].

Titanium alloys possess extraordinary mechanical strength and high-temperature resistance. The use of titanium is also advantageous since it shows great stiffness. The biggest disadvantage of titanium usage is the significantly higher cost and the lower availability, however, these alloys are still widely employed when designing space robots and vehicles [3]. The relation between shear stress of various materials with different crystalline structures and various temperatures is shown in Figure 9.

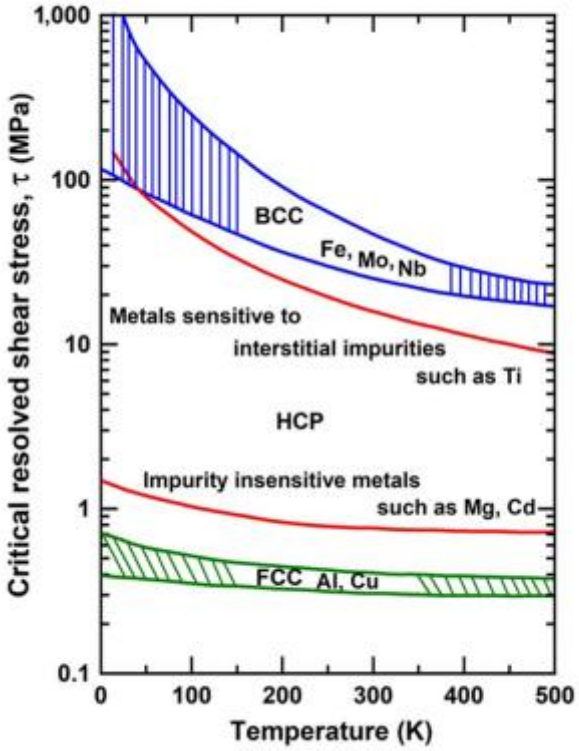

Figure 9. Critical resolved shear stress for different metallic materials, depending on the temperature [19]

2.3.3.2. Composites

Some materials when used individually may exhibit deficiencies, however, when combined with another or various materials, their properties can be optimized. The result of the combination of various components is a composite. In composites there is the possibility to blend light and tough materials to achieve the desired properties for a specific project. Implementing composite materials offers significant benefits, since it's easy to manufacture complex geometries since the final shape is determined during the initial creation process. This leads to a much more efficient and even cheaper production and better solutions [20]. There is a various list of composite materials, however the most important are glass fibers and carbon fibers, which are discussed next.

Glass fibers with reinforced plastic, or fiberglass, are the most common type of fibers used in space technology and were the first to be utilized. These types of fibers allow the adjustment of the density and the orientation of fibers, granting the freedom to determine the strength and stiffness desired [3]. When used as a reinforcement, E-glass is the most utilized in composite materials, as well as accounting for the largest volume of appliances, however, S-glass exhibits better properties, taken as an example the higher thermal stability, yet its usage is lower since the value of these material is higher, in contrary to E-glass [20]. These fibers also have low electric conductivity and transmission loss. Therefore, they are applied in the design of satellite antennas [21]. They also possess a low thermal conductivity and specific weight

(which is very desired), high strength as well as a significant endurance to thermal and chemical effects [22].

Carbon fibers, at quite high temperatures, have the potential to maintain shape and withstand ablation and oxidation, however, for extreme temperatures a silicon carbide coat is applied to ensure protection [3]. Moreover, carbon fibers also exhibit a wide range of outstanding and beneficial mechanical attributes, including high strength and elasticity modulus, good thermal stability and high resistance against ambient impacts [22].

2.4. Perseverance Rover

The Perseverance Rover (Figure 10) launched to Mars in 2020, with the objective of enhancing the current understanding of Mars. It is searching for locations situated in Jezero Crater that were habitable in the past, investigating whether life ever existed there and looking for the existence of ancient life. Additionally, the Rover is analysing the evolution of Mars atmosphere and surface. Perseverance is also assisting current studies on whether future human missions to Mars are feasible, while testing newer technologies. Moreover, samples of the planet are being collected by it in case of a future return. While being based on its predecessor Curiosity, the Perseverance is equipped with a technology and science toolbox and has the capacity to recover samples and mine minerals. This is the most important feature that differentiates both Rovers, and to achieve it, the robot is equipped with an “arm” that possesses a drill and tubes to assist the sample collection. With a similar design to a car, the Rover measures roughly 3 meters in length, 2.7 meters in width and 2.2 meters in height, and weighs 1025 Kg [23].

Figure 10. Perseverance rover [23]

2.4.1. Wheels and suspension system

Following past Mars successful missions, and the rovers associated, the Perseverance rover is equipped with the same suspension system, the “rocker-bogie”. This system links the wheels to its body, allowing it to navigate around the Mars surface with ease. The rocker-bogie suspension system is built with three key components, with them being the differential, located at the center of the top deck, connects both the right and the left rockers and is attached to the main body by a pivo; the Rocker which connects the front wheels to the differential and the bogie that connects the rocker to the rear and middle wheels [23]. Perseverance is engineered to maintain is position when tilted up to 45° in any direction. However, to prevent any consequences, rover drives avoid driving surfaces that can indulge a tilt higher than 30°, ensuring the safety of the vehicle [23]. Perseverance Rover was designed with six wheels, with every one having its separate source of power. Moreover, the front and the rear wings are built with individual steering motors, enhancing the rover’s agility and allowing it to perform 360° turns and more precise swerves and curves. The Curiosity rover while navigating, experienced sharp and jagged rocks which led to the tear and devastation of its wheels. Therefore, in 2020, engineers redesigned the Perseverance rover wheels to have higher durability [23]. Now, the rover wheels are narrower, designed with a thicker aluminium and a bigger diameter (52.5 cm), making them better prepared to handle the Martian terrain. They also are equipped with cleats with the objective of increasing traction. The rover’s legs are built with titanium tubing, like those in high-end mountain bikes. This aspect grants the possibility to navigate over rocks up to 40cm. The difference between each rover wheel is observed in Figure 11 [23].

Figure 11. Comparison between Curiosity and Perseverance wheels [23]

2.4.2. Rover speed

While in planetary exploration speed is not the central focus of the rover’s objectives, Perseverance, when compared to previous rovers, is a top-notch rover. It achieves its maximum speed of 152m/h, when on flat hard ground. This slow pace (but energy-efficient) allows the rover to consume less than 200W, in comparison to a 200-horsepower car that consumes about 150000 W [23].

2.4.3. Additional technology

Besides all the technology discussed previously, the Perseverance Rover is supplied with much more equipment to assist the exploration and to provide NASA with improved information. The rover possesses various cameras each with different tasks. Some cameras assist in driving, functioning as eyes while others take photos and collect samples helping with scientific discoveries. The rovers possess 23 cameras in total. When designing Perseverance, engineers equipped the rover with two microphones, making it not only possible to collect and observe Mars, but also listen to its sounds. As it was discussed previously, a robotic arm is attached to the main body and has the assignment to support the Martian surface investigation and sample collection. At the end of the robotic arm, a turret is connected, and it carries the scientific cameras, as well as a drill and mineral and chemical analyzers [23].

3. NUMERICAL METHODS

This chapter provides a fundamental overview of solid mechanics principles and their engineering applications. It explores both the weak and strong formulations of these methods and examines the theory behind meshless methods such as the Radial Point Interpolation Method (RPIM) and Natural Neighbour Radial Point Interpolation Method (NNRPIM). This section will also discuss the general procedures of these methods, particularly the nodal connectivity, the numerical integration, the shape functions and the system of equations behind meshless methods.

3.1. Solid mechanics fundamentals

When solids and structures are subjected to forces, they undergo stress, which then results in strain, essentially the material's deformation or internal movement. Solid and structural mechanics focus on understanding the connections between stress and strain, as well as evaluating how strains translate into displacements, given the boundary conditions [24]. Materials can exhibit a range of behaviours depending on their specific properties. In elastic materials, any deformation associated with applied loads, is entirely eradicated once the load is removed. On the contrary, materials subjected to plastic deformation remain deformed even after the force is fully eliminated, making it impossible for those materials to return to their original shape [24]. Materials, according to their mechanical properties, can also be divided into two categories: if isotropic, the same mechanical properties can be seen in various directions, in contrast to anisotropic materials, which exhibit different properties, depending on the direction [24]. Isotropic materials are often described as a special type of anisotropic materials since there is only the need to know two independent properties, the Poisson's ratio and the Young's modulus. However, anisotropic materials require the definition of various additional mechanical properties to achieve a complete description [24].

3.1.1. Stress/ principal stress

During a large deformation analysis, a body may undergo severe rotations or strains. By defining stress and strains, it becomes possible to represent virtual work as an integral over the volume of the body, reflecting its changing configuration. Due to the fact that the use of vectors is more

practical when reaching the programming step, these stresses can be referred as stress tensors, which are often written in vector form [24].

$$\boldsymbol{\sigma} = \{\sigma_{xx}\ \ \sigma_{yy}\ \ \sigma_{zz}\ \ \sigma_{xy}\ \ \sigma_{yz}\ \ \sigma_{zx}\}^T \tag{1}$$

Every six stress tensors correspond to six strain components, which can also be represented as in vector form:

$$\boldsymbol{\varepsilon} = \{\varepsilon_{xx}\ \ \varepsilon_{yy}\ \ \varepsilon_{zz}\ \ \varepsilon_{xy}\ \ \varepsilon_{yz}\ \ \varepsilon_{zx}\}^T \tag{2}$$

An alternative way to represent stress tensors, is with the Cauchy stress tensor, which fully defines the stress state at a given point of interest, expressed in equation (3).

$$\boldsymbol{\Lambda} = \begin{bmatrix} \sigma_{xx} & \sigma_{xy} & \sigma_{xz} \\ \sigma_{yx} & \sigma_{yy} & \sigma_{yz} \\ \sigma_{zx} & \sigma_{zy} & \sigma_{zz} \end{bmatrix} \tag{3}$$

Strain represents the variation in displacement over a unit length. The strain components can be determined by taking the spatial derivatives of the displacement values, which result in equations (4):

$$\varepsilon_{xx} = \frac{\partial_u}{\partial_x};\ \varepsilon_{yy} = \frac{\partial_v}{\partial_y};\ \varepsilon_{zz} = \frac{\partial_w}{\partial_z};\ \varepsilon_{xy} = \frac{\partial_u}{\partial_y} + \frac{\partial_v}{\partial_x};\ \varepsilon_{yz} = \frac{\partial_v}{\partial_z} + \frac{\partial_w}{\partial_y};\ \varepsilon_{zx} = \frac{\partial_w}{\partial_x} + \frac{\partial_u}{\partial_z} \tag{4}$$

3.1.2. Constitutive Equations

The connection between the stress rate and the strain is presented in equation (5):

$$\boldsymbol{\sigma} = \boldsymbol{c}\,\boldsymbol{\varepsilon} \tag{5}$$

where $\boldsymbol{c}$ represents the material constitutive matrix. In cases where material nonlinearity exists between $\boldsymbol{\sigma}$ and $\boldsymbol{\varepsilon}$, then $\boldsymbol{c}$. From equation (6) ,it is possible to derive the following expression:

$$\boldsymbol{\varepsilon} = \boldsymbol{c}^{-1}\,\boldsymbol{\sigma} \tag{6}$$

In this case, $\boldsymbol{c}^{-1}$ is defined as *s,* compliance matrix, and is specifically determined for a three-dimensional matrix (7):

$$\boldsymbol{s} = \begin{bmatrix} \frac{1}{E_{xx}} & \frac{\nu_{yx}}{E_{yy}} & -\frac{\nu_{zx}}{E_{zz}} & 0 & 0 & 0 \\ -\frac{\nu_{xy}}{E_{xx}} & \frac{1}{E_{yy}} & -\frac{\nu_{zy}}{E_{zz}} & 0 & 0 & 0 \\ -\frac{\nu_{xz}}{E_{xx}} & -\frac{\nu_{yz}}{E_{yy}} & \frac{1}{E_{zz}} & 0 & 0 & 0 \\ 0 & 0 & 0 & \frac{1}{G_{xy}} & 0 & 0 \\ 0 & 0 & 0 & 0 & \frac{1}{G_{yz}} & 0 \\ 0 & 0 & 0 & 0 & 0 & \frac{1}{G_{zx}} \end{bmatrix} = \boldsymbol{c}^{-1} \quad (7)$$

3.1.3. Strong and weak form formulation

The strong form of equations consists of the partial differential equations that describe the governing laws of physical phenomena. On the other hand, the weak form relaxes the consistency requirements for the approximation functions used. When encountering complex engineering problems, obtaining the exact solution utilizing strong form system equations would be ideal, however such condition it is not possible. Therefore, the usage of weak formulations often leads to more accurate results, since they produce more constant algebraic results [24].

3.1.3.1. Galerkin Weak Form

The Galerkin weak form relies on the energy principle, which declares that among all potential displacement configurations that satisfy compatibility conditions, essential boundary conditions, as well as initial and final time conditions, the true solutions corresponds to the configuration that minimizes the Lagrangian functional L [24].

$$L = T - U + W_f \quad (8)$$

In equation (8), T refers to the kinetic energy (equation (9)), *U* is the strain energy (equation (10)) and W_f is the work created by external forces (equation (11)). Kinetic energy is defined in terms of the solid volume Ω, where the displacement vector $\boldsymbol{u}$ is differentiated with respect to time (velocity). Solid mass density is referred as to ρ. Strain energy, for plastic materials, is defined in terms of the strain vector $\boldsymbol{\varepsilon}$ and the stress vector $\boldsymbol{\sigma}$. The work generated by external forces is expressed in terms of displacement, the body forces $\boldsymbol{b}$ and the external forces $\bar{\boldsymbol{t}}$ applied [24].

$$T = \frac{1}{2}\int_{\Omega} \rho \dot{\boldsymbol{u}}^T \dot{\boldsymbol{u}}\, d\Omega \quad (9)$$

$$U = \frac{1}{2}\int_{\Omega} \boldsymbol{\varepsilon}^T \boldsymbol{\sigma}\, d\Omega \tag{10}$$

$$W_f = \int_{\Omega} \boldsymbol{u}^T \boldsymbol{b}\, d\Omega + \int_{\Gamma_t} \boldsymbol{u}^T \bar{\boldsymbol{t}}\, d\Gamma \tag{11}$$

If substituting the previous expressions in the Lagrangian formula, it possible to obtain expression (12):

$$L = \frac{1}{2}\int_{\Omega} \rho \dot{\boldsymbol{u}}^T \dot{\boldsymbol{u}}\, d\Omega - \frac{1}{2}\int_{\Omega} \boldsymbol{\varepsilon}^T \boldsymbol{\sigma}\, d\Omega + \int_{\Omega} \boldsymbol{u}^T \boldsymbol{b}\, d\Omega + \int_{\Gamma_t} \boldsymbol{u}^T \bar{\boldsymbol{t}}\, d\Gamma \tag{12}$$

and then reduced to a minimum with t_1 being the initial time and t_2 the final time,

$$\delta \int_{t_1}^{t_2} \left[\frac{1}{2}\int_{\Omega} \rho \dot{\boldsymbol{u}}^T \dot{\boldsymbol{u}}\, d\Omega - \frac{1}{2}\int_{\Omega} \boldsymbol{\varepsilon}^T \boldsymbol{\sigma}\, d\Omega + \int_{\Omega} \boldsymbol{u}^T \boldsymbol{b}\, d\Omega + \int_{\Gamma_t} \boldsymbol{u}^T \bar{\boldsymbol{t}}\, d\Gamma \right] dt = 0 \tag{13}$$

The function being integrated can be expressed as equation (14), obtained by simplifying the initial term of the integral previously presented.

$$\int_{t_1}^{t_2} \left[\frac{1}{2}\int_{\Omega} \delta(\rho \dot{\boldsymbol{u}}^T \dot{\boldsymbol{u}})\, d\Omega \right] dt = -\int_{t_1}^{t_2} \left[\rho \int_{\Omega} (\delta \boldsymbol{u}^T \ddot{\boldsymbol{u}})\, dt \right] \tag{14}$$

When refining the second term on equation (14), the integrand function can be expressed as follows:

$$\delta(\boldsymbol{\varepsilon}^T \boldsymbol{\sigma}) = \delta \boldsymbol{\varepsilon}^T \boldsymbol{\sigma} + \boldsymbol{\varepsilon}^T \delta \boldsymbol{\sigma} \tag{15}$$

Since both terms are scalars, transposing them will not oppose any effect to the result. Therefore, this term can be written in the following form:

$$\delta \boldsymbol{\varepsilon}^T \boldsymbol{\sigma} = (\delta \boldsymbol{\varepsilon}^T \boldsymbol{\sigma})^T = \boldsymbol{\sigma}^T \delta \boldsymbol{\varepsilon} \tag{16}$$

Using both the constitutive equation ($\boldsymbol{\sigma} = \mathbf{c}\boldsymbol{\varepsilon}$) and the symmetric property of material matrix (the transposed matrix is equal to the original), equation (17) is obtained:

$$\delta \boldsymbol{\sigma}^T \boldsymbol{\varepsilon} = \delta(\boldsymbol{c}\boldsymbol{\varepsilon})^T \boldsymbol{\varepsilon} = \delta \boldsymbol{\varepsilon}^T \boldsymbol{c}^T \boldsymbol{\varepsilon} = \delta \boldsymbol{\varepsilon}^T \boldsymbol{c}\boldsymbol{\varepsilon} = \delta \boldsymbol{\varepsilon}^T \tag{17}$$

It is possible now to insert both integral terms in equation (14), obtaining the equation (18).

$$\int_{t_1}^{t_2} \left[-\rho \int_{\Omega} (\delta \boldsymbol{u}^T \ddot{\boldsymbol{u}})\, d\Omega - \int_{\Omega} \delta \boldsymbol{\varepsilon}^T \boldsymbol{\sigma}\, d\Omega + \int_{\Omega} \delta \boldsymbol{u}^T \boldsymbol{b}\, d\Omega + \int_{\Gamma_t} \delta \boldsymbol{u}^T \bar{\boldsymbol{t}}\, d\Gamma \right] dt = 0 \tag{18}$$

Equation (19), is referred to as the "Galerkin weak form" and is equivalent to the principle of virtual work. This principle states that when a solid body is in equilibrium, the total virtual work generated by both the internal stresses and the applied external forces must equal zero during displacement of the body. By employing the stress strain relation ($\boldsymbol{\sigma} = \boldsymbol{c\varepsilon}$) and the strain-displacement relation ($\boldsymbol{\varepsilon} = \boldsymbol{Lu}$), the Galerkin equation is written as equation (19)[24]:

$$\int_{\Omega} \delta(\boldsymbol{Lu})^T \boldsymbol{c}(\boldsymbol{Lu})\, d\Omega - \int_{\Omega} \delta \boldsymbol{u}^T \boldsymbol{b}\, d\Omega - \int_{\Gamma_t} \delta \boldsymbol{u}^T \boldsymbol{t}\, d\Gamma + \int_{\Omega} \rho(\delta \boldsymbol{u}^T \ddot{\boldsymbol{u}})\, d\Omega = 0 \qquad (19)$$

3.2. Meshless methods

Meshless methods (or meshfree methods) utilize a distinct approach to discretization when compared to traditional mesh-based methods. Unlike the FEM methods, meshless methods rely on a distribution of nodes across the domain. Since these nodes can be distributed in irregular patterns, analysing complex engineering structures and geometries becomes feasible. Nodal density affects the accuracy of the results obtained, therefore, increasing the density of nodes leads to more accurate data [25], however increases the computational time. There are several meshless methods, including the Radial Point Interpolation Method (RPIM), the Element-Free Galerkin Method (EFGM), the Local Petrov-Galerkin Method (MLPG), the Natural Neighbour Radial Point Interpolation (NNRPIM) and the Reproducing Kernel Particle Method (RKPM).

3.2.1. Radial Point Interpolation Method

The Radial Point Interpolation Method (RPIM) has been widely used to solve differential and integral equations. It combines radial basis functions (RBFs) with polynomial basis functions to address the singularity issues inherent in polynomial-based point interpolation methods (PIM). Although polynomial augmentation is not strictly necessary for RPIM, relying solely on RBFs can lead to instability and ill-conditioned linear systems, requiring regularization techniques for stabilization [26]. RPIM significantly developed due to recent discoveries and has been applied to solve various problems. Notable advancements include weighted nodal RPIM for 2D solid mechanics in linear elasticity. The RPIM framework has been enhanced with normalized RBFs, allowing for the analysis of nonlinear thermal buckling in graded plates without requiring fitting parameters. It has also been extended to solve nonlinear coupled Burger's equations through advanced spectral techniques. Simplified versions of RPIM have been developed to improve computational efficiency in methods like Meshless Local Petrov-Galerkin (MLPG), particularly for analysing bending plates under Reissner's hypothesis [26]. RPIM demonstrates strong performance in various mechanical engineering applications, showing accuracy and computational efficiency in nonlinear analysis, especially when combined with interactive methods such as Newton-Raphson [26].

3.2.2. Natural Neighbour Radial Point Interpolation Method

The development of interpolating shape functions has been a key focus in computational mechanics, leading to several advancements in meshless methods. A significant development in this field is the Natural Neighbour Radial Point Method (NNRPIM). This method combines the natural neighbour connectivity from the Natural Element Method (NEM) with RPIM's interpolation approach. The NNRPIM is truly meshless, requiring only Cartesian coordinates of the nodal distribution to calculate the positions and the weights of the background integration points and establish the nodal connectivity using the natural neighbour concept. NNRPIM is a successful tool in meshless methods, since this combination discussed previously greatly enhances the accuracy of the results and it is more efficient [27].

3.2.3. Nodal connectivity

Within FEM, connectivity between nodes is inherently established trough a predefined element mesh, allowing nodes within an element to interact directly with each other and with boundary nodes of adjacent elements. In meshless methods, however, there is no initial connection between nodes. Therefore, node distribution defines the nodal connectivity of these meshfree methods [24]. This section will outline how nodal connectivity is defined in the RPIM and NNRPIM methods.

3.2.3.1. RPIM

In meshless methods, there is the need to overlap influence domains around each node in order to achieve nodal connectivity. These domains are defined by setting a fixed number of nodes within a specific area for 2D problems or specific volumes for 3D problems [24]. Many meshless methods implement this approach since it is simple to perform, however when analysing complex geometries or variations in size or shape of influence domains, the accuracy might be minimized or reduced. To balance the nodal connectivity and obtain more accurate results, it is generally recommended that each domain contain between 9 to 16 nodes [24]. To define influence domains, a reference dimension d is often calculated based on the average spacing h between nodes in the vicinity, with a scaling factor k typically between 1.5 and 2.5. Fixed-size influence domains can be either rectangular or circular (Figure 12). In the rectangular approach the dimensions dx and dy are specified, and for each target point x_i, the *n* nodes located within a $dx \cdot dy$ rectangle centered on x_i are identified. In the circular methods, a radius d_R is defined, and the *n* nodes within this circular area around $\boldsymbol{x}_i$ are selected. However, fixed influence domains near boundaries can result in fewer neighbouring nodes, which may reduce accuracy [24].

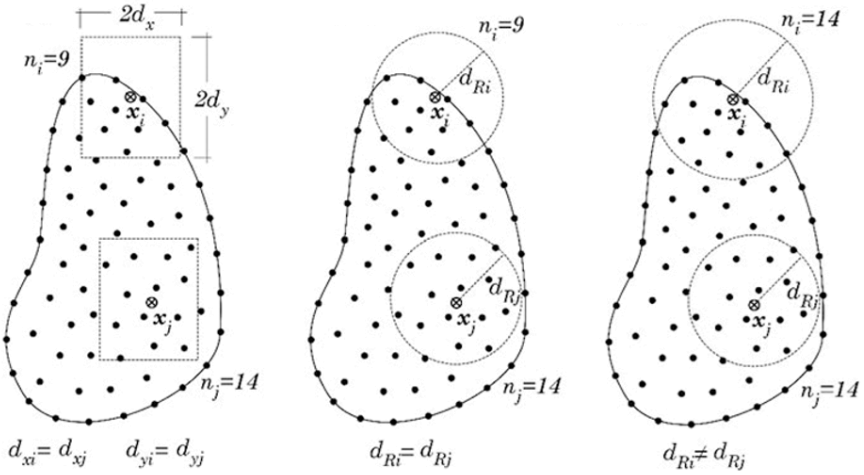

a) b) c)

Figure 12. a) Fixed rectangular shape domain. b) Fixed circular domain. c) Flexible circular domain [24]

3.2.3.2. NNRPIM

The NNRPIM employs the concept of natural neighbours to define integration points and establish nodal connectivity. This is based on constructing the Voronoï diagram of the problem's nodal discretization. For a 2D domain Ω, discretised with N nodes $\boldsymbol{X} = \{x_1, x_2, \dots, x_N\}$, the Voronoï diagram partitions Ω into convex, non-overlapping sub-regions V_i. Each cell V_i contains all points closer to the node $\boldsymbol{x}_i$ than to any other node, ensuring that $\Omega = \sum_{i=1}^{N} V_i$ [27]. The natural neighbours of a node $\boldsymbol{x}_i$ are those nodes whose Voronoï cells share and edge with V_i. Utilizing this property, the NNRPIM establishes nodal connectivity automatically. Instead of the conventional "influence domain", this method introduces the concept of an "influence cell", determined by the natural neighbours of $\boldsymbol{x}_i$. NNRPIM disposed two types of influences cells. The first-degree influence cells consist of $\boldsymbol{x}_i$ and their natural neighbours and the second-degree influence cells encompasses $\boldsymbol{x}_i$, the first neighbours and the neighbours of those first-degree nodes [27]. This approach eliminates the need for searches for nearby nodes, as the connectivity is inherently defined by the Voronoï diagram. Additionally, the duality between the Voronoï diagram and the Delaunay triangulation is leveraged to create background integration meshes, ensuring computational efficiency and accuracy. The NNRPIM's reliance on natural neighbours allows for robust, truly meshless analysis, capable of efficiently interpolate across the domain [24].

3.2.4. Numerical integration

This section introduces the integration basis utilized in the numerical and computational meshless methods. In variational-based numerical methods, such as Galerkin weak formulation, integration is a critical component for deriving the system of equations that govern the physical problem. Since in meshless methods, the computational effort represents a considerable portion of the analysis, this step is especially important.

3.2.4.1. RPIM

Utilizing the Gauss-Legendre integration, a regular grid separates the solid domain in equal parts, with each grid cell containing integration points following the Gauss-Legendre quadrature rule. This process involves transforming grid cells into isoparametric squares, distributing quadrature points, and calculating weights using the determinant of the Jacobian matrix. While these regular grids are computationally efficient, fitted grids offer greater stability and accuracy in results, even being more resource intensive [24]. In order to facilitate the approach of the Gauss-Legendre quadrature, its necessary to transform the initial quadrilateral into an isoparametric square, shown in Figure 13a). Then, quadrature points are distributed within the square, and utilizing isoparametric interpolation functions, their Cartesian coordinates are determined. In Figure 13b) the isoparametric square shape using a 2x2 quadrature is presented [24]. The integration weight for each point is determined by multiplying its isoparametric weight by the inverse of the Jacobian determinant for the corresponding grid cell, which can be seen in Figure 13c). If the grid perfectly aligns with the domain, there is no necessity for adjustment. Integration points outside the solid domain are removed from the grid [24]. When considering the function $F(\boldsymbol{x})$ which is defined in the domain Ω, it becomes possible to perform the following numerical integration, where the integration point of $\boldsymbol{x}_i$ is $\widehat{w_i}$ and n_g is the number of integration points (equation (20)):

$$\int_{\Omega} F(\boldsymbol{x})\, d\Omega = \sum_{i=1}^{n_g} \widehat{w_i}\, F(\boldsymbol{x}_i) \tag{20}$$

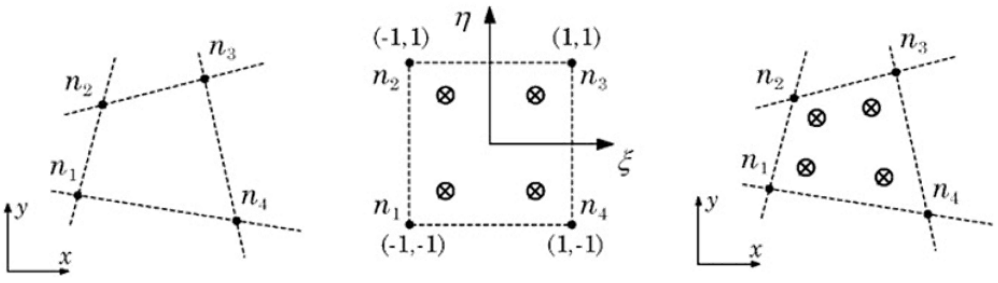

a) b) c)

Figure 13. a) First quadrilateral from the grid cell. b) isoparametric square shape from the initial quadrilateral. c) Return to the initial shape [24]

3.2.4.2. NNRPIM

In the initial phase of discretizing a two-dimensional domain $\boldsymbol{X} \subset \mathbb{R}^{\boldsymbol{2}}$ with a set of nodes $\boldsymbol{N} = \{n_1, n_2, \dots, n_N\}$, the Voronoï cells for each node are constructed. These cells are used to establish smaller sub-areas, which can be either quadrilateral or triangular, depending on whether the nodal distribution is irregular or regular [24]. For a given n_i, in an irregular distribution, its natural neighbours are represented by the finite set $\boldsymbol{N_I} = \{n_1, n_2, \dots, n_6\}$. These

neighbours are used to construct the Voronoï cell V_I for n_I, with corners P_{Ii} defining its polygonal boundary, which can be seen in Figure 14a). Next, the midpoints M_{Ii} between n_I and each neighbour node $n_i \in \boldsymbol{N_I}$ are identified, as shown in Figure 14b). Utilizing the previous calculated midpoints, the Voronoï cell V_I is subdivided into n quadrilateral sub-cells S_{Ii}, where *n* corresponds to the number of natural neighbours of n_I. This information is presented in Figure 14c) [24].

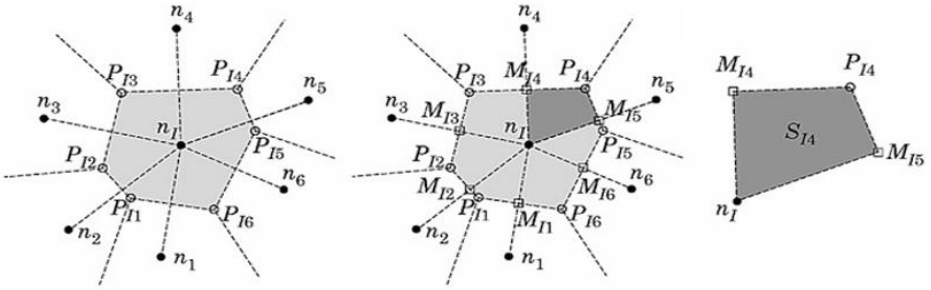

a) b) c)

Figure 14. a) Voronoï cell with its intersection points. b) Middle points and the respective quadrilaterals. c) Quadrilateral generated [24]

In a regular nodal distribution, the nodes $\boldsymbol{N} = \{n_1; n_2, \dots, n_N\}$ discretizing the domain $\boldsymbol{X} \subset \mathbb{R}^2$ result in Voronoï cells that are divided into triangular sub-cells in contrast to quadrilateral ones. For a node n_I, its natural neighbours $\boldsymbol{N_I} = \{n_1; n_2, \dots, n_8\}$ define a Voronoï cell V_I shaped as a perfect square with four corners P_{Ii} (Figure 15a)). By identifying the midpoints M_{Ii} it is then possible to divide the cell into n triangular sub-cells, illustrated in Figure 15b), where *n* denotes the total number of natural neighbours of the node n_I (Figure 15c)).

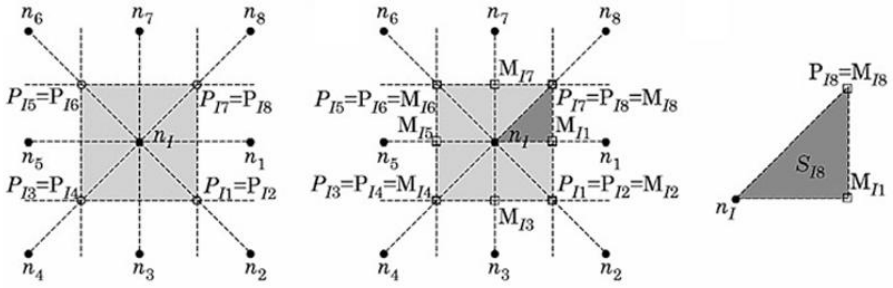

a) b) c)

Figure 15. a) Voronoï cell with its intersection points. b) Middle points and the respective triangles. c) Triangle generated [24]

It is possible now to determine the size of the Voronoï cell, using the sub-cells created by dividing the original cell, with the assistance of equation (21):

$$A_{V_I} = \sum_{i=1}^{n} A_{S_{Ii}}, \forall\, A_{S_{Ii}} \geq 0 \tag{21}$$

In equation (21), $A_{S_{Ii}}$ represents the size of the sub-cell S_{Ii} and A_{V_I} the size of the Voronoï cell V_I. An initial integration approach places one integration point at the geometric center of each triangular or quadrilateral sub-cell. The coordinates of these points are calculated for their respective sub-cells, as can be seen in Figure 16. The integration weight for each point is equal to the sub-cell's area [24].

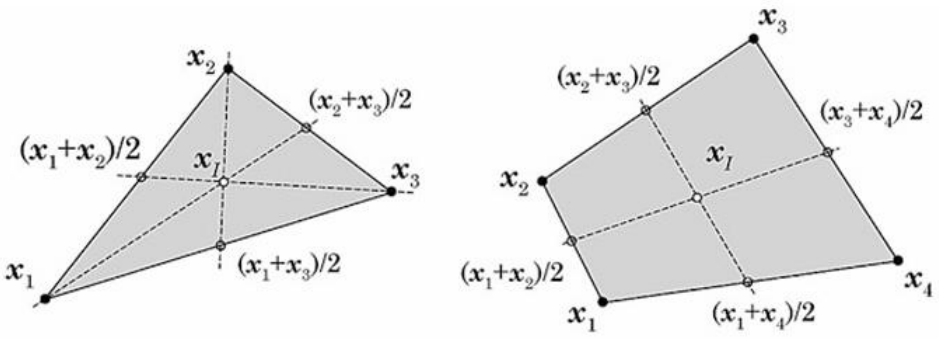

a) b)

Figure 16. Cell shapes with integration points. a) triangular. b) quadrilateral [24]

A more advanced integration system can be developed by further subdividing the sub-cells represented in Figure 16, transforming all shapes into smaller quadrilaterals or triangles. This process begins by identifying the centre of each geometric shape, x_C, and calculating the midpoints of the edges of quadrilaterals and triangular cells using $x_{ij} = (x_i + x_j)/2$. These new midpoints are used to define new, smaller sub-cells, as shown in Figure 17. The Gauss-Legendre quadrature method is then applied to these sub-quadrilaterals to determine the integration points. This method allows for $k \times k$ integration points to be distributed across each sub-quadrilateral or triangular cell. In Figure 17, it is possible to observe the Gauss-Legendre integration method with each sub cell containing 9 points each [24].

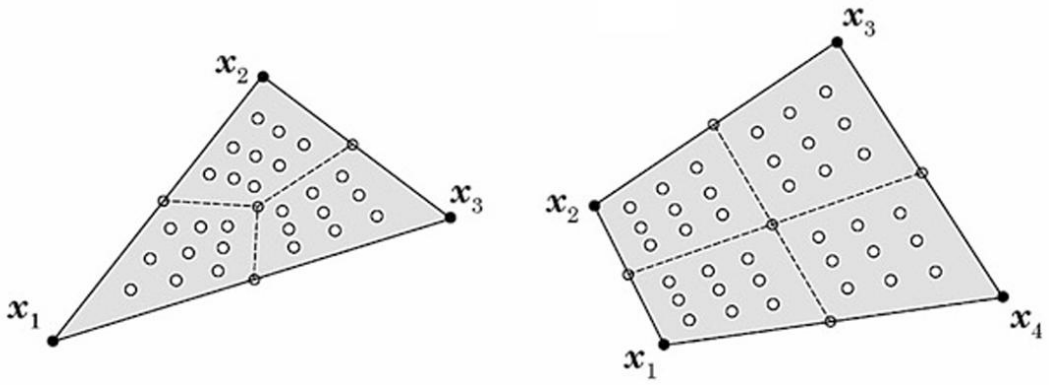

a) b)

Figure 17. Gauss-Legendre integration for a) quadrilateral and b) triangular cells with 9 points each [24]

3.3. Shape functions

Both the RPIM and NNRPIM use the radial point interpolation technique in the construction of their shape functions. In a 2D domain $\Omega \subset \mathbb{R}^2$, a field function $u(x)$ is discretized over N nodes $X = \{x_1, x_2, \dots, x_N\}$. For an integration point $x_I \notin X$, the interpolated value $u(x_I)$ is expressed as equation (22):

$$u(\boldsymbol{x}_I) = \{\boldsymbol{r}(\boldsymbol{x}_I)^T, \boldsymbol{p}(\boldsymbol{x}_I)^T\}\begin{Bmatrix}\boldsymbol{a}\\ \boldsymbol{b}\end{Bmatrix} \tag{22}$$

Here, $\boldsymbol{r}(x_I)$ is a radial basis function (RBF), $\boldsymbol{p}(x_I)$ is a polynomial basis function and parameters $\boldsymbol{a}$ and $\boldsymbol{b}$ are coefficients associated with $\boldsymbol{r}(x_I)$ and $\boldsymbol{p}(x_I)$ **,**respectively [25]. The polynomial basis enhances the stability and robustness of the RPIM shape functions. The Multiquadric Radial Basis Function (MQ-RBF) has been adapted to incorporate the spatial dimensions of the problem's domain, significantly enhancing its applicability and effectiveness [25]. Initially, the MQ-RBF was commonly recommended for RPIM applications in its original form, with shape parameters set to $c = 1.42$ and $p = 1.03$. These values were suggested in earlier literature as suitable for 2D analysis, providing acceptable results for many cases. However, Belinha [25] later refined the MQ-RBF to enhance its performance by optimizing the Kronecker delta property of the 2D RPIM shape functions. Through this process, it was found that reducing c to a value close to zero, though not being zero, and setting p to a value near one result in better accuracy and stability. The optimal parameters were determined to be $c = 10^{-4}$ and $p = 1 - 10^{-4}$. These adjustments allowed the RPIM to reproduce highly complex variable fields with greater precision [25]. Therefore, for a 2D domain, the refined MQ-RBF is expressed as (23):

$$r_j(\boldsymbol{x}_i) = r_{ij} = \left(d_{ij}^2 + (\widehat{w}_I \cdot c)^2\right)^p = \left(\left(\sqrt{\left(x_j - x_i\right)^2 + \left(y_j - y_i\right)^2}\right)^2 + (\widehat{w}_I \cdot c)^2\right)^p \tag{23}$$

In the early developments of the RPIM, it was established that ensuring a unique solution requires satisfying the condition in which $j = \{1,2,\dots,m\}$:

$$\sum_{i=1}^{n} p_j(\boldsymbol{x}_i) a_i(\boldsymbol{x}_i) = 0 \tag{24}$$

When combining equations (22) and (24), a new matrix can be built, with its parameters being presented as well:

$$\begin{bmatrix}\boldsymbol{R} & \boldsymbol{P}\\ \boldsymbol{P}^T & 0\end{bmatrix}\begin{Bmatrix}\boldsymbol{a}\\ \boldsymbol{b}\end{Bmatrix} = G\begin{Bmatrix}\boldsymbol{a}\\ \boldsymbol{b}\end{Bmatrix} = \begin{Bmatrix}\boldsymbol{u}_s\\ 0\end{Bmatrix} \tag{25}$$

$$\boldsymbol{u}_s = \{u_1, u_2, \dots, u_n\}^T \tag{26}$$

$$\boldsymbol{R} = \begin{bmatrix} r_{11} & r_{12} & \cdots & r_{1n} \\ r_{21} & r_{21} & \cdots & r_{2n} \\ \vdots & \vdots & \ddots & \vdots \\ r_{n1} & r_{n2} & \cdots & r_{nn} \end{bmatrix} \tag{27}$$

$$\boldsymbol{P} = \begin{bmatrix} p_1(\boldsymbol{x}_1) & p_2(\boldsymbol{x}_1) & \cdots & p_m(\boldsymbol{x}_1) \\ p_1(\boldsymbol{x}_2) & p_2(\boldsymbol{x}_2) & \cdots & p_m(\boldsymbol{x}_2) \\ \vdots & \vdots & \ddots & \vdots \\ p_1(\boldsymbol{x}_n) & p_2(\boldsymbol{x}_n) & \cdots & p_m(\boldsymbol{x}_n) \end{bmatrix} \tag{28}$$

Due to the fact that $\boldsymbol{R}$ is a symmetric matrix, $\boldsymbol{G}$ disposed of the same property. Therefore, when solving equation (25), the result is as follows:

$$\begin{Bmatrix} \boldsymbol{a} \\ \boldsymbol{b} \end{Bmatrix} = \boldsymbol{G}^{-1} \cdot \begin{Bmatrix} \boldsymbol{u}_s \\ 0 \end{Bmatrix} \tag{29}$$

Having the solved terms for the parameters $\boldsymbol{a}$ and $\boldsymbol{b}$ its now possible to replace them in equation (22), obtaining the following interpolation of $\boldsymbol{x}_I$:

$$\boldsymbol{u}(\boldsymbol{x}_I) = \{\boldsymbol{r}(\boldsymbol{x}_I)^{\boldsymbol{T}}, \boldsymbol{p}(\boldsymbol{x}_I)^{\boldsymbol{T}}\} \cdot \boldsymbol{G}^{-1} \cdot \begin{Bmatrix} \boldsymbol{u}_s \\ \boldsymbol{0} \end{Bmatrix} = \{\boldsymbol{\Phi}(\boldsymbol{x}_I), \boldsymbol{\Psi}(\boldsymbol{x}_I)\} \cdot \begin{Bmatrix} \boldsymbol{u}_s \\ \boldsymbol{0} \end{Bmatrix} \tag{30}$$

In equation (30), $\Phi(\boldsymbol{x}_I)$ represents the interpolation function of $\boldsymbol{x}_I$:

$$\boldsymbol{\Phi}_{\xi}(\boldsymbol{x}_I) = \{\boldsymbol{r}(\boldsymbol{x}_I)_{\xi}^{T}, \boldsymbol{p}(\boldsymbol{x}_I)_{\xi}^{T}\} \cdot \boldsymbol{G}^{-1} \tag{31}$$

Radial point interpolating functions maintain the partition of unity and fulfil the Kronecker delta property, enabling straightforward application of boundary conditions [25].

3.4. System of equations

The formulation of the global system of equations for elasticity problems is grounded in the virtual work principle. This principle ensures equilibrium by stating that the internal forces' contribution to the virtual work must match the external forces' contribution. The problem's domain, denoted as Ω, encompasses both the internal volume and its boundaries, where forces and constraints are applied [27]. All the following equations are related for both RPIM and NNRPIM methods. Therefore, this section applies for both techniques. The boundary Γ is split to Γ_t, which specifies natural boundary conditions, and Γ_u, which defines essential boundary conditions. Additionally, uniform body forces b may act over the entire domain Ω. This balance of forces is described by equation (32):

$$\int_{\Omega} \delta\boldsymbol{\varepsilon}^T \cdot \boldsymbol{\sigma} \cdot d\Omega = \int_{\Omega} \delta\boldsymbol{u}(\boldsymbol{x}_I)^T \cdot \boldsymbol{b} \cdot d\Omega + \int_{\Gamma_t} \delta\boldsymbol{u}(\boldsymbol{x}_I)^T \cdot \bar{\boldsymbol{t}} \cdot d\Gamma \tag{32}$$

In order to fully represent equation (32), both displacements components $\{u, v\}$ are necessary. If added, equation (33) is obtained:

$$\boldsymbol{u}(\boldsymbol{x}_I) = \begin{Bmatrix} u(\boldsymbol{x}_I) \\ v(\boldsymbol{x}_I) \end{Bmatrix} = \boldsymbol{H}(\boldsymbol{x}_I) \cdot \boldsymbol{u} = \begin{bmatrix} \phi_1(\boldsymbol{x}_I) & 0 & \cdots & \phi_n(\boldsymbol{x}_I) & 0 \\ 0 & \phi_1(\boldsymbol{x}_I) & \cdots & 0 & \phi_n(\boldsymbol{x}_I) \end{bmatrix} \cdot \begin{Bmatrix} u_1 \\ v_1 \\ \vdots \\ u_n \\ v_n \end{Bmatrix} \tag{33}$$

Equation (33) can now be translated as a deformation vector, represented in equation (34):

$$\boldsymbol{\varepsilon}(\boldsymbol{x}_I) = \boldsymbol{L} \cdot \boldsymbol{u}(\boldsymbol{x}_I) = \begin{bmatrix} \frac{\partial}{\partial x} & 0 \\ 0 & \frac{\partial}{\partial y} \\ \frac{\partial}{\partial y} & \frac{\partial}{\partial x} \end{bmatrix} \cdot \Phi(\boldsymbol{x}_I) \cdot \boldsymbol{u} = \boldsymbol{B}(\boldsymbol{x}_I) \cdot \boldsymbol{u} = \boldsymbol{B}(\boldsymbol{x}_I) \cdot \begin{Bmatrix} u_1 \\ v_1 \\ \vdots \\ u_n \\ v_n \end{Bmatrix} \tag{34}$$

The stress at an integration point $\boldsymbol{x}_I$ can be computed using Hooke's law, represented as equation (35):

$$\boldsymbol{\sigma}(\boldsymbol{x}_I) = \boldsymbol{c}(\boldsymbol{x}_I) \cdot \boldsymbol{\varepsilon}(\boldsymbol{x}_I) = \boldsymbol{c}(\boldsymbol{x}_I) \cdot \boldsymbol{B}(\boldsymbol{x}_I) \cdot \boldsymbol{u} \tag{35}$$

Here, the matrix $\boldsymbol{c}(\boldsymbol{x}_I)$ characterizes the material's constitutive properties and depends on the material mechanical parameters at $\boldsymbol{x}_I$. For two-dimensional problems under plane stress conditions, these mechanical parameters include E_i, G_{ij} and υ_{ij}. Also, some coefficients are key when defining the matrix: $\alpha_1 = E_1/E_1$; $\alpha_2 = G_{12}/E_2$; $\alpha_3 = 1 + \upsilon_{12}$; $\alpha_4 = 1 - \upsilon_{12} - 2 \cdot \alpha_1 \upsilon_{21}$. Utilizing the previous coefficients, matrix is constructed as follows [27]:

$$\boldsymbol{c} = \frac{E_2}{1 - \alpha_1 \cdot \upsilon_{21}^2} \begin{bmatrix} \alpha_1 & \alpha_1 \cdot \upsilon_{12} & 0 \\ \alpha_1 \cdot \upsilon_{12} & 1 & 0 \\ 0 & 0 & \alpha_2 \cdot (1 - \alpha_1 \cdot \upsilon_{21}^2) \end{bmatrix} \tag{36}$$

By redefining the stress and strain vectors, equation (32) can be reformulated. This leads to equation (37):

$$\int_{\Omega} \delta(\boldsymbol{B}(\boldsymbol{x}_I) \cdot \boldsymbol{u})^T \cdot (\boldsymbol{c}(\boldsymbol{x}_I) \cdot \boldsymbol{B}(\boldsymbol{x}_I) \cdot \boldsymbol{u}) \cdot d\Omega = \int_{\Omega} \delta\,(\boldsymbol{H}(\boldsymbol{x}_I) \cdot \boldsymbol{u})^T \cdot \boldsymbol{b} \cdot d\Omega + \int_{\Gamma_t} \delta\,(\boldsymbol{H}(\boldsymbol{x}_I) \cdot \boldsymbol{u})^T \cdot \overline{\boldsymbol{t}} \cdot d\Gamma \tag{37}$$

Here, the terms account for internal forces within the domain Ω, body forces distributed across the domain and external forces applied to the boundary Γ_t [27].

3.5. Bone remodelling

Bone mechanical behaviour is characterized by a direct relationship between apparent density and material properties such as Young's modulus and ultimate compressive strength. These properties vary continuously within the tissue according to specific mathematical laws derived from experimental observations, capturing the distinct behaviours of cortical and trabecular bone. The evolution of mechanical properties is thus intrinsically tied to local variations in density, enabling a gradual adaptation of the tissue.

Bone remodelling is regulated by the distribution of the strain energy density. In each iteration, the mechanical stimulus is assessed across the domain, and only the regions where the stimulus falls outside a defined optimal range undergo modifications in density. The new apparent density at each point is determined based on the principal stresses, ensuring that the tissue strengthens or resorbs locally in response to mechanical demands. Material properties are

updated accordingly, and the stiffness tensors are realigned with the new stress directions. This iterative process continues until a state of equilibrium is reached, where either the global density stabilizes, or a predefined target density is attained. Through this mechanism, bone architecture progressively adapts, optimizing itself to the prevailing mechanical environment. In Figure 18 it's possible to observe the bone tissue remodelling algorithm, described previously.

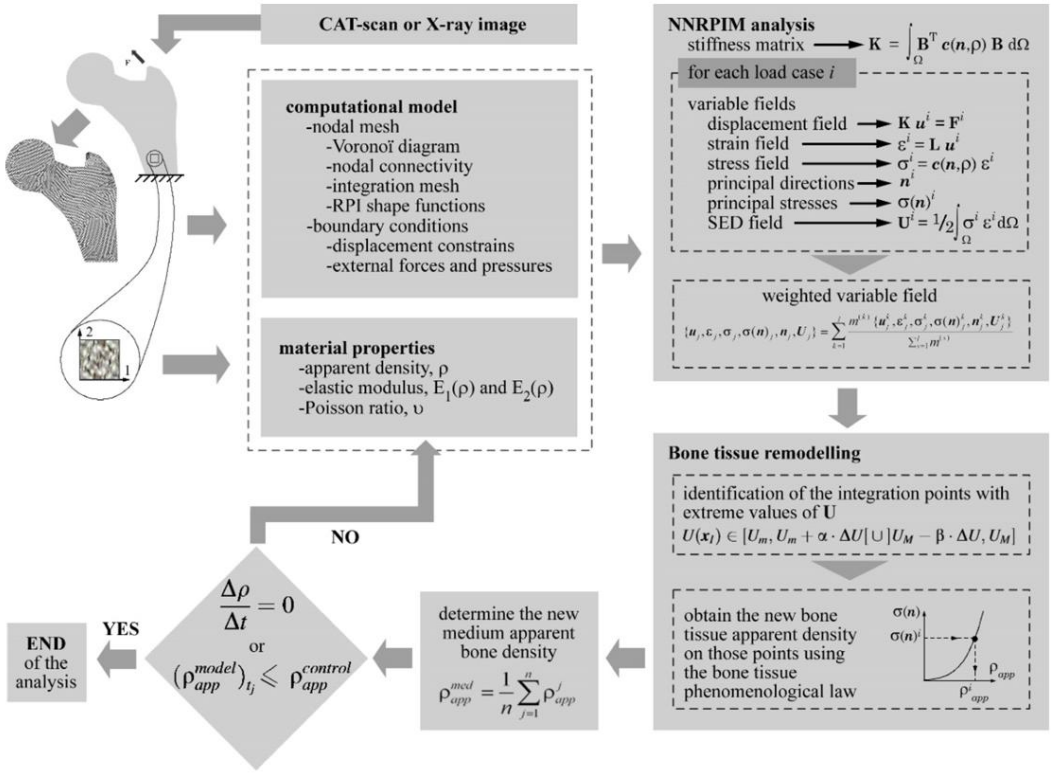

Figure 18. BONE remodelling algorithm [28]

3.6. Bi-directional Evolutionary Structural Optimization

The Bi-directional Evolutionary Structural Optimization (BESO) method works by iteratively updating the material distribution in a structure based on its stress reaction. At each iteration, a structural analysis is performed in order to compute the stress field, and using the information produced, the algorithm searches for areas to reinforce, being the ones with the highest stress value, whereas the lower stress regions are penalized. This material update is governed by a penalty parameter that continuously adjusts the material state at each point, ranging from nearly solid to almost empty. A fixed portion of the domain experiencing the highest stress is reinforced by assigning it full material properties, while a portion with the lowest stress is penalized, reducing its stiffness to simulate material removal.

After each iteration, the structure is re-analysed, and the process repeats itself. If the average stress increases significantly between iterations, the algorithm temporarily focuses only on reinforcing critical areas to restore stability. This iterative process continues until the structure

converges to a much stable layout, with material only applied in the most critical and structural efficient regions. The BESO algorithm is summarized in Figure 19.

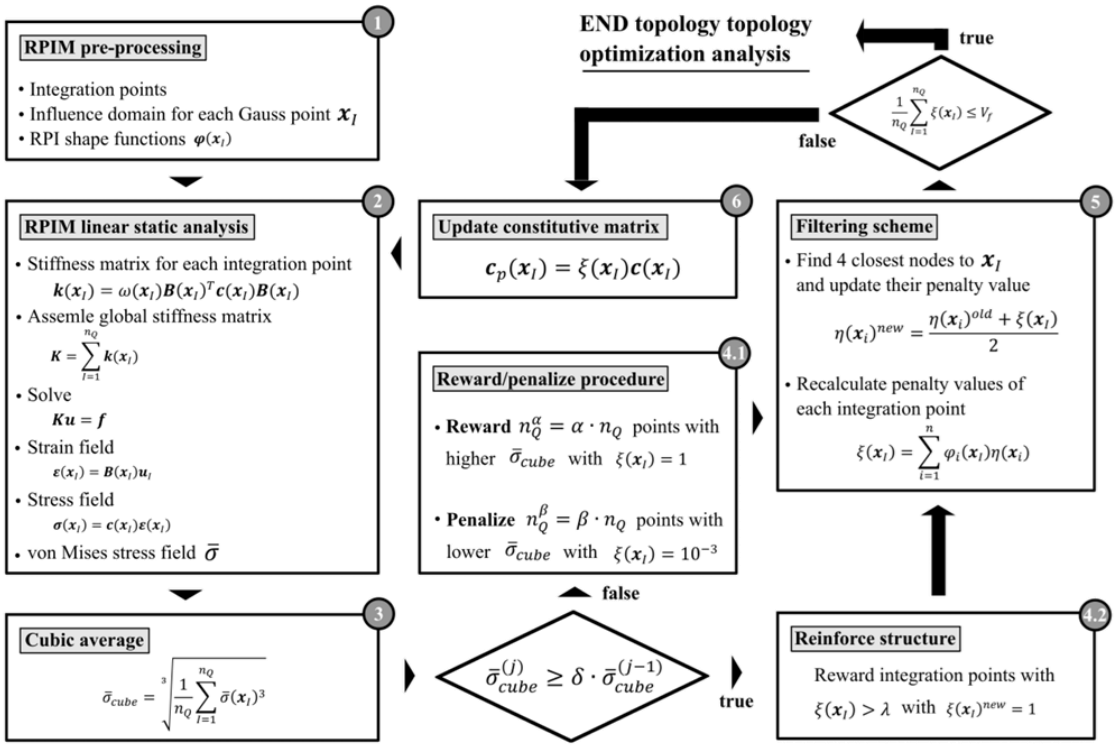

Figure 19. BESO algorithm [29]

4. COMPUTATIONAL APPLICATIONS

This chapter provides a detailed explanation of the evolution and recent innovations in numerical techniques used for scientific modelling and engineering analysis. It focuses on the finite element method (FEM), highlighting its importance and discussing its inherent limitations, which have led to the emergence of Meshless Methods (MMs). The chapter also demonstrates the real-world application of these approaches in space technology, featuring case studies that explore areas like soil-wheel dynamics and detailed assessments of exploration Rovers.

4.1. Finite element method

In the past eighty years, the finite element method (FEM) has become a fundamental tool in computational analysis, revolutionizing engineering design and scientific modelling across a wide range of physical processes. FEM is widely used to model and solve a wide variety of problems including material and structural mechanics, fluid flow, heat transfer, medical diagnostics and surgical planning, electromagnetics, semiconductor design and many others that rely on partial differential equations (PDEs) [30]. To solve problems, the domain is divided into a network of discrete nodes, which are linked together by what are referred to as elements. The beginning of the finite element method dates to the year 1941. The earliest example of mesh discretization came from A. Hrennikof, a Russian-Canadian structural engineer, who introduced a lattice framework for membrane and plate models. In this work [31], he divided the solution domain into a mesh using a lattice structure. The continuous developments achieved by engineers enhanced previous methods by the early 1950s. Such made it possible to solve practical issues occurring in civil and aeronautical industries. M. J. Turner, R. W. Clough, H. C. Martin and L. J. Topp were the creators of this new method, the Matrix Stiffness Method [32], while working in the Boeing company in 1954. Throughout the years, engineers (Szabo and Babuska) discovered that FEM converges exponentially as the mesh is refined with an appropriate combination of h-refining, which consists of the division of elements into smaller dimensions, and p-refining which increases their polynomial order [30]. Comparing to most FEM methods previously discovered, exponential convergence proved to be significantly beneficial, since other methods only converge at a numerical rate [30]. Figure 20 illustrates the exponential rate at which finite elements-related papers are increasing. The graph was created utilizing ScienceDirect®, searching for “finite element methods” and defining the interval of years from 1966 to 2024.

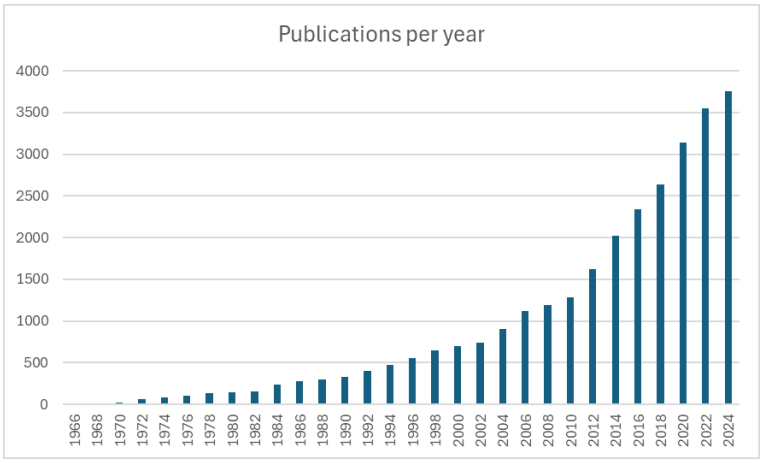

Figure 20. Finite Element Publications per year since 1966 [33]

4.2. Meshless methods

Finite elements do have advantages when it comes to solving problems, however they present some limitations as well. Since these methods rely solely on meshed-based interpolation, it can result in a higher probability of errors. In some cases, the mesh becomes distorted and require remeshing, a process that is both time consuming and intensive. Additionally, for complex three-dimensional shapes might not be feasible [34]. Meshless methods, as the name suggests, eliminate the need for meshes since the properties required are determined at the nodes. The first meshless method was discovered in the 1970s by Gingold Monghan and Lucy, for numerical simulation of astrophysical problems without any boundaries. The method was called Smooth Particle Hydrodynamics (SPH) [35]. However, SPH was inconsistent in satisfying various conditions when solving problems. Therefore, the Element free Galerkin Method (EFGM) was developed by Ted Belytschko [35]. To overcome boundary-related issues and stability challenges in standard SPH, the Reproducing Kernel Particle Method (RKPM) was introduced as an improved version of the SPH. Throughout the years, various types of methods were developed however the Meshless Local Petrov-Galerkin (MLPG), discovered by Zhu, Zhang and Atluri, was one of the most relevant. The MLPG is genuinely meshless, as it does not require finite elements or boundary element meshes for interpolating the trial and test functions of the solution variables or for integrating the weak-form, whether symmetric or not [36]. Meshless methods offer several key advantages such as: h-adaptivity is easier to implement, they handle problems with moving discontinuities, they are more robust when managing large deformations and they allow for higher-order continuous shape functions. Yet, MMs have some drawbacks, including the need for higher-order integration due to their rational and handling complexity of essential boundary conditions, as their shape functions are not direct interpolants [34]. According to Figure 21, it's possible to observe the increase in the number of publications about meshless methods. The graph was created utilizing ScienceDirect®, searching for "meshless methods" and defining the range of years from 1996 to 2024.

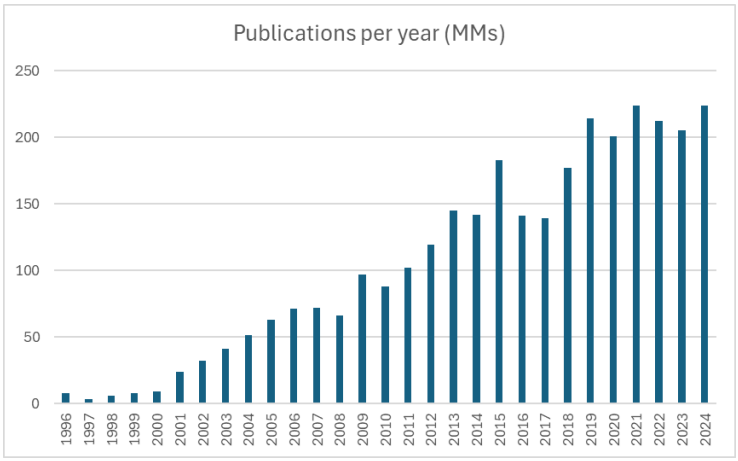

Figure 21. Meshless Methods Publications per year since 1996 [37]

4.3. Numerical methods applied in space technology

To support advancements in space studies and spacecraft developments, numerical methods have played a crucial role. This section, highlights recent applications of numerical methods applied in space industries, emphasising the use of these technologies in space.

4.3.1. Wheels-soil interaction

For planetary exploration, a mobile robot must be capable of navigating diverse soil types consistently. Maintaining rover mobility is crucial for gathering scientific data and observations. When mobility is compromised, the rover's potential for discovery is exponentially reduced [38]. Some factors that might influence the rover's mobility are sinkage and slippage events. To prevent failures, researchers in 2012 conducted an in-depth study of how rover wheels interact with Martian soil utilizing meshfree methods, with more precision the Reproducing Kernel Particle Method (RPKM) [38]. In this work, a simulation model was developed with a rigid wheel interacting with a meshfree soil domain. In this setup, the wheel rotates while applying a controlled vertical load onto the soil. To establish a basis for the meshfree analysis, an initial benchmark simulation was conducted in LS-Dyna using standard Lagrangian meshing for the soil [38]. Both numerical tests are shown in Figure 22. Finally, both results achieved, are compared to a classic pressure-sinkage method, Bekker's equation and it was possible to observe that the curves acquired from the RPKM align more closely to the one referred to previously [38]. This suggests that meshfree solutions produce more accurate results than the Lagrangian form.

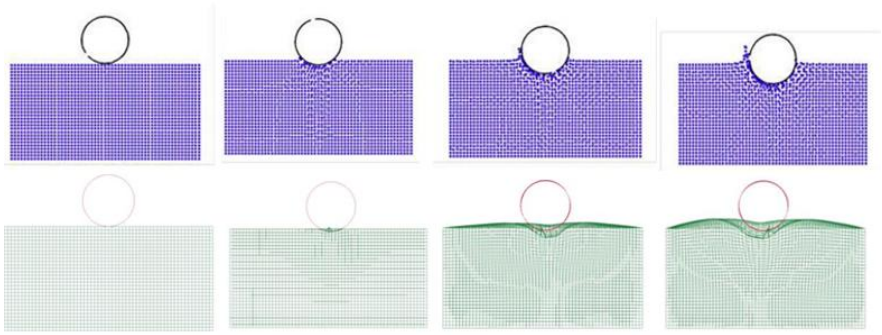

Figure 22. RPK simulation (blue) and Lagrangian simulation (green), adapted from [38]

The conclusion of this study prompted a focused investigation into slippage in 2015, since this factor highly challenged the mobility of rovers when exploring planetary surfaces [39]. Despite all the experiments done, some occasional problems have occurred, for example Opportunity encountered significant wheel sinkage and rover slippage while attempting to cross wind-blown sand ripples [39]. To address these challenges the Massachusetts Institute of Technology (MIT) research team used discrete element method (DEM) to simulate the complex interactions between the rover wheels and the soil, particularly under high-slip environments. Additionally, MIT conducted a laboratory test on a spare wheel on a simulated Martian soil, which mimics it's mechanical properties [39]. The experiments adjusted load, wheel rotation and slip conditions to compare to the results obtained when conducting the DEM simulations. To represent the soil resistance, tri-sphere particles are used in DEM simulation, including particle compaction and friction [39]. The numerical test was conducted using a range of slip values (i=0,0.1,0.3,0.5) which were then fine-tuned to fit measure experimental data (i=0.7,0.9,0.99) [39]. Upon completing all the tests, it's possible to conclude that the 3D DEM simulations successfully captured the drawbar pull particularly under slip ratios of 0.5 and 0.7 since in high-slip conditions, where soil resistance relies more on friction than particle interlocking, the predictions closely align with the experimental data [39]. Both studies discussed previously focus primarily on the interaction between wheels and the planetary soil. Since slippage highly affects rover's mobility and ability to explore, in 2020 flexible metal wheels were studied since they exhibit improved traction [40]. While maintaining balance when turning and preventing sinking are key considerations in wheel design, the primary focus of this study was on ensuring the wheels could withstand heavy loads and provide stable steering. The wheel design sought to achieve an optimal balance of strength and flexibility. Emphasis was placed on maximizing ground contact area by leveraging elastic deformation while preventing any plastic deformation. The structure featured a single sturdy rim supporting two flexible carcasses positioned side by side, each composed of 36 evenly spaced spring steel sheets [40]. FEM simulations were employed to fine tune the wheel dimensions by simulating static loads, such as vertical, tangential and side forces and impact loads. These simulations, aimed to optimize the thickness of the carcass sheets while assessing the wheel's stress tolerance, deformation and strength. The simulation data was subsequently compared with physical test outcomes [40]. The carcass material featured a Young's modulus of 200 GPa, a yield strength of 1500 MPa and a Poisson's ratio of 0.288 [40]. The vertical load simulation was done for three thicknesses (1.3,1.5,1.7 mm) using loads of 7500N and 15000N. While simulating with the 1.3mm for both

loads applied, it is analysed that in both situations the maximum stress surpasses the maximum yield strength. For the other dimensions, when subjected to 15000N, they all exceed the yield strength. Therefore, it is feasible to use 1.5 or 1.7 mm of thickness [40]. Analytical calculations determined that the maximum thrust under nominal load reached 6305N [40]. To test the carcass flexibility and durability under this load, the tangential force was applied while holding the rim stationary. Results indicate that deformation reaches its maximum at 7mm with the highest stress recorded at 715.5MPa [40]. Equations within the resolution estimated that the side force under nominal load would reach 1906N. A side force was applied at the contact point while the rim was in a stationary position, to simulate the turning conditions. Results acquired show that these conditions led to a displacement of 12.9 mm and a maximum stress of 433.2 MPa, confirming that no plastic deformation would occur [40]. Test showed the wheel's strong load capacity, stiffness and resilience under dynamic conditions. Compared to the woven wire wheel used in lunar rovers, this design's twin metal carcasses and spring steel plates improved reliability and load support. Physical tests indicate higher load tolerance than simulations [40].

4.3.2. Rover Structural Components

Examining wheel-soil interaction is essential for optimal performance yet analysing other structural elements of the rover is equally important. In 2016, a FEM analysis, using ANSYS, was conducted on a rover chassis to evaluate its behaviour under stress, fatigue and heat transfer conditions [41]. The mesh in this analysis was refined around areas where the chassis integrates with other platform components and around notches since these locations are prone to stress concentration. The two scenarios analysed were the application of a bending force to the front wheels and another where the impact from a potential fall by applying a strong force to the center frame profile is simulated [41]. This analysis provided insight into areas requiring reinforcement, helped to evaluate the suitability of adding lightening holes and identified potential design optimizations. Stress values at key points were also examined to ensure they remained within the material's elastic limit, emphasizing the need for strong welded joints [41]. Analyzing the chassis is key to ensuring that the rover functions optimally, since it is one of the main structural components, however other elements must also be examined. Therefore, in 2017 a rover manipulator was numerically and geometrically tested, to achieve weight optimization [42]. The manipulator exhibits six degrees of freedom and is composed of a gripper, four arms, three linear engines and a shock absorber, with all these elements being constructed with various materials (Steel S185, Aluminium alloy 2017 and Acrylonitrile butadiene styrene (ABS)) [42]. To evaluate the performance of the manipulator when in operation, three computational models simulating different loading scenarios were employed using FEM analysis. All three computational models are shown in Figure 23. The first and third models applied 50N at the lower part of the gripper to study the object transportation and the handling capacity of the manipulator. Meanwhile, the second model was created to simulate a pulling motion of 20 kg [42]. When considering all the scenarios, an automatically generated finite element mesh was used, and the system was secured to the base of the manipulator. The FEM results led to various conclusions. Despite ABS being the lightest material, when considering the first and the third models, it showed a lack in structural integrity since under

the 50N load, substantially exceeding feasible values of stress and strain. Even though, when utilizing Aluminium and Steel, the maximum yield strength is also surpassed, however this exceedance is typically minimal [42]. The strength analysis confirms that both structural steel and aluminium alloys are feasible options when building the manipulator, providing the capacity to handle items up to 5kg in any configuration. The production of the manipulator consisted of using aluminium, however ABS could be used in applications in which object transport is not involved. The designed manipulator was used in multiple tasks and all components remained intact, confirming the reliability of the design [42].

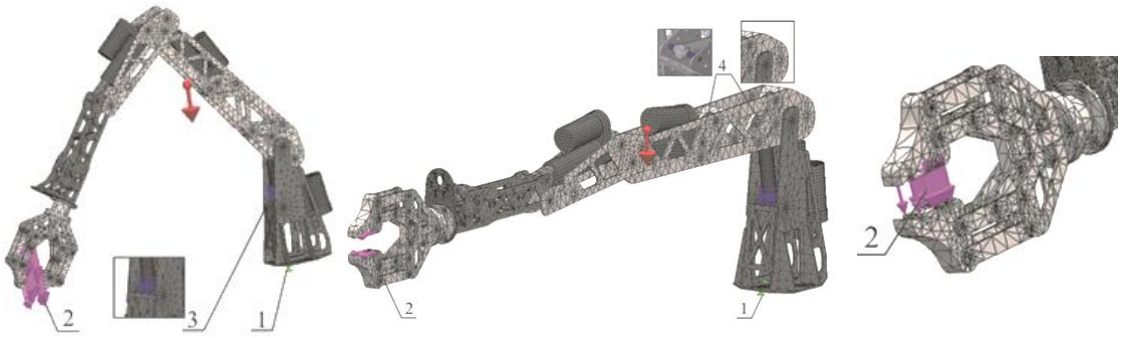

a) b) c)

Figure 23. Different computational models: a) first; b) second; c) third (adapted from[42])

Evaluating how structural elements behave under certain conditions is important, however analysing power supplies is also key. Therefore, in 2018, the Laser Power Supply (LPS) of the 2020 Mars Rover was numerically examined utilizing a transient thermal analysis as well as a Steinburg fatigue analysis [43]. The LPS grants energy to the Ultraviolet (UV) laser that with the emission of a focused dot of UV light, targets specific areas. Such interaction generates a unique glow, if molecules contain carbon rings, potentially revealing whether ancient life was preserved [43]. The LPS faces considerable challenges, including high power dissipation and stringent dielectric isolation, as Mars' environment presents extreme temperature variations. To overcome such inconveniences, a comprehensive multi-physics simulation was developed that considered temperature-dependent material properties. Moreover, a steady-state analysis utilizing finite elements, while considering Martian gas and thermal radiation, was executed, however the thermal analysis will just be discussed in chapter 4.3.3 [43]. A structural analysis was conducted on the LPS assembly, applying a random vibration spectrum of the Atlas V launch environment [43]. Using a damping of 2%, the spectrum is applied in the critical direction. The deflection of the Printed Wiring Assembly (PWA) was evaluated for vibration fatigue of 20 million cycles which is equivalent to 8 hours of vibration at a frequency of 783 Hz. This analysis proved that the LPS presented no issues when subjected to random vibration environments [43]. In chapter 2.3.1.1 a brief explanation about how wheeled vehicles work, and its suspension system was documented. The most implemented system, and the one used in the Perseverance Rover, is the rocker-bogie, subject of analysis in 2021. Utilizing Finite Elements the suspension of the rover was structurally investigated and the design was validated [44]. With the assistance of the Finite Element Analysis (FEA) software, structural optimization is feasible since critical zones, due to areas of high stress concentrations or oversized elements, which add unnecessary

weight to the rover, are identified [44]. According to the results obtained, the factor of safety was determined to be 11.987, which means all elements remain within the elastic range based on the Von Mises analyses [44]. The Von Mises stress and the Global factor of safety using FEA software can be observed in Figure 24. To observe the rovers' behaviour when encountering obstacles and varying soils, similar to those of Mars, a transient analysis was conducted. This computational examination, analyses the rover's stability, focusing on factors such as the movement of the centre of mass, velocity and suspension behaviour when travelling uneven terrain [44]. The results ensure the reliability of the rocker-bogie suspension, preventing rollover and providing smooth movement [44]. This study complements those discussed in the section 4.3.1, since the wheels analysis proved to minimize sinkage and slippage. Therefore, if integrating the data obtained when studying the wheel-soil interaction along with the suspension system findings, it is possible to achieve the most optimal rover design, incorporating results from other numerical projects discussed as well.

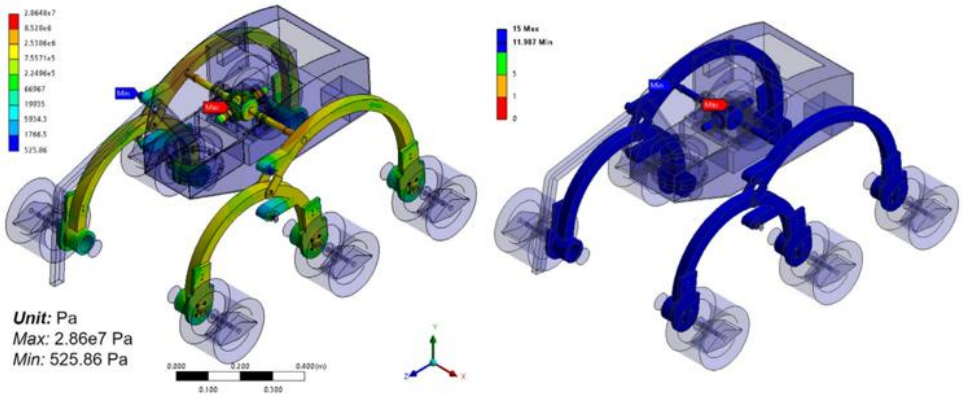

a) b)

Figure 24. Different FEA analysis: a) Von Mises stress; b) Global factor of safety (adapted from [44])

4.3.3. Thermal and fluid analysis

As it was stated previously, the existence of dust in Mars is significant. Therefore, in 2016 as well, a dust wind tunnel was designed and numerically investigated. This study uses Computational Fluid Dynamics (CFD) in FLUENT (software) to model gas-only and gas dust flows under Martian conditions [45]. Geometric modelling and meshing were conducted with Pro-Engineer and ICEM CFD, using a symmetric approach to reduce computational load. The innovative Secondary Injector System (SIS) was incorporated to enhance recirculating flow and particle distribution [45]. The results demonstrate that the SIS greatly enhances the flow control and consistency within the wind tunnel. When operating in gas-only mode, the addiction of SIS made possible to achieve flow speed that matched design targets since the deviation was only 4%. On the contrary, without the SIS systems, the deviation would be 17%. Additionally, by utilizing SIS is possible to maintain a constant particle concentration which enables the necessary dust distribution when in Martian terrain. It also helped to reduce the turbulence along tunnel walls [45]. As it was referred in chapter 4.3.2 the thermal analysis of the LPS will be discussed in this section. The Printed Wiring Board (PWB) was evaluated through a transient

study to ensure that the operating cycle of 50% of the maximum power was acceptable [43]. The laser is designed to operate with 40 usec pulses, with 10 second duration for both on and off times. The purpose of this numerical analysis is to assess how the temperature varies, with the aim of potentially reducing the on and off cycles [43]. The thermal analysis indicates that the peak temperature reached is 112.4°C [43]. A comparable study from 2018, focusing on NASA's Mars 2020 Rover, also applied a combination of experimental and numerical methods to examine the effects of the rover's presence on environmental data collection, particularly for the wind sensors of the Mars Environmental Dynamics Analyzer (MEDA) [46]. The methodology included wind-tunnel experiments with a 1:10 scale rover model and computational fluid dynamics (CFD) simulations. Wind-tunnel tests involved visualizing airflow with the assistance of smoke and particle image velocimetry (PIV) to map the velocity field surrounding the rover [46]. These velocity fields can be seen in Figure 25. The results obtained served as a benchmark for CFD simulations conducted using the FloEFD software.

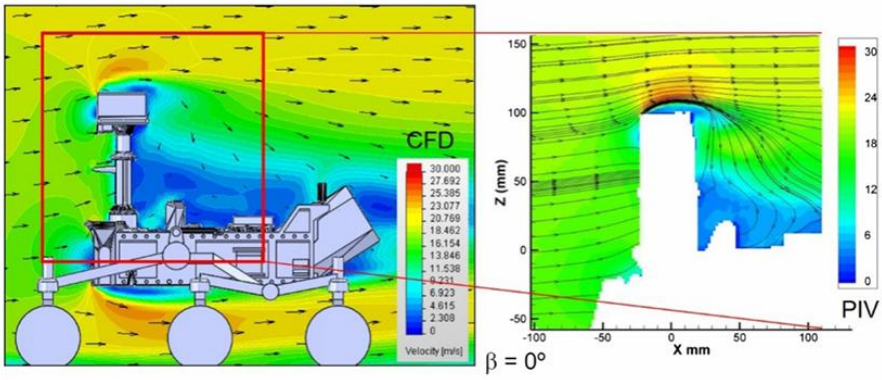

Figure 25. Flow velocity surrounding the rover using CFD and PIV [46]

The rover model exhibited a mesh with 2.7 million cells across fluid and solid domains, allowing both laminar and turbulent flow simulations. The model focused on critical areas such as the MEDA wind sensors built on the rover mast. The simulations aimed to replicate and predict the airflow behaviour around the vehicle to analyse how the rover's structure can cause wind perturbation, especially in areas where flow separation is existent [46]. The study identified two distinct flow regions surrounding the rover. For instance, in the Upstream region, the rovers caused the airflow to slightly curve, affecting the measurements taken by the wind sensor. On the contrary, in the downstream region the flow becomes separated, creating a wake pattern characteristic of bluff bodies [46]. Results obtained from CFD compared to PIV's show that simulations accurately predicted upstream regions with despicable error of 5%. However, where turbulence was more pronounced (downstream regions), substantial differences were observed, exceeding 40% of error [46]. These findings indicate that CFD methods can precisely predict the behaviour of the airflow in attached areas, or mainstream regions, however further refinement is necessary when analysing separated flow areas. Overall, the study supports the use of CFD to correct the rover's wind sensors data, suggesting that improved calibration techniques can ensure measurement accuracy in Mars's challenging environment [46].

5. PRELIMINARY NUMERICAL STUDIES

In this section, an elasto-static analysis of a cantilever beam is posed and described operating with the FEM, RPIM and NNRPIM methods. Subsequently, the results obtained with the finite element and meshless methods are compared to the analytical solution. To assess the accuracy of the methods previously stated, the analysis is performed in both two and three dimensions.

5.1. Cantilever beam

Using finite element and meshless methods, a convergence test was conducted when performing an elasto-static analysis of a benchmark example of a cantilever beam in 2D as well as 3D. The assumed material properties are as follows: a Young's modulus (*E*) of 1000 Pa and a Poisson's ratio (υ) of 0.3. Initially, it is necessary to define the analytical equations for displacements (equations(38) and (39)) and stresses (equations (40) and (41)), that will later serve as comparison to the numerical results obtained. The cantilever beam has the height of D=1m, and a length of L=2m. Then, it is possible to determine the beam's moment of inertia as $I = \frac{D^3}{12}$. Finally, it is applied a distributed load of 1N/m.

$$u(x) = -\frac{2P}{E \cdot D^3}\left[3x \cdot (2L - x) \cdot y + (2 + \upsilon) \cdot \left(y^2 - \frac{D^2}{4}\right) \cdot y\right] \tag{38}$$

$$v(x) = \frac{2P}{E \cdot D^3}\left[x^2 \cdot (3L - x) + 3\upsilon \cdot (L - x) \cdot y^2 + x \cdot (4 + 5\upsilon) \cdot \frac{D^2}{4}\right] \tag{39}$$

$$\sigma_{xx}(x) = -\frac{P \cdot (L - x) \cdot y}{I} \tag{40}$$

$$\sigma_{xy}(x) = \frac{P \cdot D^2}{8I} \cdot \left(1 - \frac{4y^2}{D^2}\right) \tag{41}$$

It is important to note that the horizontal displacement ($u(x)$) will not be used in convergence studies, since it is approximately null.

5.1.1. Cantilever beam 2D analysis

Taking into consideration plane stress conditions, it is possible now to analyse the cantilever beam with a two-dimensional approach. As it was stated previously, FEM, RPIM and NNRPIM methods were employed. Initially, in the FEM study both quadrilateral and triangular elements were utilized in order to form the mesh structure of the beam. For the RPIM method, the same mesh defined for the FEM was used as the background integration mesh, however the influence domains were defined by 16 nodes with Gaussian integration. Finally, in the NNRPIM analysis, both the first-degree and second-degree influence cells and full integration were implemented. In order to achieve the most precise results, in the RPI functions, c and p parameters were defined as follows: $c = 0.0001$ and $p = 0.9999$. With the simulation parameters finalized, modelling and analysis of the cantilever beam can now proceed. The dimensions of the beam were stated previously, however it also important to note that in the 2D analysis, a thickness of 1 meter is assigned. An essential boundary condition will be applied on the left side making left edge completely restrained in both the *x* and *y* directions. Additionally, a natural boundary condition will impose a downward distributed force of 1 N/m. An illustration of the Cantilever beam is presented in Figure 26. The selected points serve as reference locations for different types of analysis. At point A, the vertical displacement ($v(x)$) is verified, while in point B is evaluated the shear stress ($\sigma_{xy}(x)$) and point C analyses the normal stress ($\sigma_{xx}(x)$). The coordinates of the points shown in Figure 26 are presented in Table 2.

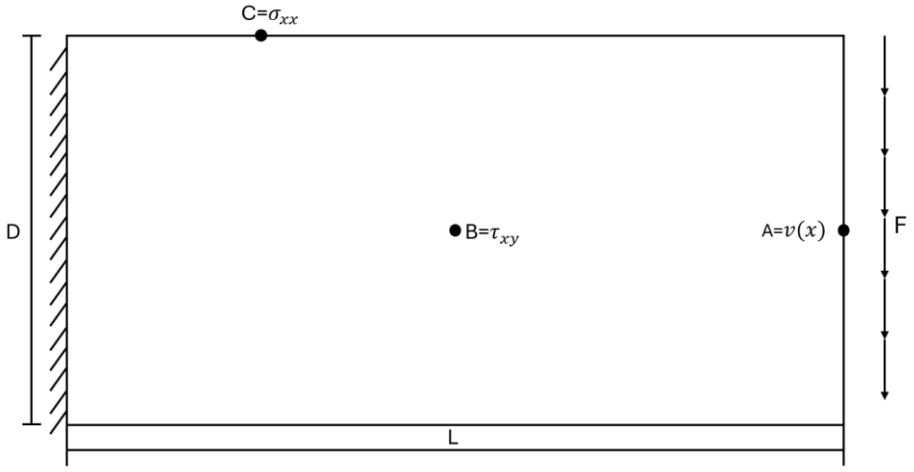

Figure 26. Sketch of the Cantilever Beam

Table 2. Coordinates

Points	*x* [m]	*y* [m]
A	2	0
B	1	0
C	0.5	0.5

As it was previously stated, the main objective of this study was to produce a convergence test. Therefore, it is necessary to progressively increase the number of divisions while consequently increasing the total number of nodes. Initially, the beam is divided into 4 divisions along the *x*-

axis and 2 divisions along the *y*-axis. These divisions are then sequentially doubled along both edges of the beam, allowing for the generation of all the configurations presented in Table 3. Moreover, Figure 27 presents some examples of the mesh used in the simulations.

Table 3. Divisions and number of nodes

Divisions	Number of nodes
4×2	15
8×4	45
16×8	153
32×16	561
64×32	2145
128×64	8385

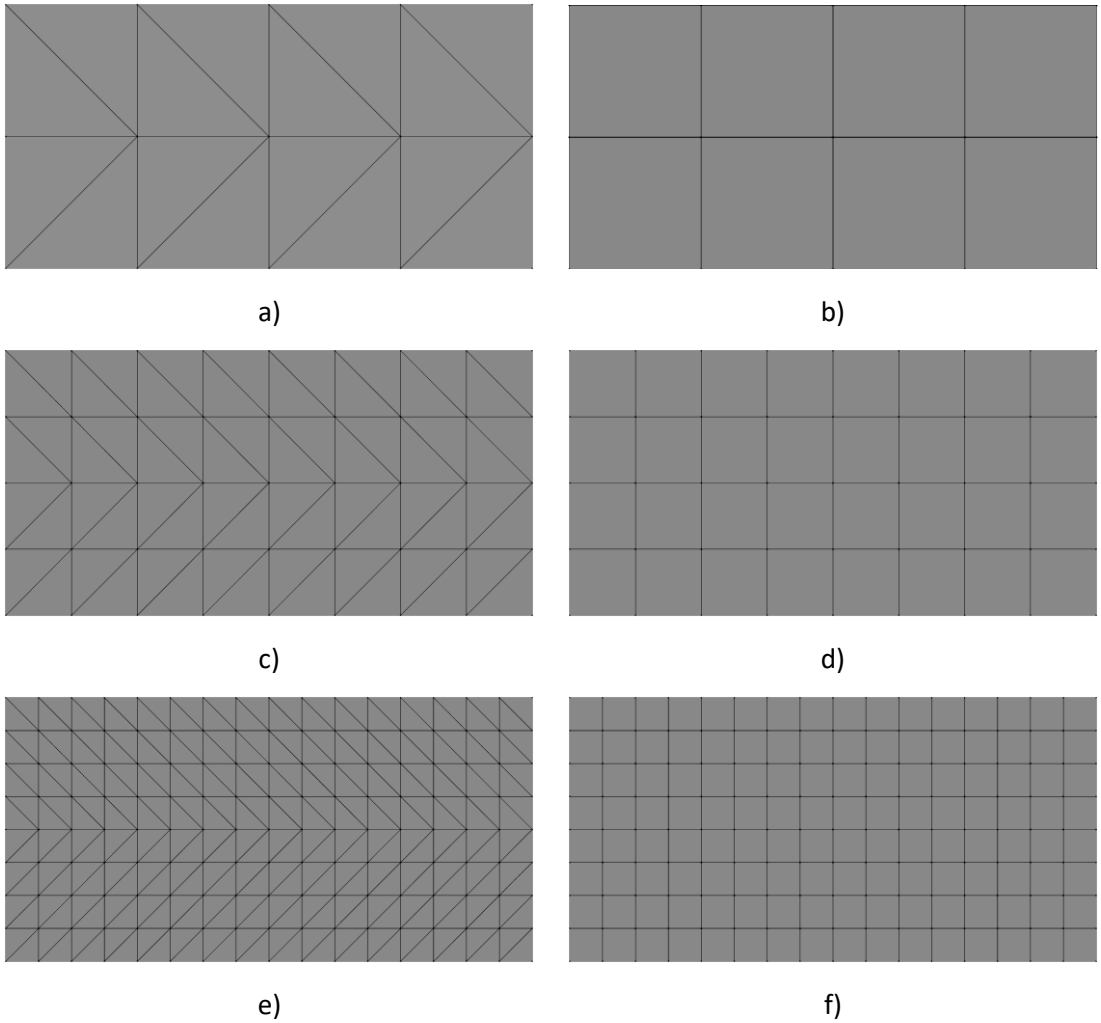

Figure 27. 2D Mesh divisions. a) triangular 4×2; b) quadrangular 4×2; c) triangular 8×4; d) quadrangular 8×4; e) triangular 16×8; f) quadrangular 16×8

With the modelling step completed, the results obtained from the simulations can now be analysed and compared to the analytical solution. If the results show convergence, it confirms that the methods used to study the cantilever beam, and subsequently the NASA rover, are reliable and accurate. Examining the vertical displacements graphs, presented in Figure 28a)

and Figure 28b) it is notable that every method converges toward the analytical solution, however the NNRPIM method demonstrates the highest accuracy, since it is the one that achieves convergence with fewer number of nodes, when compared to the others. Such is possible to observe, when examining the shear stress graphs presented in Figure 29a) and Figure 29b). In contrast, when analysing the normal stress graphs shown in Figure 30a) and Figure 30b), it becomes evident that the method that shows the fastest convergence is FEM using triangular elements.

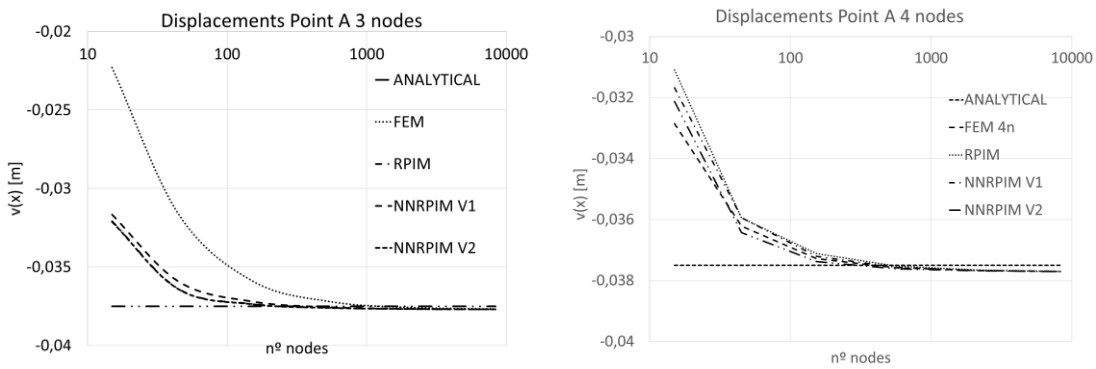

a) b)

Figure 28. a) Displacements in triangular mesh; b) Displacements in quadrangular mesh

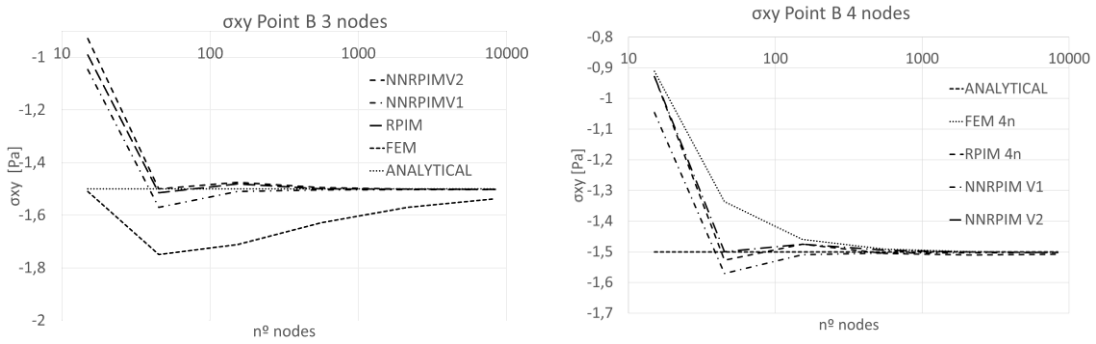

a) b)

Figure 29. a) $\sigma_{xy}(x)$ in triangular mesh; b) $\sigma_{xy}(x)$ in quadrangular mesh

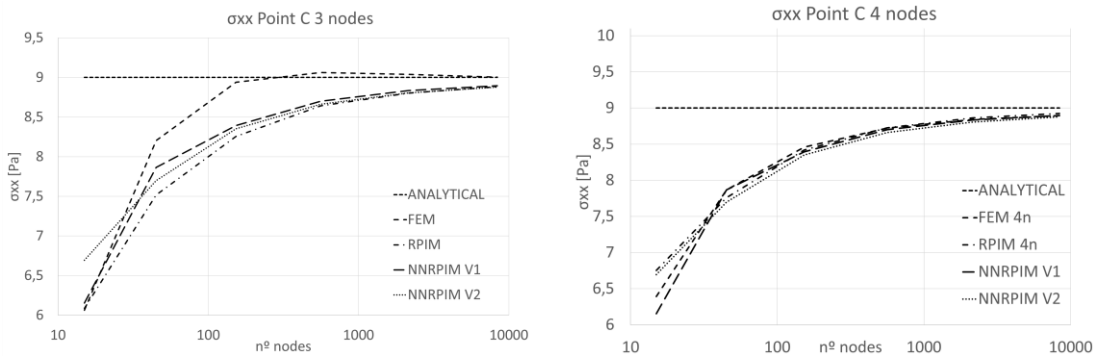

a) b)

Figure 30. a) $\sigma_{xx}(x)$ in triangular mesh; b) $\sigma_{xx}(x)$ in quadrangular mesh

The colour graphs can also be analysed to better understand the stress distribution across the beam. To ensure the accuracy of the results, the finest mesh structure, with 128×64 nodes, will be used. When examining Figure 31 it is notable that visual differences are almost insignificant, however NNRPIM is the method that generates the highest values when compared to the others. Regarding the shear stress graphs presented in Figure 32 it is evident that NNRPIM produces the lower values and FEM the highest.

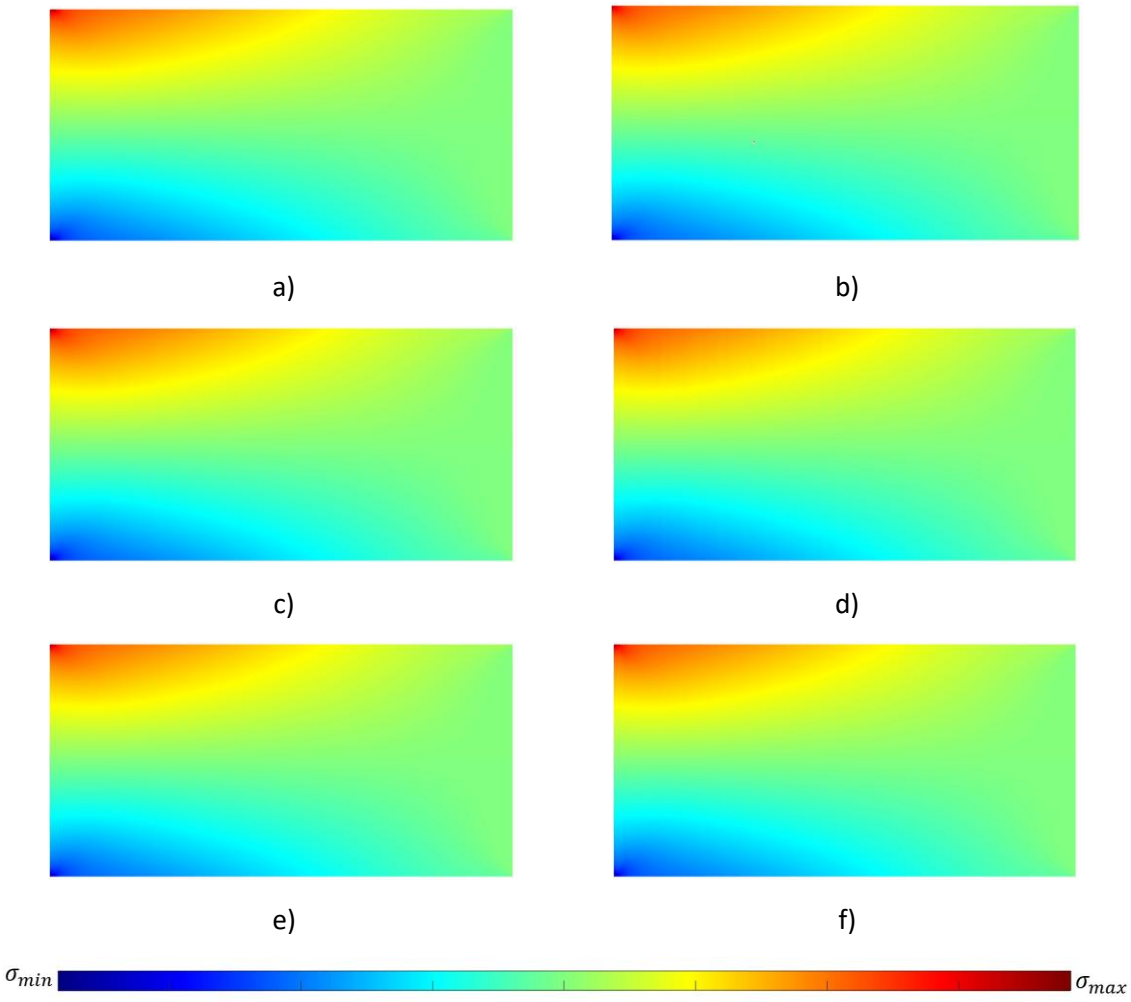

Figure 31. σ_{xx} colour map; a) FEM 3n ($\sigma_{\max} = 19.24$ MPa, $\sigma_{\min} = -19.24$ MPa); b) FEM 4n ($\sigma_{\max} = 19.42$ MPa, $\sigma_{\min} = -19.42$ MPa); c) RPIM 3n ($\sigma_{\max} = 19.07$ MPa, $\sigma_{\min} = -19.07$ MPa); d) RPIM 4n ($\sigma_{\max} = 19.36$ MPa, $\sigma_{\min} = -19.36$ MPa); e) NNRPIM V1 ($\sigma_{\max} = 19.59$ MPa, $\sigma_{\min} = -19.59$ MPa); f) NNRPIM V2 ($\sigma_{\max} = 19.39$ MPa, $\sigma_{\min} = -19.39$ MPa)

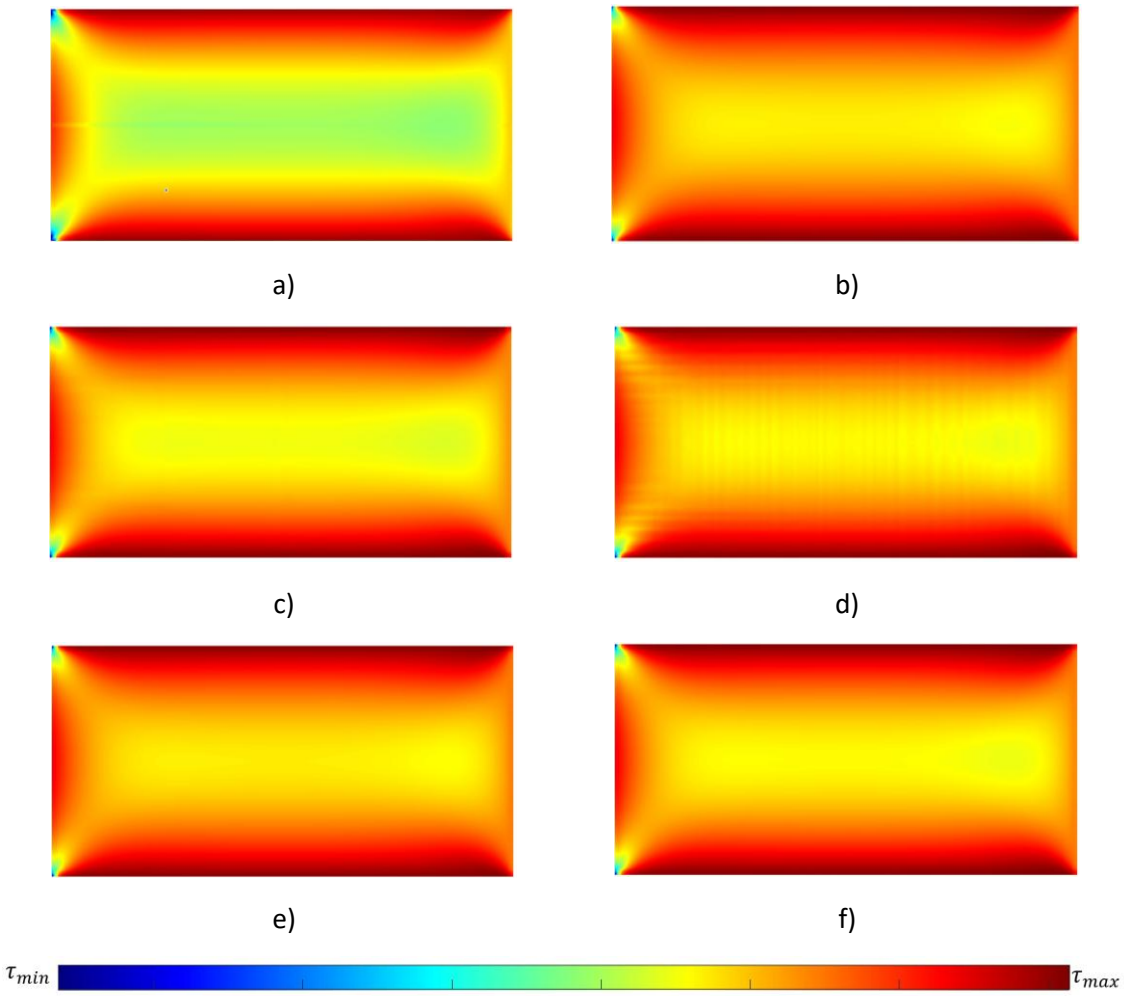

Figure 32. τ_{xy} colour map; a) FEM 3n ($\tau_{min} = -3.32\ Pa;\ \tau_{max} = 0\ Pa$); b) FEM 4n ($\tau_{min} = -4.12\ Pa;\ \tau_{max} = 0\ Pa$); c) RPIM 3n ($\tau_{min} = -3.85\ Pa;\ \tau_{max} = 0\ Pa$); d) RPIM 4n ($\tau_{min} = -4.01\ Pa;\ \tau_{max} = 0\ Pa$); e) NNRPIM V1 ($\tau_{min} = -4.22\ Pa;\ \tau_{max} = 0\ Pa$); f) NNRPIM V2 ($\tau_{min} = -3.99\ Pa;\ \tau_{max} = 0\ Pa$)

5.1.2. Cantilever beam 3D analysis

The 3D study followed the same procedure as the 2D analysis, with the addiction of thickness. To maintain a division of two along the z-axis while optimizing computational costs, the thickness was made variable. Therefore, natural boundary conditions will differ from those of the 2D analysis. Table 4 presents the dimensions used in the simulation and Figure 33 examples of the mesh divisions used.

Table 4. Divisions of the 3D analysis, thickness and number of nodes

Divisions	Thickness [m]	Nodes
$4 \times 2 \times 2$	1	45
$8 \times 4 \times 2$	0.5	135
$16 \times 8 \times 2$	0.25	459
$32 \times 16 \times 2$	0.125	1683

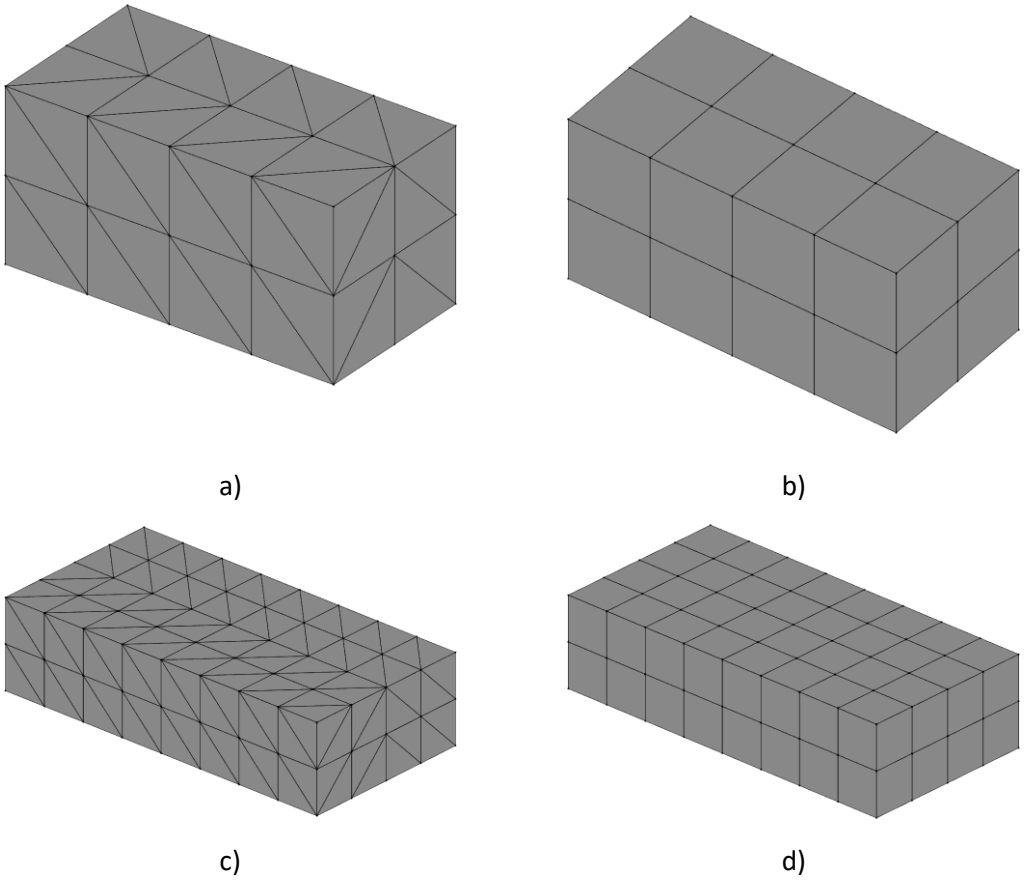

Figure 33. 3D Mesh divisions. a) tetrahedral $4 \times 2 \times 2$; b) hexahedral $4 \times 2 \times 2$; c) tetrahedral $8 \times 4 \times 2$; d) hexahedral $8 \times 4 \times 2$

For the FEM analysis, a classic formulation was applied using tetrahedral and hexahedral element meshes. In the RPIM method, influence domains consisted of 27 nodes, with the shape functions defined by parameters $c = 1.42$ and $p = 1.03$. Additionally, RPIM was implemented with both tetrahedral and hexahedral meshes. Lastly, for the NNRPIM method, investigations were conducted considering both first and second influence cells using parameters $c = 0.0001$ and $p = 0.9999$ for full integration.

The studied coordinates were identical to those used in the 2D analysis, with the addition of half the thickness to ensure the evaluation of the beam's midpoint in each case. In Figure 34, it's possible to observe the results obtained with the analysis of the 3D cantilever beam and understand how the convergence proceeds in every study. It is worth noting that some curves exhibit a slight misalignment with the analytical solution, resembling a lack of convergence. However, this discrepancy arises from the lower mesh density in the 3D analysis compared to the 2D analysis. When evaluating the vertical displacements, depicted in Figure 34, it is possible to exhibit that the FEM method with tetrahedral elements is the slowest to achieve convergence, when compared to the other methods for both tetrahedral and hexahedral elements. In Figure 35, where the shear stress is shown, FEM proves to displays the biggest discrepancy for both of the elements used when compared to meshless methods. The normal

stress curves presented in Figure 36, proves that the FEM analysis utilizing tetrahedral elements converges at a slower rate than the other methods.

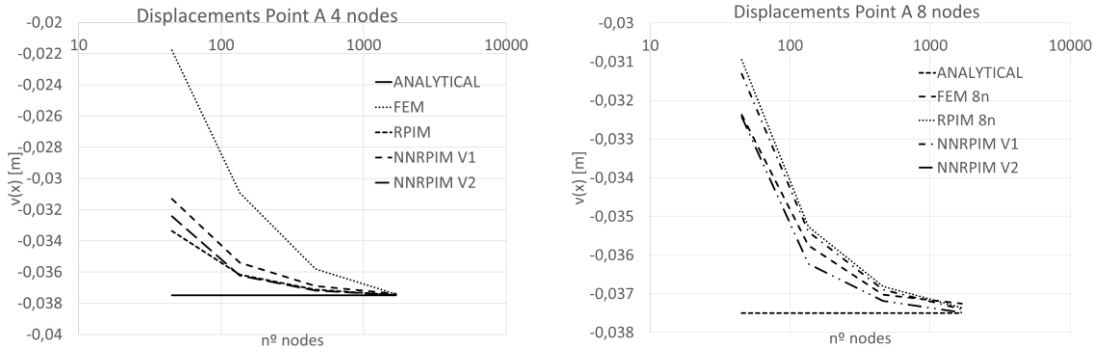

a) b)

Figure 34. a) Displacements in tetrahedral mesh; b) Displacements in hexahedral mesh

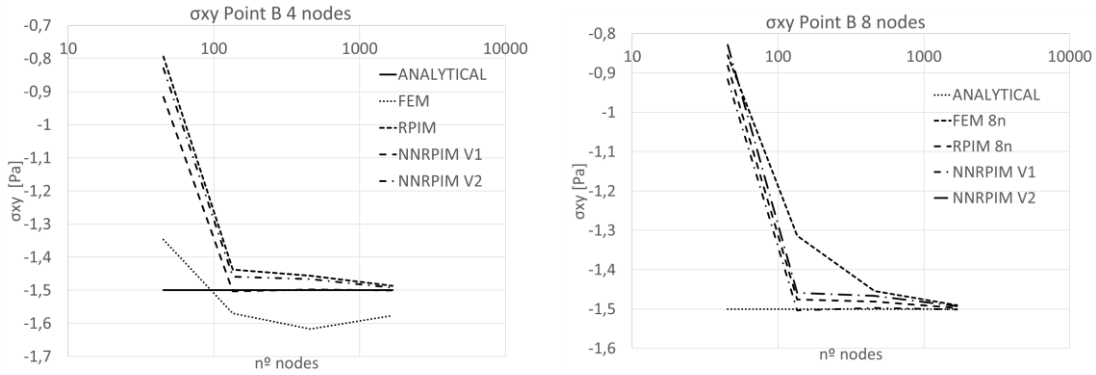

a) b)

Figure 35. a) $\sigma_{xy}(x)$ in tetrahedral mesh; b) $\sigma_{xy}(x)$ in hexahedral mesh

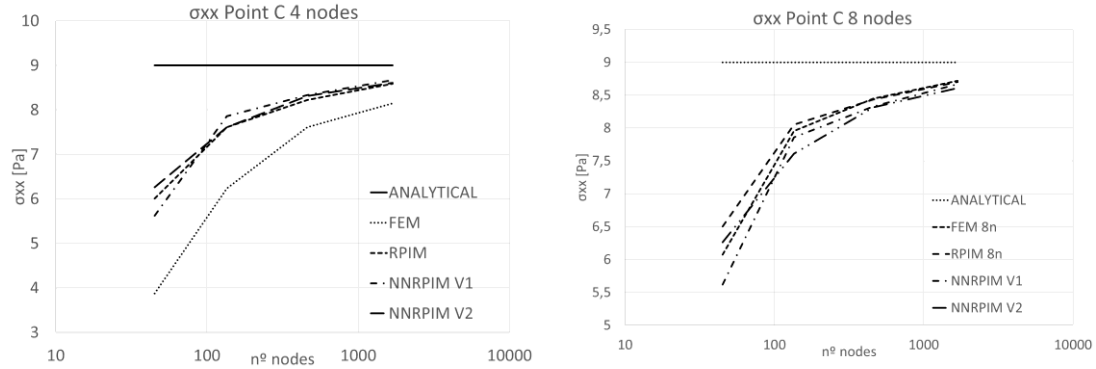

a) b)

Figure 36. $\sigma_{xx}(x)$ in tetrahedral mesh; b) $\sigma_{xx}(x)$ in hexahedral mesh

Following the same pattern as the 2D analysis, colour maps of the normal and shear stress are presented in Figure 37 and Figure 38 respectively. Analysing Figure 37 one observes that FEM analysis produce higher values when compared to the other methods, especially with hexahedral mesh elements. According to the shear stress analysis results (Figure 38), FEM exhibits the highest values. However, unlike the normal stress analysis, the tetrahedral mesh elements yield the highest values in this case.

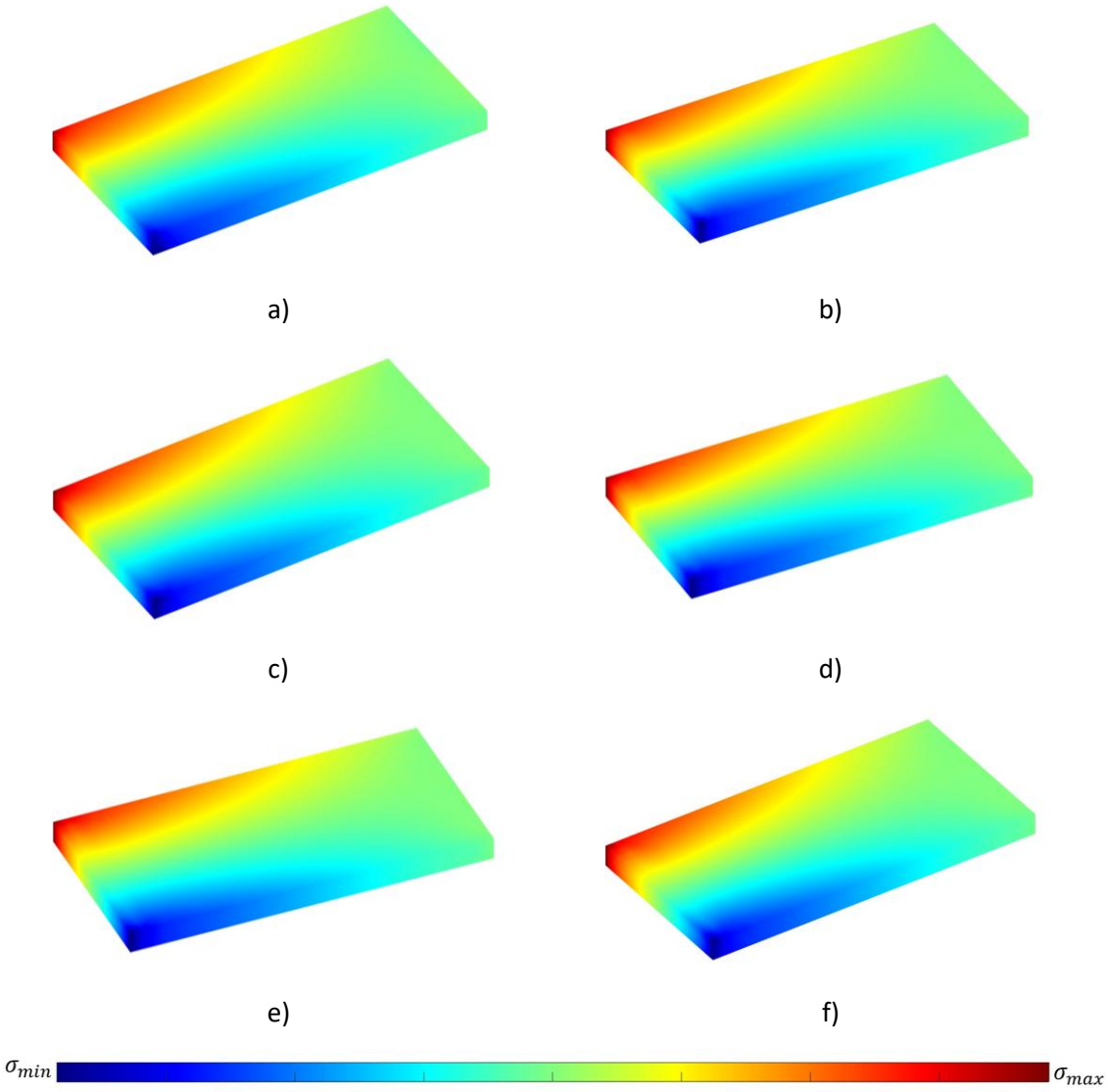

Figure 37. σ_{xx} colour map; a) FEM 3n ($\sigma_{\max} = 15.52$ MPa, $\sigma_{\min} = -15.52$ MPa); b) FEM 4n ($\sigma_{\max} = 15.72$ MPa, $\sigma_{\min} = -15.72$ MPa); c) RPIM 3n ($\sigma_{\max} = 14.82$ MPa, $\sigma_{\min} = -14.82$ MPa); d) RPIM 4n ($\sigma_{\max} = 15.04$ MPa, $\sigma_{\min} = -15.04$ MPa); e) NNRPIM V1 ($\sigma_{\max} = 15.30$ MPa, $\sigma_{\min} = -15.30$ MPa); f) NNRPIM V2 ($\sigma_{\max} = 15.22$ MPa, $\sigma_{\min} = -15.22$ MPa)

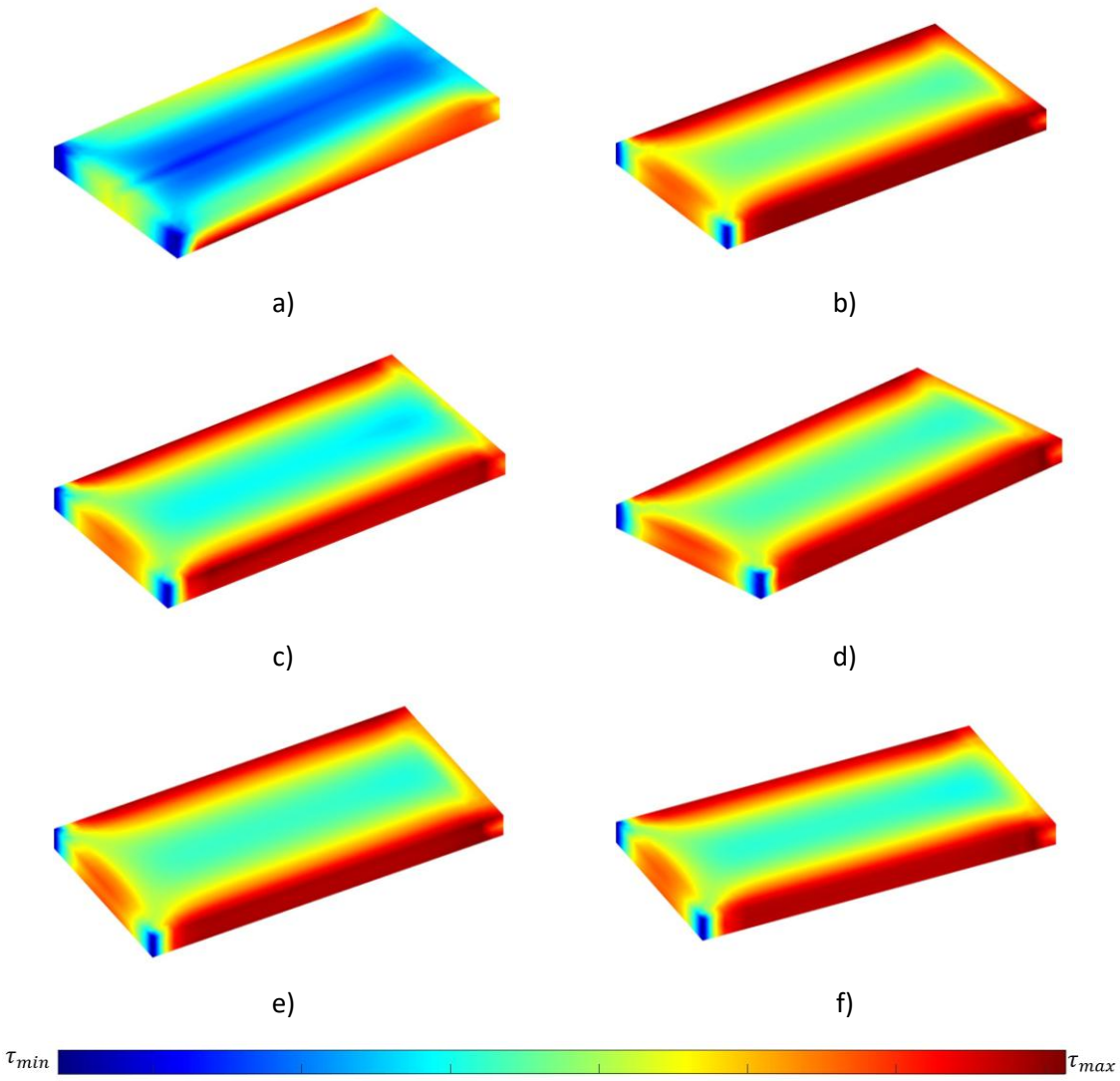

Figure 38. τ_{xy} colour map; a) FEM 3n ($\tau_{min} = -1.975\ Pa; \tau_{max} = 0\ Pa$); b) FEM 4n ($\tau_{min} = -2.77\ Pa; \tau_{max} = 0\ Pa$); c) RPIM 3n ($\tau_{min} = -2.44\ Pa; \tau_{max} = 0\ Pa$); d) RPIM 4n ($\tau_{min} = -2.72\ Pa; \tau_{max} = 0\ Pa$); e) NNRPIM V1 ($\tau_{min} = -2.67\ Pa; \tau_{max} = 0\ Pa$); f) NNRPIM V2 ($\tau_{min} = -2.56\ Pa; \tau_{max} = 0\ Pa$)

5.2. Structural optimization

To further validate the effectiveness of the methods employed throughout this thesis, an optimization study will be conducted. The study focuses on a 2D beam with dimensions of 2400 × 400 mm, as it is presented in Figure 39. To simplify the analysis and reduce computational time, only half of the beam will be modelled. As illustrated in Figure 40, the beam is restrained at its left end, preventing any movement in the *y* direction. At the right end, it is restrained in the *x* direction only, allowing for vertical displacement and rotation. Additionally, a vertical load of 20 kN is applied to the top surface of the beam. The material used for the beam is aluminium and the optimization study will be caried out using both the Bone Remodelling approach and the Bi-directional Evolutionary Structural Optimization (BESO) method.

Initially, it is necessary to analyse the beam for each method, as it was done for the Cantilever beam in chapter 5.1. The FEM method follows a classic approach. As for the RPIM method the influence domain exhibits 16 nodes with the following parameters: $c = 1.42$ and $p = 1.03$. During the analysis the RPI followed a linear polynomial basis and a $2 \times 2 \times 2$ gauss integration. Regarding the NNRPIM method, it was applied considering both first and second-degree neighbours. Full integration was also employed for the parameters $c = 0.0001$ and $p = 0.9999$. In Figure 41, a representation of the expected benchmark results is presented.

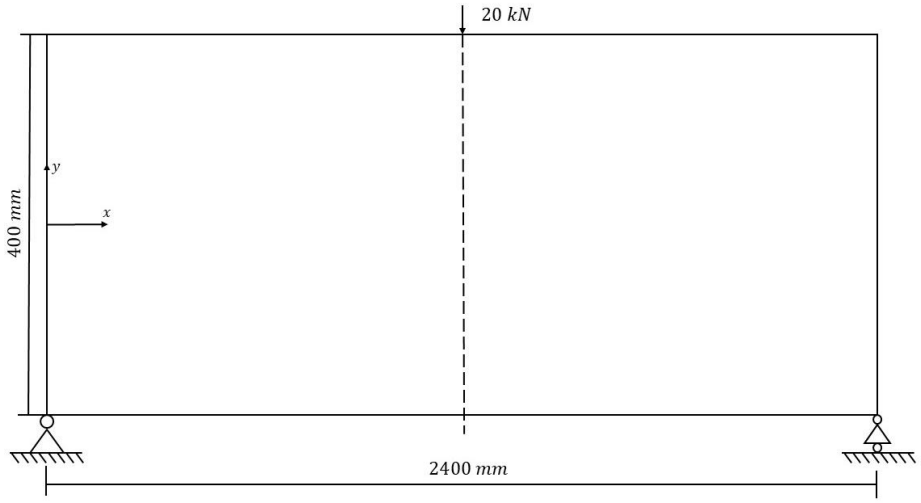

Figure 39. Structural optimization study full beam

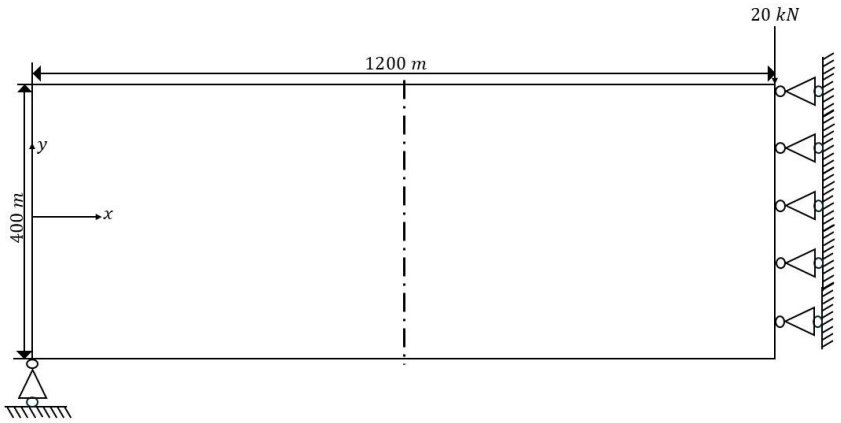

Figure 40. Structural optimization study beam

Figure 41. Benchmark beam results [47]

5.2.1. Bone remodelling

In order to optimize the structure of beam with the Bone remodelling method, it is necessary to define its remodelling parameters. Since the method used is the Bone remodelling method, the maximum material density used is $2.1\ kg/m^3$ and the simulation is required to stop at an average density of $0.2\ kg/m^3$. To understand how density decrease ratios (β) influence the results of the simulations, values of 0.01; 0.02 and 0.05 will be used. Important to note that the density increase ratio will always be null. The number of times each point can undergo remodelling will be determined by selecting a value within the range of 1 to 5. To define the optimal beam structure, an average density of 0.9 (around 45% of the initial value) is imposed. Accordingly, the iteration selected should be the one whose resulting density most closely approximates the target value [47].

The results for the simply supported beam are presented from Figure 42 to Figure 45. As observed, all outcomes closely align with the benchmark solution, demonstrating the effectiveness of the methods employed in analysing the beam's behaviour. Furthermore, when examining the data, it is evident that the Decrease Ratio (DR) of $\beta = 0.01$ yields the highest computational time when compared to the other DR values. When analysing each design produced throughout the optimization process, it is evident that by employing a higher DR the computational time is reduced, due to the fact that by iteration, more material is being removed. It is important to also to note that a higher DR generates enhanced results.

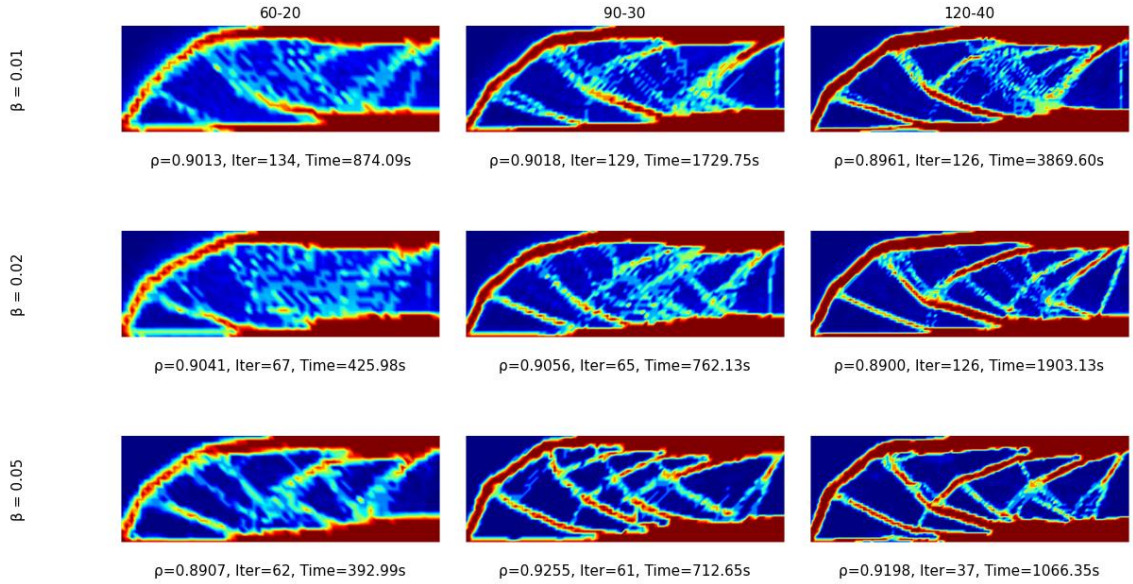

Figure 42. Bone remodelling FEM analysis

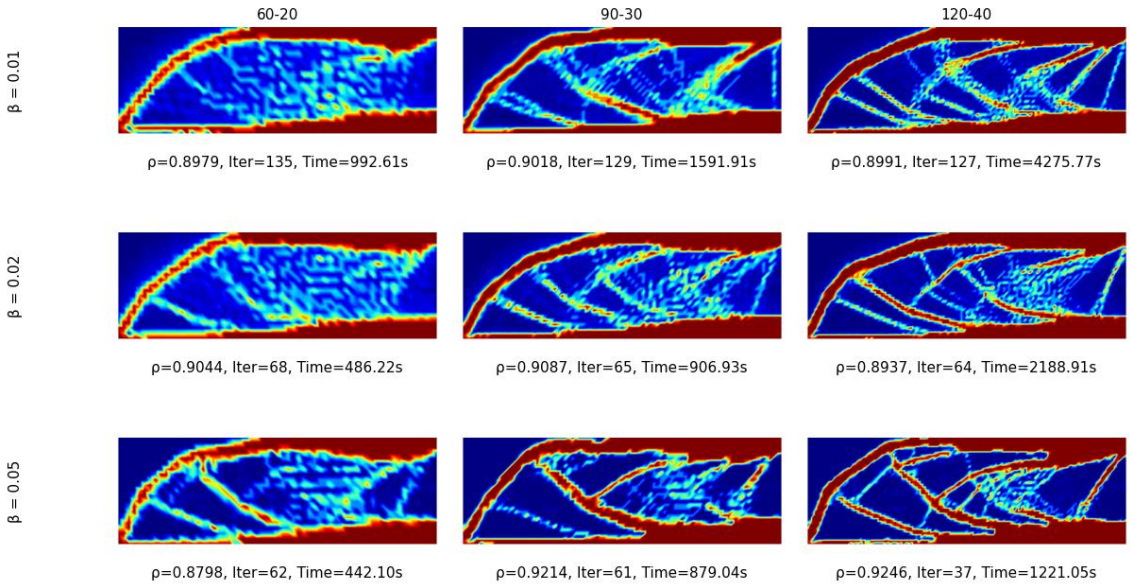

Figure 43. Bone remodelling RPIM analysis

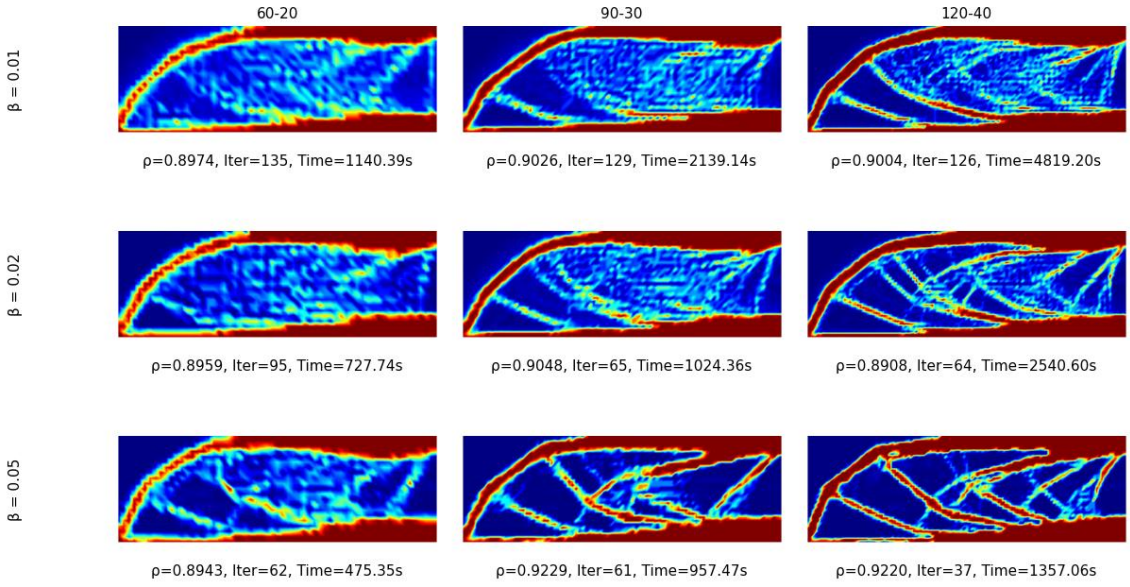

Figure 44. Bone remodelling NNRPIM V1 analysis

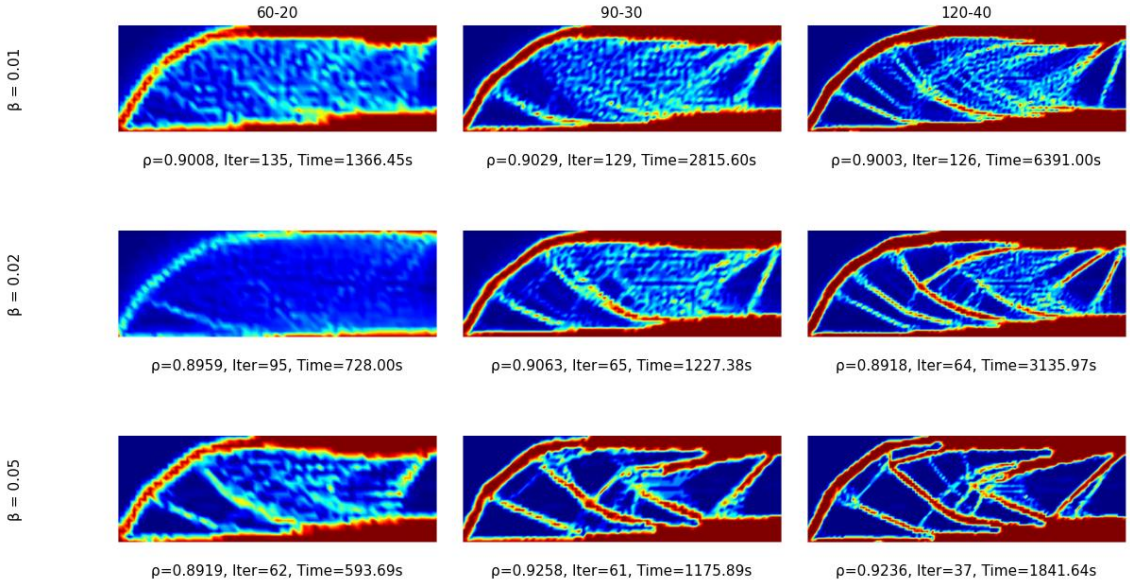

Figure 45. Bone remodelling NNRPIM V2 analysis

A comparison can now be made between the results obtained for the simply supported beam and those of the fully restrained configuration at the corresponding coordinate. The solutions exhibit notably different beam configurations, due to the distinct loading conditions and internal force distributions. The density plots generated using the methods previously described are presented from Figure 46 to Figure 49, and as it is possible to observe the results were in line with expectations, since by introducing a reaction in the horizontal direction, the presence of the horizontal bar was no longer necessary. Therefore, the obtained results matched the predicted behaviour.

In conclusion, it is notable that with the BONE remodelling method for the simply supported structure, every method studied generated results that closely align with the benchmark example. It is also important to state that using a higher DR, tends to improve the results and reduce the computational time due to the fact that for each iteration, a much superior mass quantity is being removed. The results show that the higher the number of mesh divisions, the better the results, which was expected.

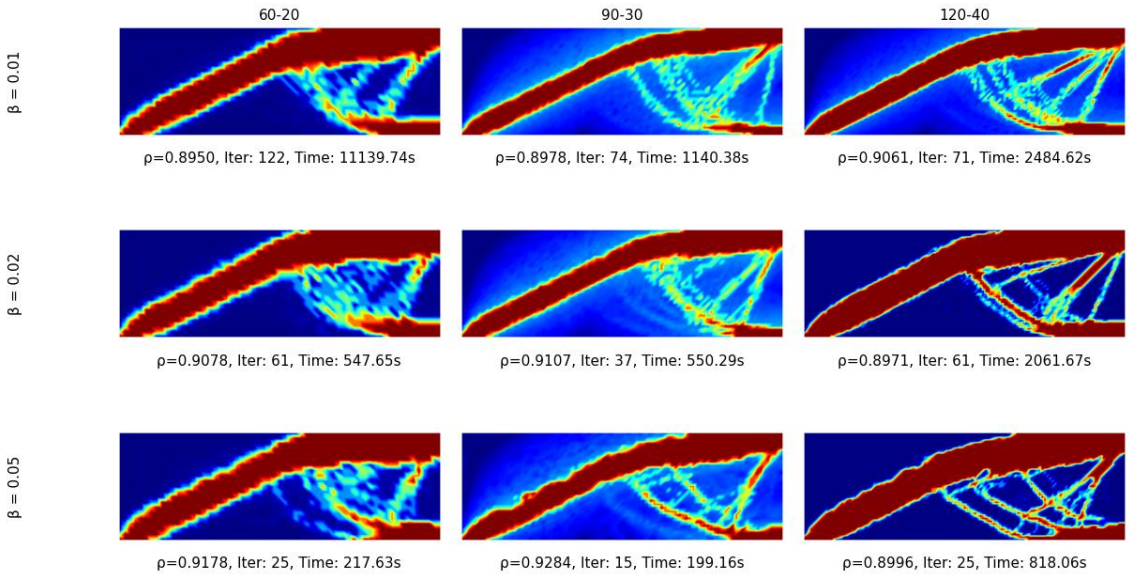

Figure 46. Bone remodelling for FEM analysis

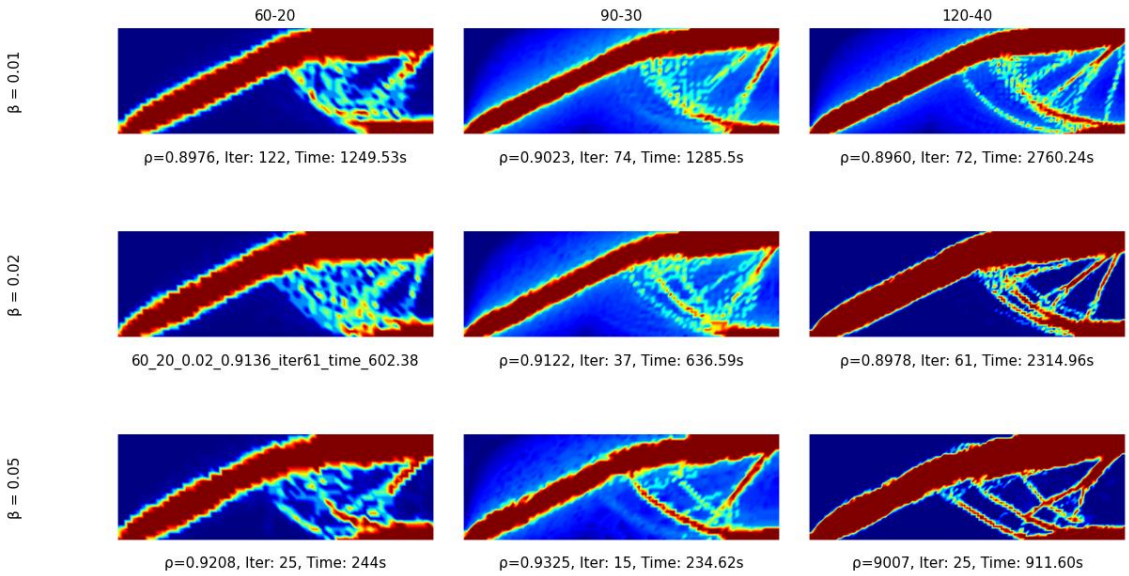

Figure 47. Bone remodelling for RPIM analysis

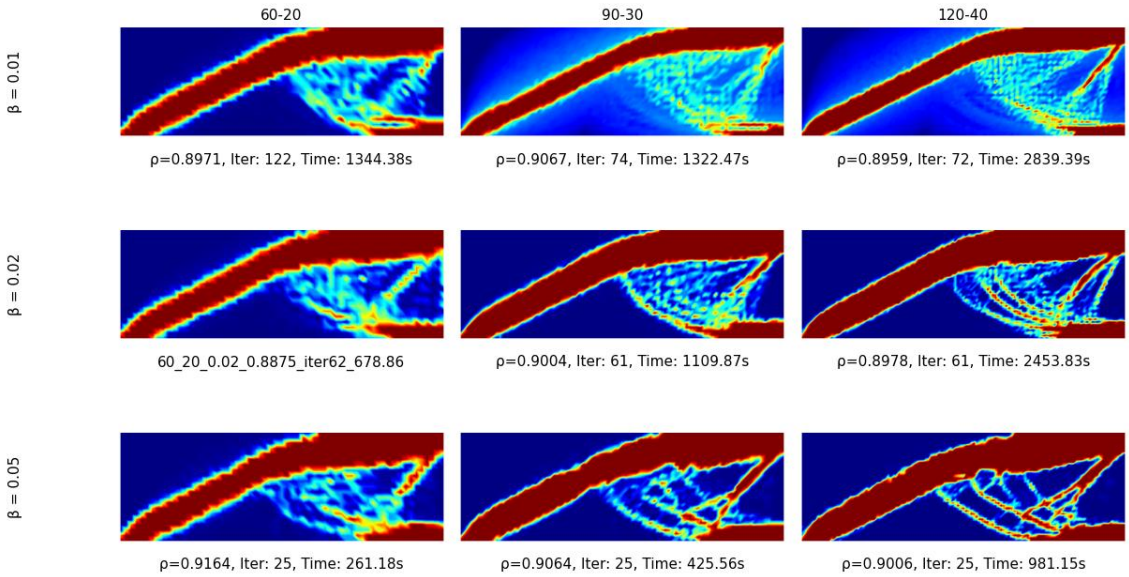

Figure 48. Bone remodelling for NNRPIM V1 analysis

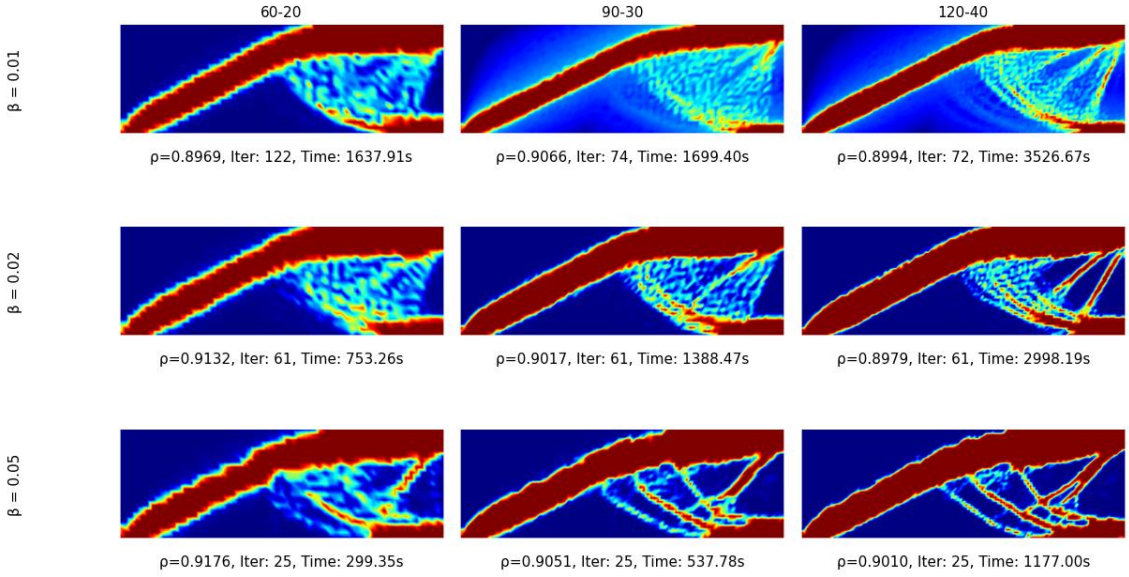

Figure 49. Bone remodelling for NNRPIM V2 analysis

5.2.2. BESO

Contrary to the Bone remodelling method, BESO has a maximum material density of $1\ kg/m^3$ and the simulation is required to stop at an average density of $0.2\ kg/m^3$. While all simulation parameters are maintained equivalent to those utilized in the bone remodelling framework, the inherently different nature of BESO leads to a variable number of allowable remodelling events per point, unconstrained by a predefined range. To define the optimal beam structure, an average density of $0.45\ kg/m^3$ (45% of the initial value) is imposed. Accordingly, the iteration yielding an average density most closely aligned with this target is selected as the optimal solution.

The results for the simply supported beam are presented from Figure 50 to Figure 53. As observed from Figure 50 to Figure 53, both NNRPIM analyses present the best results, being the ones which most closely align with the benchmark example and the ones that achieved the target density. A decrease ratio of 0.01 proved to produce results with the highest deviance, when compared to 0.02 and 0.05. At a first instance, it is possible to observe that the RPIM method produces the worst results, being the ones with a higher medium density value as well as the least improved structure. When analysing Figure 51, it is clear that for the RPIM method, the only structure that was approved is the one using the densest mesh (120x40) with a decrease ratio of 0.05. This is the only case that closely matches the benchmark solution. The FEM method gives better results than RPIM, but it still does not perform as well as the meshless methods. This is mainly because of how the FEM and RPIM methods are programmed, especially the use of a kurtosis ratio. During the remodelling process, the kurtosis is calculated at each iteration. If the value falls outside a predefined range, the remodelling starts over. Also, the number of iterations plays an important role, depending on the decrease ratio used. In all studies, the DR was set to 10, meaning that reinforcement happens every 10 iterations. Because of this, both FEM and RPIM might not have enough time between reinforcements to fully optimize the beam, since the cycle is too short for significant changes to happen.

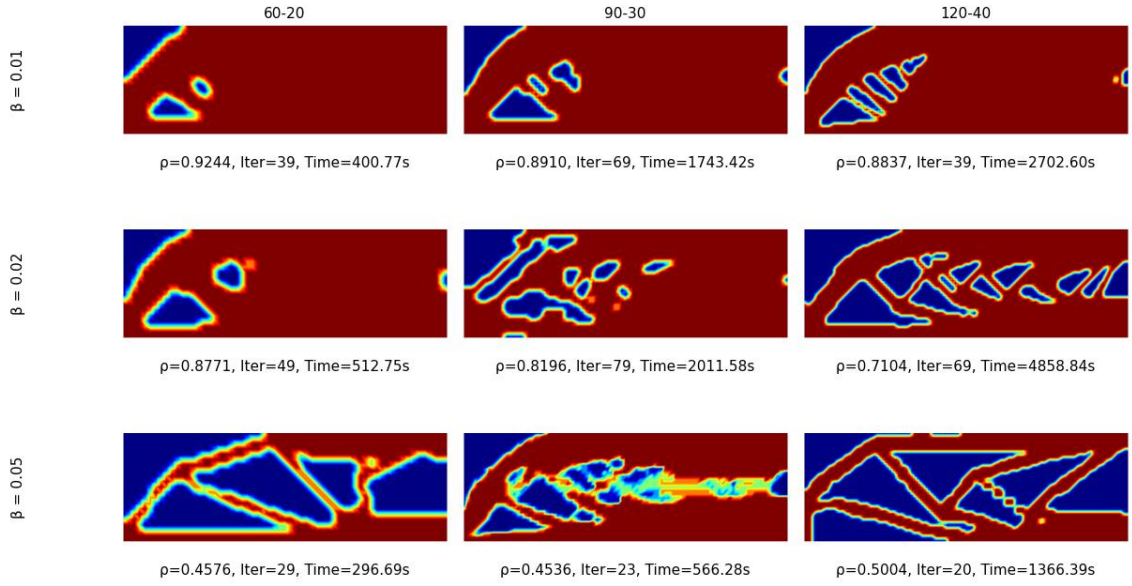

Figure 50. Simply supported beam FEM BESO analysis

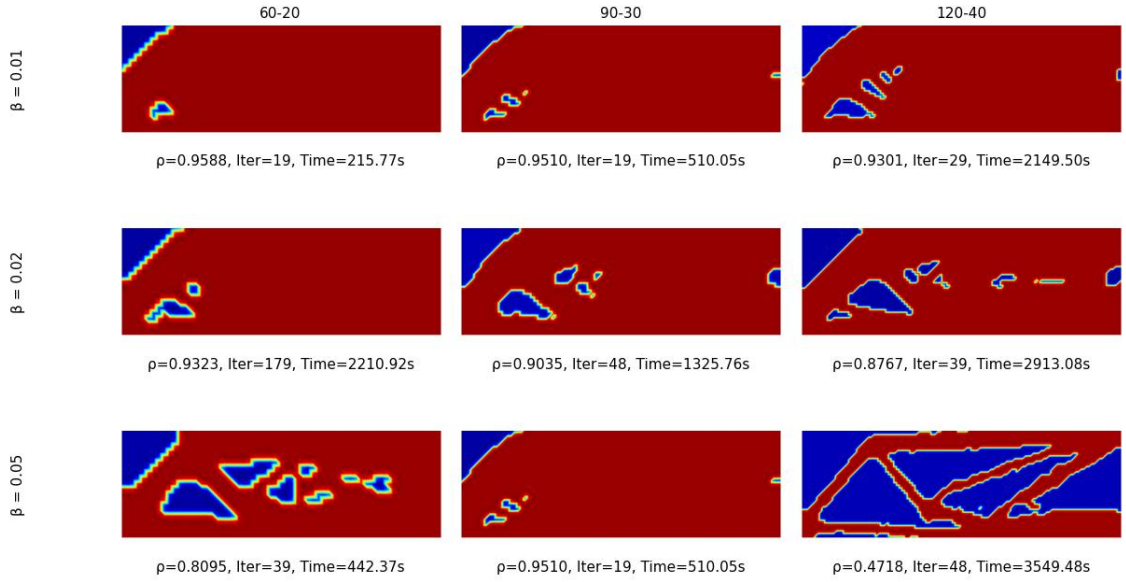

Figure 51. Simply supported beam RPIM BESO analysis

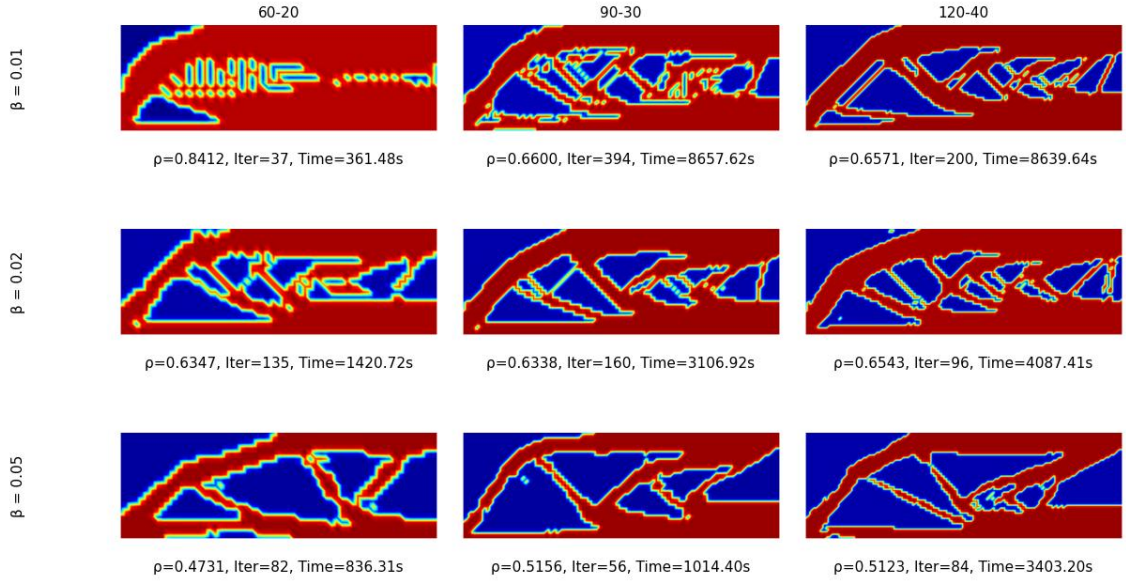

Figure 52. Simply supported beam NNRPIM V1 BESO analysis

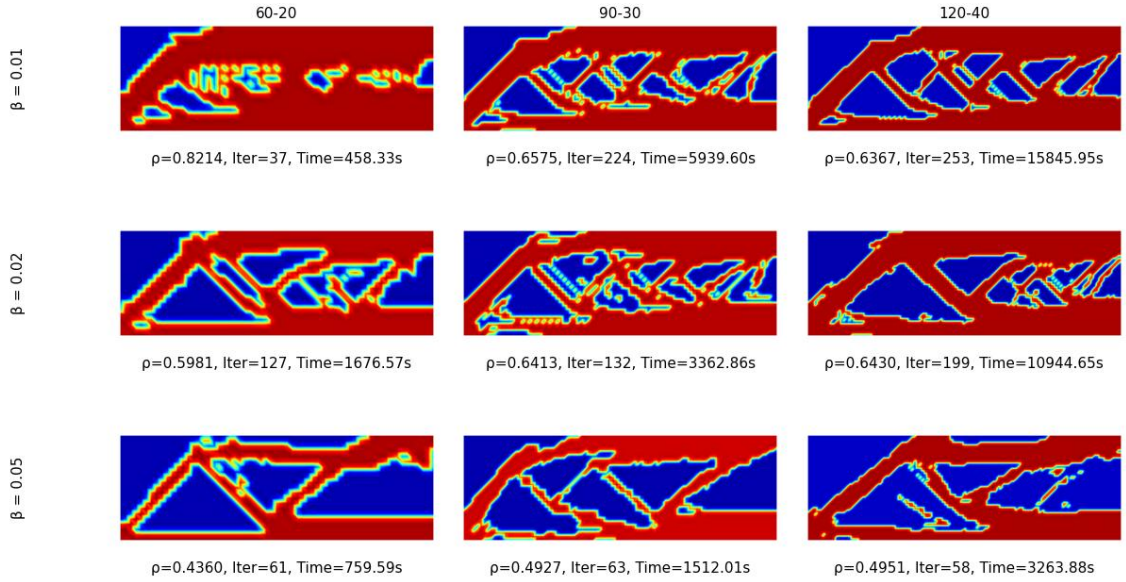

Figure 53. Simply supported beam NNRPIM V2 BESO analysis

Such results can now be compared to the fully restrained beam, presented across Figure 54 to Figure 57. As it is possible to observe in Figure 56 and Figure 57, once again, the meshless methods demonstrate the lowest deviation in results, as they not only align more closely with the target density but also lead to better optimized structures. In the case of the FEM analysis, the results obtained for the fully restrained beam were more accurate and resulted in a more efficient structure compared to the simply supported beam. Regarding the RPIM methods, although their performance was better than that of the simply supported beam, they generally produced the least accurate results among all the methods analysed.

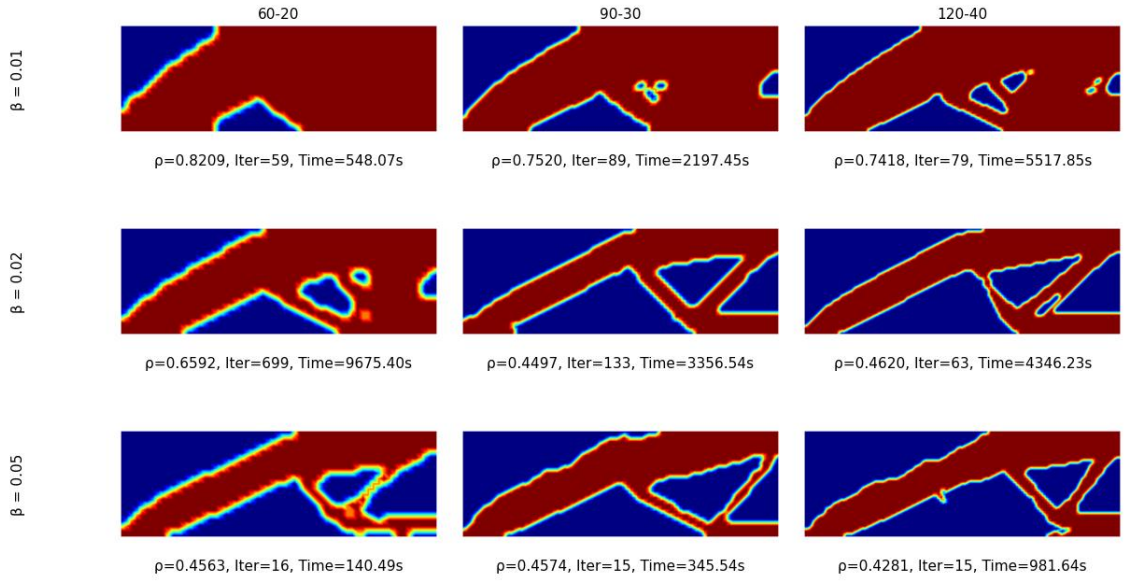

Figure 54. Fully supported beam FEM BESO analysis

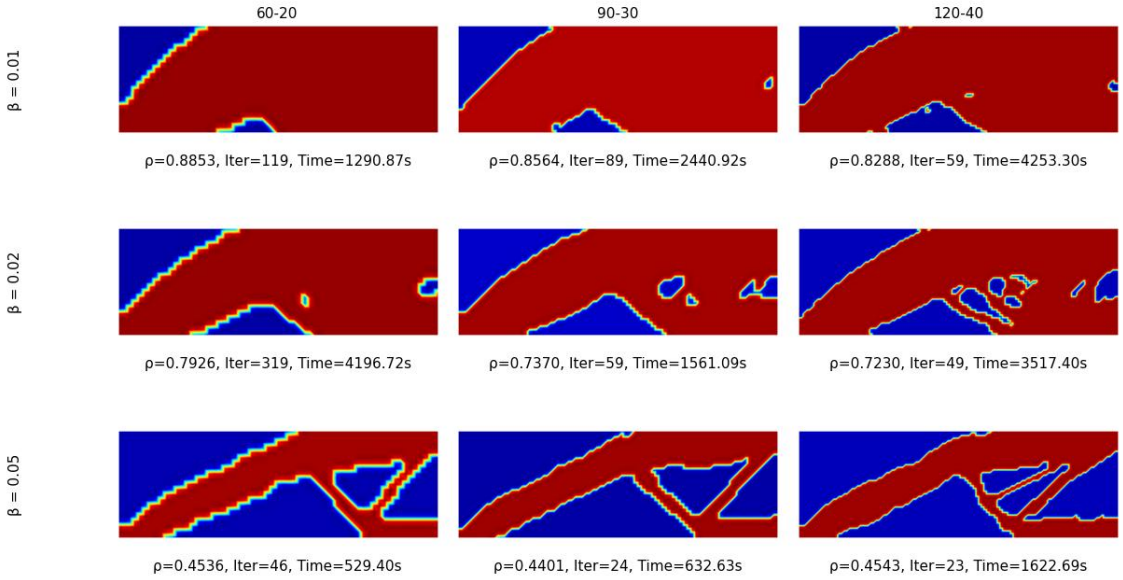

Figure 55. Fully supported beam RPIM BESO analysis

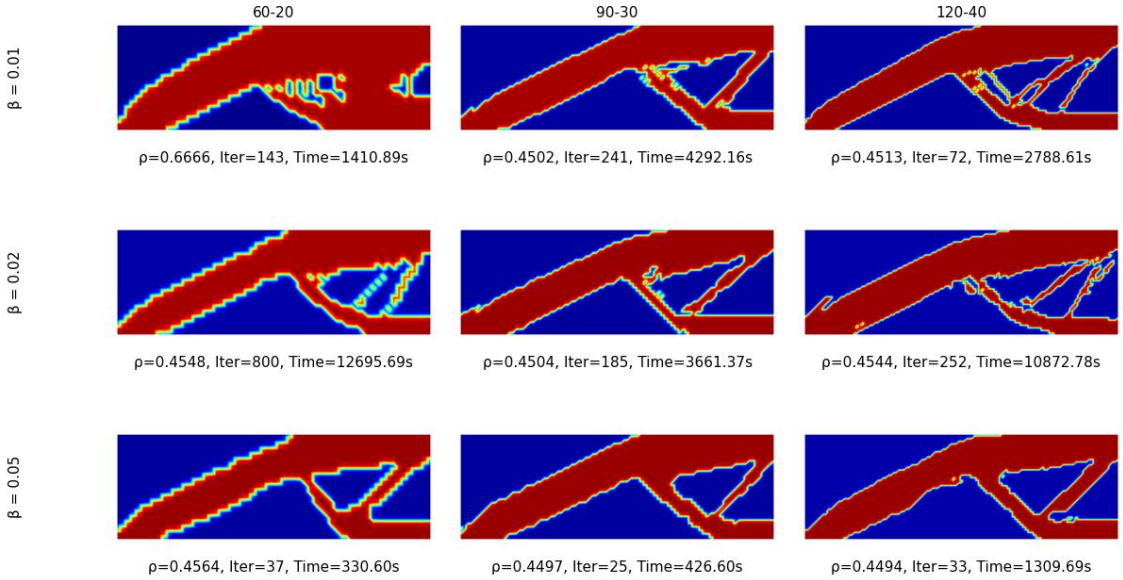

Figure 56. Fully supported beam NNRPIM V1 BESO analysis

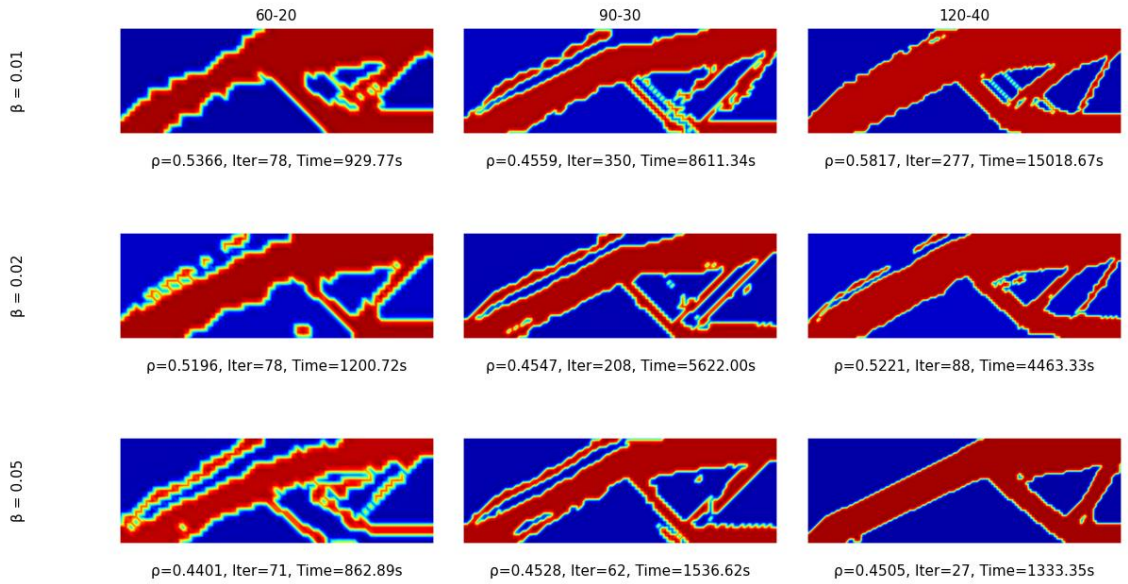

Figure 57. Fully supported beam NNRPIM V2 BESO analysis

Since the results obtained for some studies are not the excepted, improvements and changes on the coding behind the FEM and RPIM methods, were made. Initially, the number of iterations needed in order to reinforce the beam was increased to 30, in order to promote a much higher optimization interval. The first test was performed with a mesh of 90x30 with a decrease ratio of 0.02, with FEM. The results obtained can be observed in Figure 58. With an interval of 30 iterations before remodelling and reinforcing, it is notable that the optimized structure becomes much more align with the benchmark result presented in Figure 41 and has a higher similarity with the one produced by the meshless methods. As for the RPIM method, the same mesh with the same DR was chosen. According to Figure 59b), by utilizing a 30 iteration interval, it is possible to create an optimized structure closer to the targeted one, however it shows a little deviance when compared to other methods. A possible way to increase the efficiency of the RPIM method would be to further extend the iteration cycle, however, this could also be disadvantageous due to the fact that it would reduce the frequency of point correction. As a result, even if a structure similar to the benchmark were achieved, it might contain more internal errors.

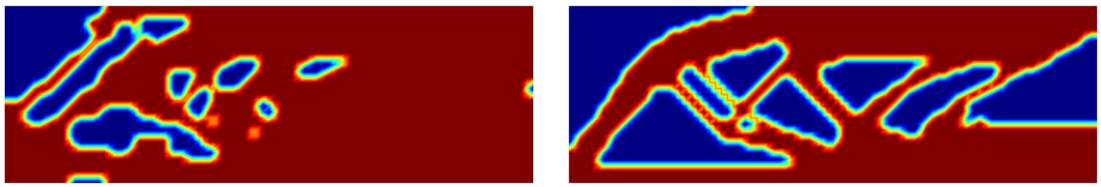

a) b)

Figure 58. a) FEM (90x30;0.02) study with a 10 iteration interval; b) FEM (90x30;0.02) study with a 30 iteration interval

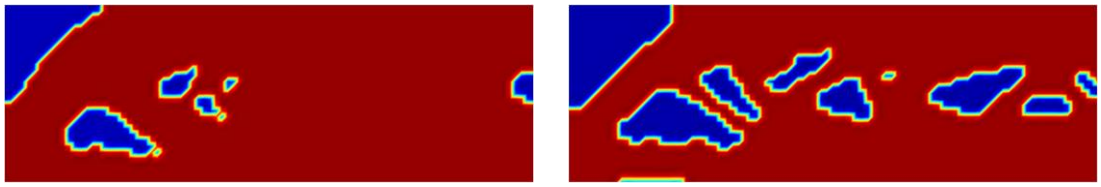

a) b)

Figure 59. a) RPIM (90x30;0.02) study with a 10 iteration interval; b) RPIM (90x30;0.02) study with a 30 iteration interval

5.3. Elastostatic studies

With the structural optimization process completed, the most optimal designs obtained from each method were selected for further analysis, using parameters consistent with those presented in chapter 5.1.1. Specifically, the selected configurations were FEM with a mesh of 60x20, RPIM with a mesh of 120x40, NNRPIM V1 with a mesh of 60x20 and NNRPIM V2 with a mesh of 60x20. It is important to note that every design selected was design with the BESO optimization procedure and possessed a decrease ratio of 0.05. Although the meshless methods demonstrated superior performance in generating more efficient structures, all optimization approaches were included in evaluation to ensure a comprehensive comparison. The analyses performed focuses on the Von Misses stress. The analysis made of the simply supported beams are presented from Figure 60 to Figure 66. As it possible to observe, the Von Mises stress is of a similar scale throughout all structures, however the structures obtained with the FEM method (Figure 60) exhibit the lower overall values despite the study technique used, particularly when analysed with the NNRPIM V2 method. Across all methods, meshless approaches consistently produce lower von Mises stress values, with the NNRPIM V2 method yielding the lowest stress values among them. On the contrary, the RPIM method produces the highest Von Misses stress values, indicating to be the least suitable method for the analysis. Due to its effective performance in elastostatic analysis and the encouraging results from previous optimization studies, NNRPIM V2 will be used for the upcoming optimization of the rover's suspension system.

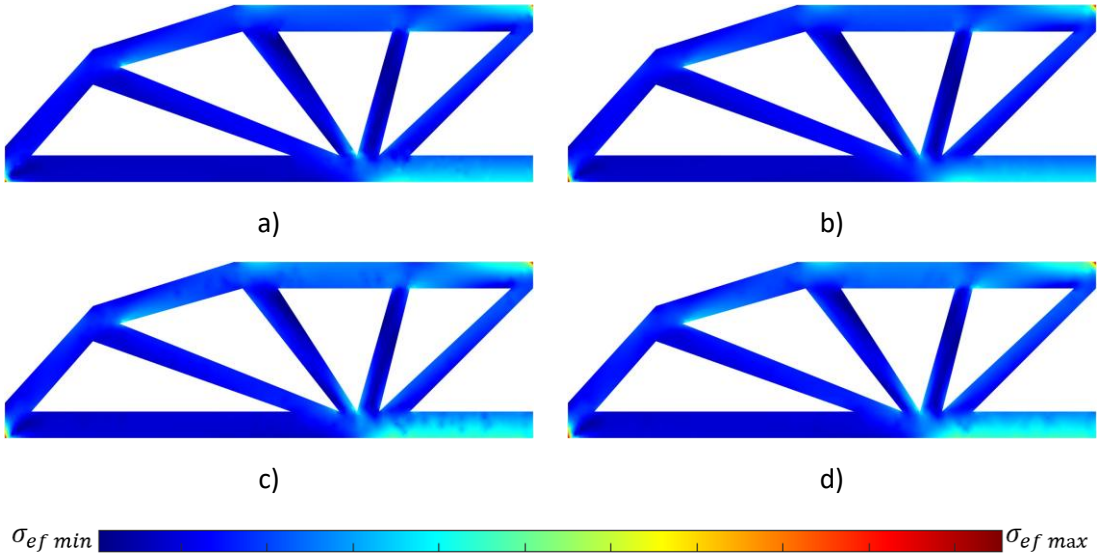

Figure 60. FEM Simply supported beam; a) FEM ($\sigma_{ef\ max} = 3.92\ \times 10^6\ Pa;\ \sigma_{ef\ min} = 2.09\ \times 10^4\ Pa$); b) RPIM ($\sigma_{ef\ max} = 3.97\ \times 10^6\ Pa;\ \sigma_{ef\ min} =\ 1.40\ \times 10^4\ Pa$); c) NNRPIM V1 ($\sigma_{ef\ max} = 3.43\ \times 10^6\ Pa;\ \sigma_{ef\ min} = 1.48\ \times 10^4\ Pa$); d) NNRPIM V2 ($\sigma_{ef\ max} = 3.35\ \times 10^6\ Pa;\ \sigma_{ef\ min} = 1.42\ \times 10^4\ Pa$)

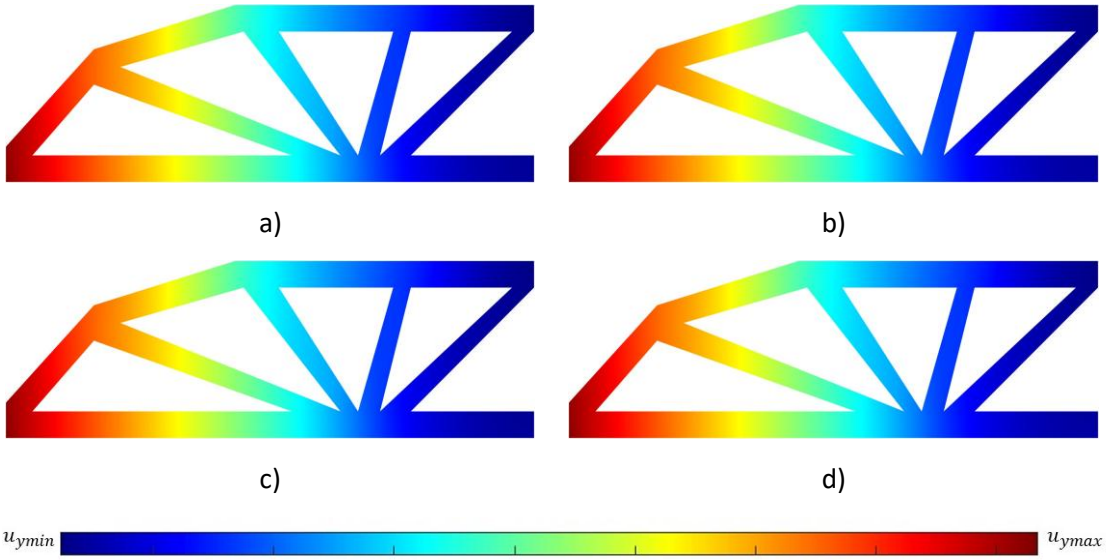

Figure 61. FEM Simply supported beam. a) FEM ($u_{max} = 0;\ u_{min} = -6.78 \times 10^{-5}\ m$); b) RPIM ($u_{max} = 0;\ u_{min} = -6.82 \times 10^{-5}\ m$); c) NNRPIM V1 ($u_{max} = 0;\ u_{min} = -6.81 \times 10^{-5}\ m$); d) NNRPIM V2 ($u_{max} = 0;\ u_{min} = -6.77 \times 10^{-5}\ m$)

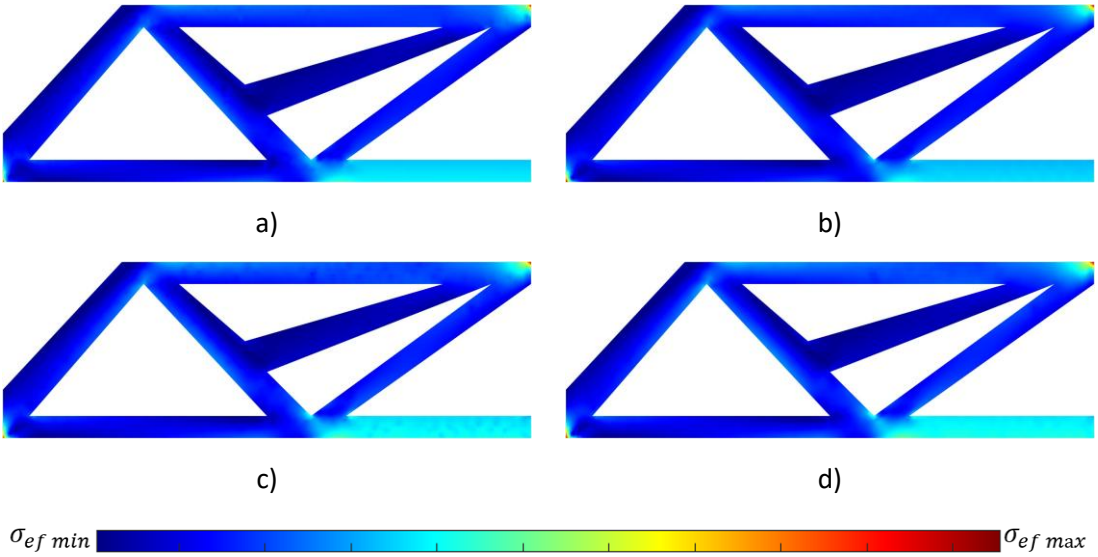

Figure 62. RPIM Simply supported beam; a) FEM ($\sigma_{ef\ max} = 3.89\ \times 10^{6}\ Pa;\ \sigma_{ef\ min} = 8.63\ \times 10^{3}\ Pa$); b) RPIM ($\sigma_{ef\ max} = 4.12\ \times 10^{6}\ Pa;\ \sigma_{ef\ min} = 7.00\ \times 10^{3}\ Pa$); c) NNRPIM V1 ($\sigma_{ef\ max} = 3.67\ \times 10^{6}\ Pa;\ \sigma_{ef\ min} = 9.84\ \times 10^{3}\ Pa$); d) NNRPIM V2 ($\sigma_{ef\ max} = 3.55\ \times 10^{6}\ Pa;\ \sigma_{ef\ min} = 1.05\ \times 10^{4}\ Pa$)

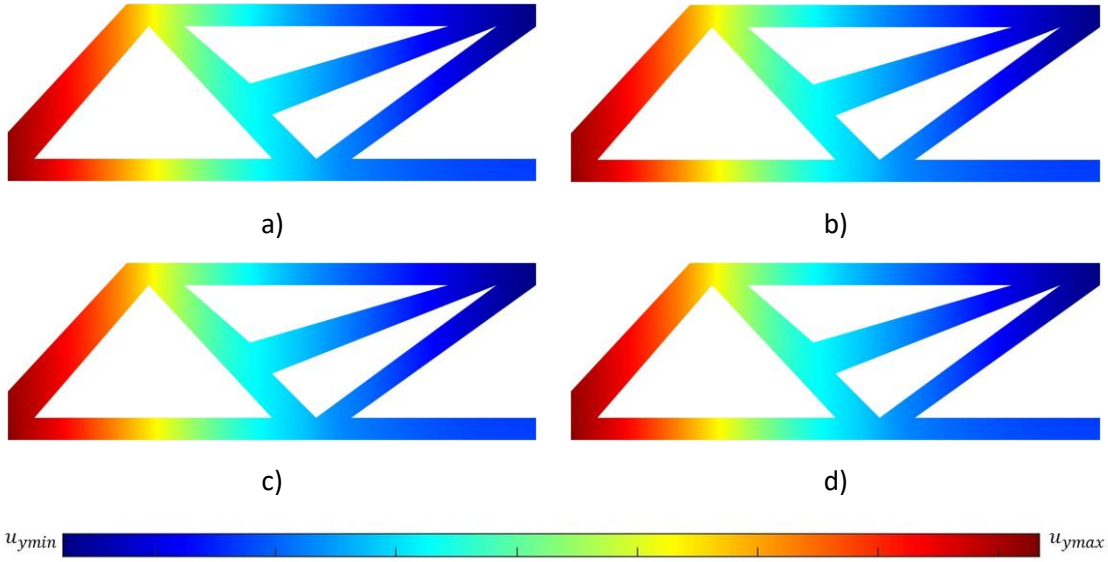

Figure 63. RPIM Simply supported beam. a) FEM ($u_{max} = 0;\ u_{min} = -7.19 \times 10^{-5}\ m$); b) RPIM ($u_{max} = 0;\ u_{min} = -7.24 \times 10^{-5}\ m$); c) NNRPIM V1 ($u_{max} = 0;\ u_{min} = -7.23 \times 10^{-5}\ m$); d) NNRPIM V2 ($u_{max} = 0;\ u_{min} = -7.20 \times 10^{-5}\ m$)

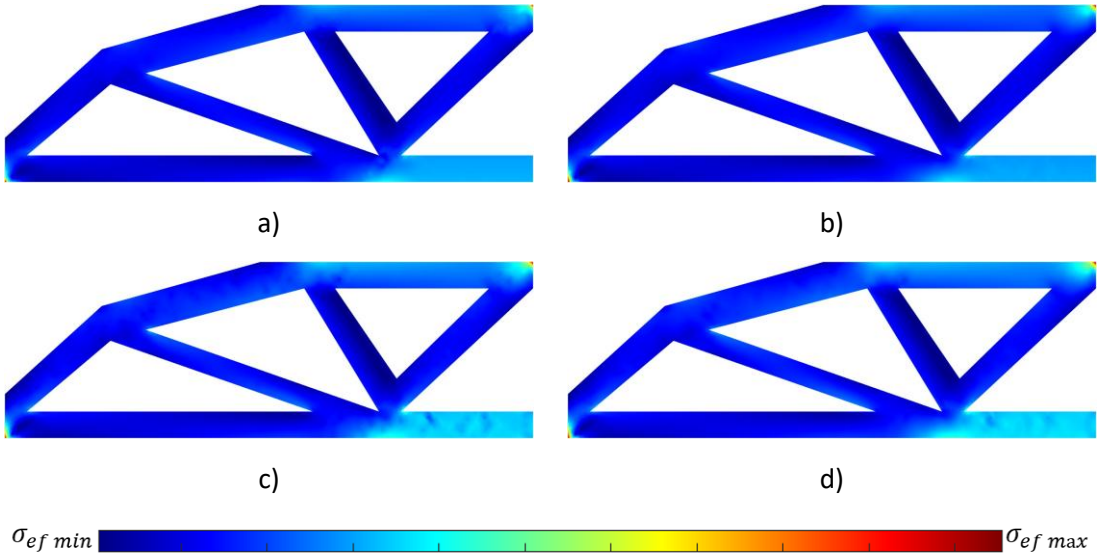

Figure 64. NNRPIM V1 Simply supported beam; a) FEM ($\sigma_{ef\ max} = 3.91\ \times 10^6\ Pa;\ \sigma_{ef\ min} = 1.12\ \times 10^4\ Pa$); b) RPIM ($\sigma_{ef\ max} = 4.00\ \times 10^6\ Pa;\ \sigma_{ef\ min} = 1.18\ \times 10^4\ Pa$); c) NNRPIM V1 ($\sigma_{ef\ max} = 3.53\ \times 10^6\ Pa;\ \sigma_{ef\ min} = 9.51\ \times 10^3\ Pa$); d) NNRPIM V2 ($\sigma_{ef\ max} = 3.42\ \times 10^6\ Pa;\ \sigma_{ef\ min} = 7.87\ \times 10^3\ Pa$)

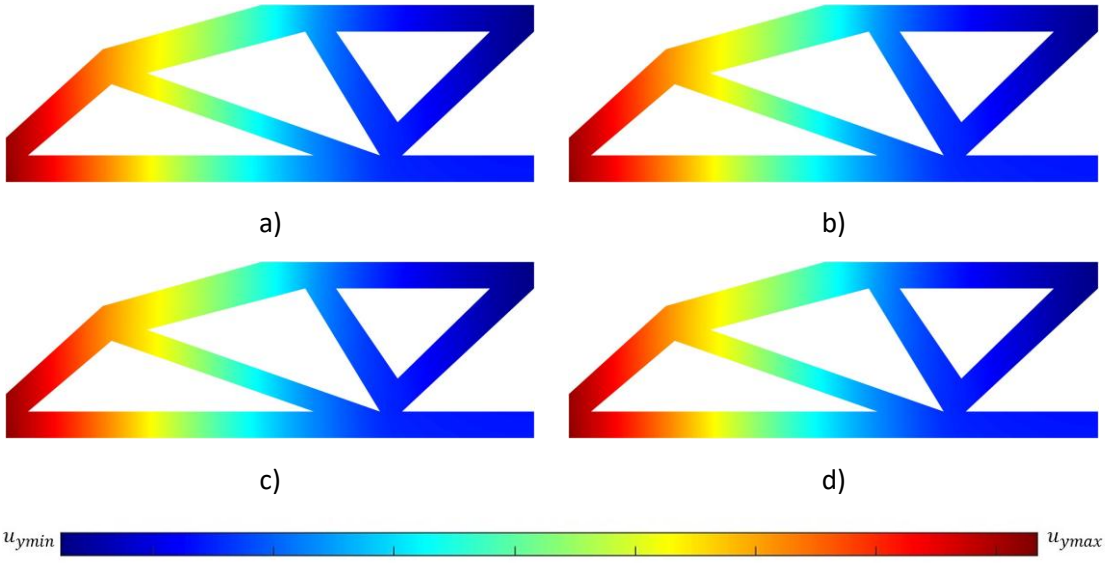

Figure 65. NNRPIM V1 Simply supported beam. a) FEM ($u_{max} = 0;\ u_{min} = -6.38 \times 10^{-5}\ m$); b) RPIM ($u_{max} = 0;\ u_{min} = -6.42 \times 10^{-5}\ m$); c) NNRPIM V1 ($u_{max} = 0;\ u_{min} = -6.42 \times 10^{-5}\ m$); d) NNRPIM V2 ($u_{max} = 0;\ u_{min} = -6.39 \times 10^{-5}\ m$)

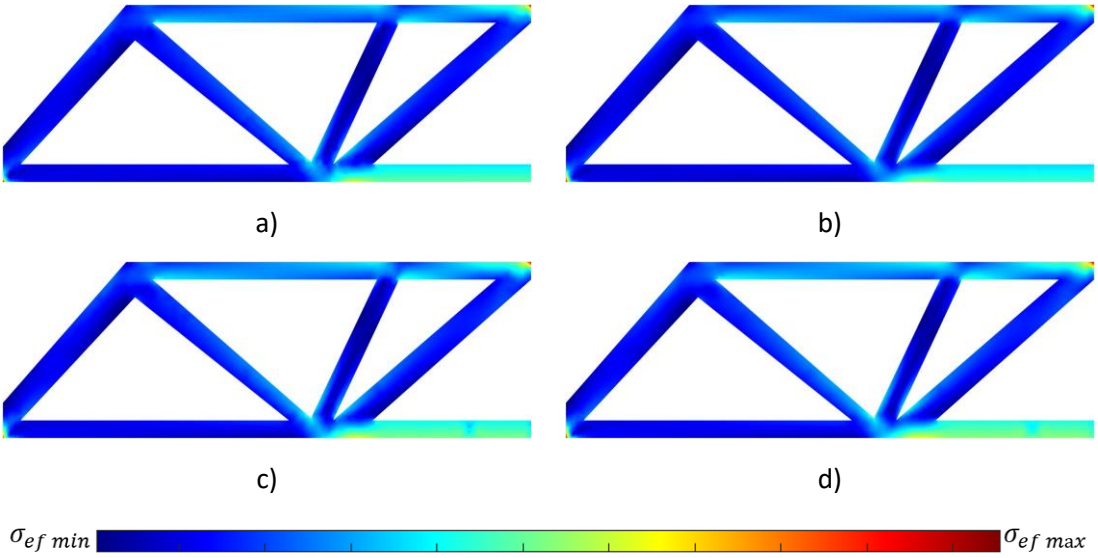

Figure 66. NNRPIM V2 Simply supported beam; a) FEM ($\sigma_{ef\ max} = 3.95\ \times 10^{6}\ Pa;\ \sigma_{ef\ min} = 1.48\ \times 10^{4}\ Pa$); b) RPIM ($\sigma_{ef\ max} = 4.24\ \times 10^{6}\ Pa;\ \sigma_{ef\ min} = 1.19\ \times 10^{4}\ Pa$); c) NNRPIM V1 ($\sigma_{ef\ max} = 3.74\ \times 10^{6}\ Pa;\ \sigma_{ef\ min} = 1.52\ \times 10^{4}\ Pa$); d) NNRPIM V2 ($\sigma_{ef\ max} = 3.59\ \times 10^{6}\ Pa;\ \sigma_{ef\ min} = 1.26\ \times 10^{4}\ Pa$)

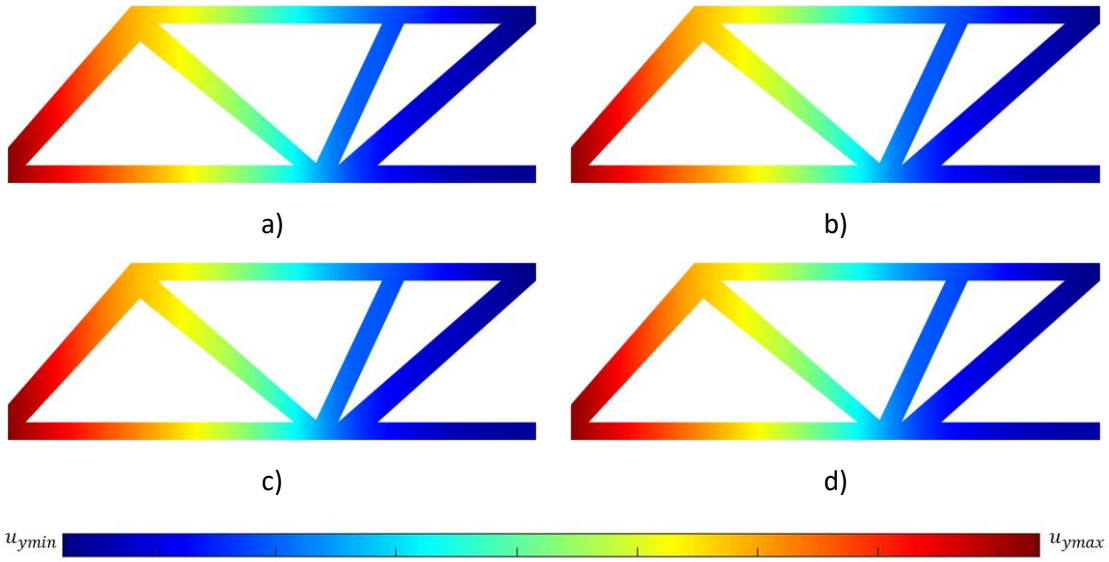

Figure 67. NNRPIM V2 Simply supported beam. a) FEM ($u_{max} = 0;\ u_{min} = -8.92 \times 10^{-5}\ m$); b) RPIM ($u_{max} = 0;\ u_{min} = -8.97 \times 10^{-5}\ m$); c) NNRPIM V1 ($u_{max} = 0;\ u_{min} = -8.96 \times 10^{-5}\ m$); d) NNRPIM V2 ($u_{max} = 0;\ u_{min} = -8.90 \times 10^{-5}\ m$)

In methods contrast to the simply supported beams, the fully constrained structures, shown from Figure 68a) to Figure 68d), exhibit higher Von Mises stress values across all simulation. The highest stress was recorded using the NNRPIM V1 method, while the FEM method yielded the lowest among this group. This increase in stress levels may be attributed to the absence of a lower truss connected to the bottom support in the fully constrained configurations. The

presence of a lower truss in the simply supported models appears to increase force distribution, reducing stress concentrations areas. It is important to note that the fully-supported structure was kept unchanged throughout the elastostatic studies, as the optimization results consistently showed similar outcomes across all cases.

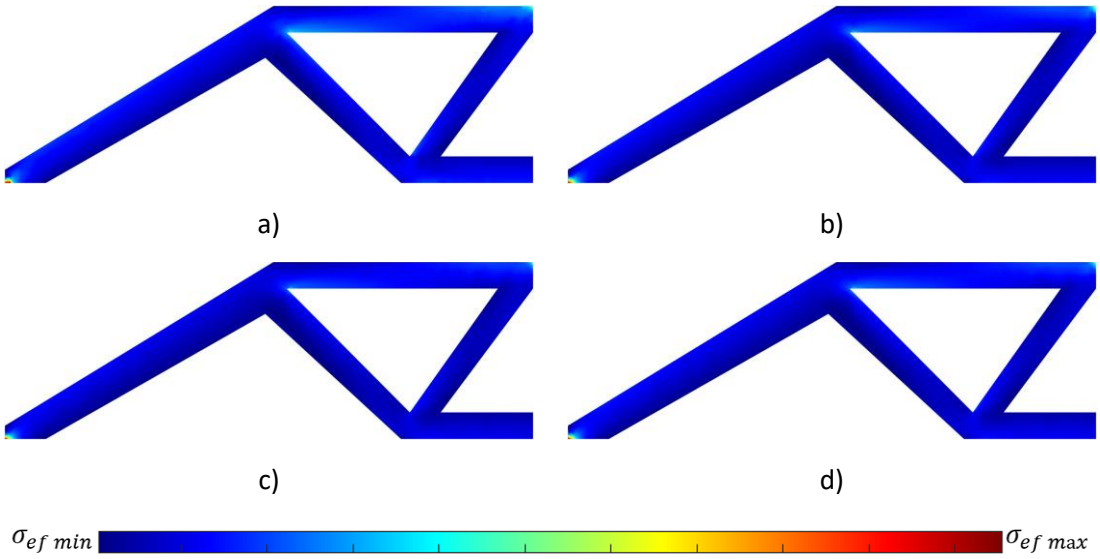

Figure 68. Fully supported beam; a) FEM ($\sigma_{ef\ max} = 5.28 \times 10^6\ Pa;\ \sigma_{ef\ min} = 1.89 \times 10^4\ Pa$); b) RPIM ($\sigma_{ef\ max} = 6.31 \times 10^6\ Pa;\ \sigma_{ef\ min} = 1.62 \times 10^4\ Pa$); c) NNRPIM V1 ($\sigma_{ef\ max} = 7.12 \times 10^6\ Pa;\ \sigma_{ef\ min} = 1.52 \times 10^4\ Pa$); d) NNRPIM V2 ($\sigma_{ef\ max} = 6.63 \times 10^6\ Pa;\ \sigma_{ef\ min} = 1.62 \times 10^4\ Pa$)

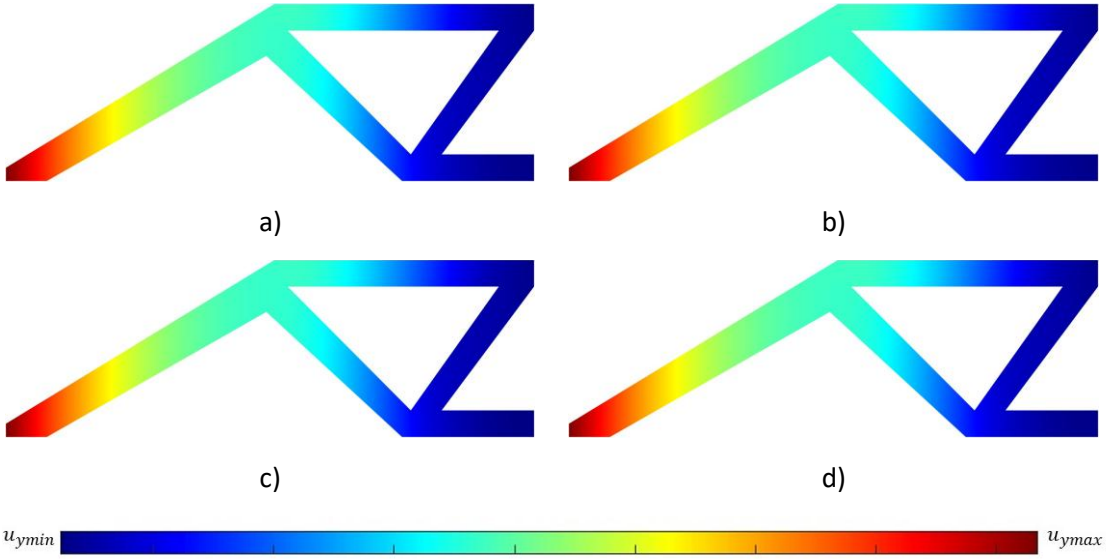

Figure 69. Fully supported beam. a) FEM ($u_{max} = 0;\ u_{min} = -4.54 \times 10^{-5}\ m$); b) RPIM ($u_{max} = 0;\ u_{min} = -4.59 \times 10^{-5}\ m$); c) NNRPIM V1 ($u_{max} = 0;\ u_{min} = -4.65 \times 10^{-5}\ m$); d) NNRPIM V2 ($u_{max} = 0;\ u_{min} = -4.58 \times 10^{-5}\ m$)

Following the analysis of all structures, their respective stiffness values can now be determined. To do so, the applied force will be used in combination with the displacement measured at the point where the force was applied. By dividing the force by this displacement ($\frac{F}{d}$), the stiffness of the structure can be calculated. In Table 5 it is possible to observe the stiffness values of each structure, according to the method used in the studies.

Table 5. Structure stiffness values

STIFFNESS [kN/mm]				
Structure	FEM	RPIM	NNRPIM V1	NNRPIM V2
Figure 60	295	293	293	295
Figure 62	278	276	276	277
Figure 64	313	311	311	312
Figure 66	224	222	223	224
Figure 68	440	435	429	436

When analysing the stiffnesses presented in Table 5, it is possible to determine that the structure generated by the NNRPIM V1 method (Figure 64), possesses the highest stiffness when compared with the other simply-supported structures, especially when analysed with FEM. On the other hand, the structure obtained with the NNRPIM V2 method (Figure 66), yields lower stiffness values when compared to the simply-supported structures generated by the other methods. Although the NNRPIM V2 method yielded lower stiffness values compared to the other approaches, its selection for the rover optimization was not based solely on stiffness performance. Instead, this method was chosen due to its overall balance between accuracy and stability across different mesh configurations, making it the most suitable candidate for the subsequent optimization process. It is important to note that the fully-supported structure presented in Figure 68 disposes of the highest stiffnesses among every case studied, meaning that the displacements involved in this structure were the lowest.

6. Perseverance Rover rocker-bogie

In this chapter, the rocker-bogie suspension system of the Perseverance Rover is structurally optimized, utilizing the NNRPIM method with only second-degree influence cells and a decrease ratio of 0.02 for the BONE method and 0.05 for the BESO. The obtained results will then be 3D modelled utilizing CAM programs, in order to demonstrate and observe the different sights of the rocker-bogie. The objective of such study is to achieve the most optimal solution for the suspension system.

6.1. Rocker-bogie structure

The rocker-bogie suspension system of NASA's Perseverance Rover is a fundamental component of its six wheeled mobility platform, designed to optimize stability as well as manoeuvrability across the rugged Martian surface. This system enables the rover to navigate across rocks, slopes and craters while keeping the main body levelled and reducing mechanical stress. As it was stated in chapter 2.4.1, the suspension system consists of two rocker arms connected to two shorter bogies forming a passive suspension system that balances the movement across both sides of the rover via a central differential. Such design permits the rover to climb over obstacles up to the wheel diameter while distributing the forces evenly.

Due to the fact that such structure needs a high strength as well as being lightweight, the suspension system is made of Ti-6Al-4V STA. Since that in further computations, some data about related to the material is needed, in Table 6 it is possible to observe the important mechanical properties and each of its values.

Table 6. Mechanical properties of Ti-6Al-4V STA [48][49]

Mechanical properties	Value
Young's Modulus	113.8 GPa
Poisson's ratio	0.342
Yield strength	1035 MPa
Tensile strength	1100 MPa
Density	4.43 g/cm^3

6.2. Rocker-bogie numerical analysis

This stage, which consists of the re-design of the bogie's suspension system using structural optimization techniques, focuses on refining the geometry and material distribution of the suspension system in order to achieve the best possible balance between mechanical performance and density.

6.2.1. Initial geometry and meshing

To initiate the structural optimization process, a simplified rectangular two-dimensional model was built, employing FEMAP software, to represent the initial geometry of the rocker bogie suspension system. The domain was modelled as a rectangle with the total length of 3 m and a height of 1 m, with the dimensions obtained with the assistance of the STL file model provided by NASA. This initial geometry functioned as a neutral baseline, providing flexibility to observe how material redistributions develop under boundary and loading conditions. In order to illustrate every important dimension, Figure 70 is presented.

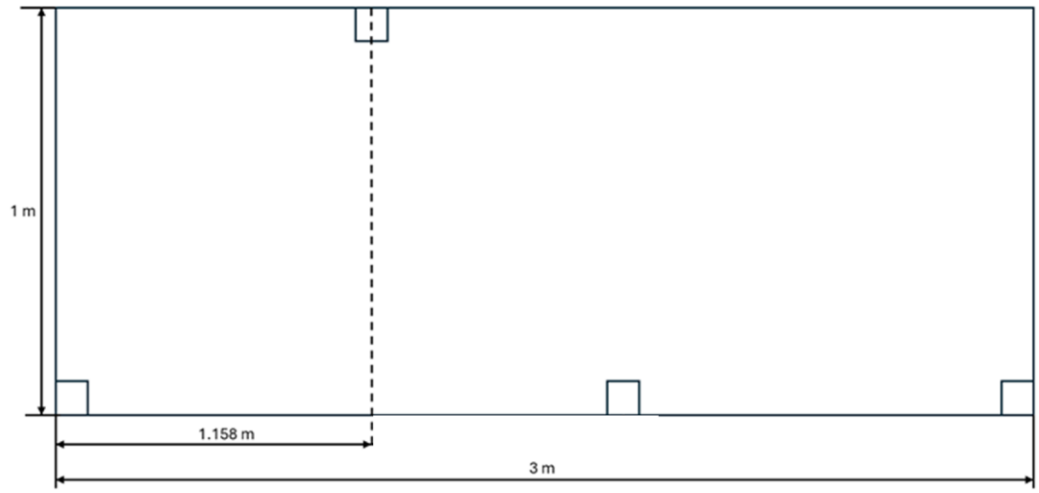

Figure 70. Initial geometry dimensions sketch

Within the rectangular domain, certain areas, designated as non-removable, corresponding to the connection points and structural interfaces that are critical for mechanical connectivity, such as the connection with the rover's wheels. Such areas are defined as small rectangular pads and remain unchanged during the optimization process to preserve the functional role of the original structure. Both the initial geometry and the non-removable areas (red rectangle) can be seen in Figure 71a) and Figure 71b), respectively. Regarding the material used in the numerical simulations, Ti-6Al-4V STA was selected. The corresponding mechanical properties are detailed in Table 6. The material density varies depending on the optimization method employed. In the Bone Remodelling approach, a maximum density of 2.1 g/cm^3 was applied, whereas in the BESO method, the maximum density was set to 1.0 g/cm^3. For the non-removable regions, a constant density of 4.43 g/cm^3 was assigned across all optimization methods. This value exceeds the maximum allowable density in the modifiable regions and

serves to effectively prevent material removal or redistribution in these structurally critical zones.

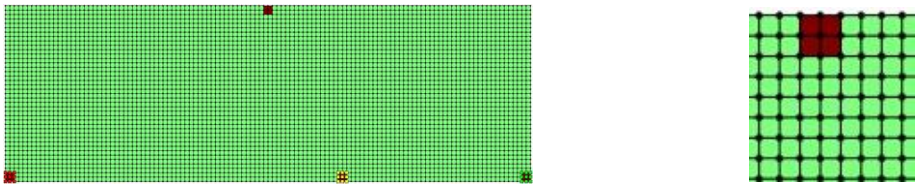

a) b)

Figure 71. a) Initial rectangular geometry; b) Non-removable region

In order to obtain more reliable and accurate results, a refined mesh was adopted by selecting an element size of 0.025. Such choice resulted in a significantly denser discretization of the computational domain, allowing for more precise identification of regions to subject to material redistribution during the optimization process. With this mesh size, 4800 elements were discretized into the domain.

6.2.2. Boundary conditions

The initial boundary conditions were defined to accurately represent the structural constraints and loading conditions of the suspension system. As previously mentioned, the model includes an upper non-removable support region, where displacements were constrained in both the *x* and *y* directions, reflecting the structural restrictions of the actual system. Regarding the loading conditions, the total vertical force acting on the full suspension system is 1025 kg which corresponds to the weight of the Perseverance Rover. However, since the suspension consists of two symmetric units and only one side was analysed, the applied load was halved, resulting in a vertical force of 512.5 kg (5027.63 N). To more accurately represent the physical behaviour of the structure, this force was decomposed and distributed among three lower non-removable regions. In order to fully understand how the total force applied in the rover is decomposed across every wheel, the calculation process of each intensity is described. The calculation of the forces begins with the bogie, as it serves as the starting point for the overall force distribution throughout the system. This distribution is illustrated in the Figure 72, where the transmission of forces from the bogie to the rest of the structure can be clearly observed. Additionally, the complete calculation of the forces acting on the bogie is shown through the system of equations presented in equation (42), which provides a detailed representation of the equilibrium conditions and internal force components.

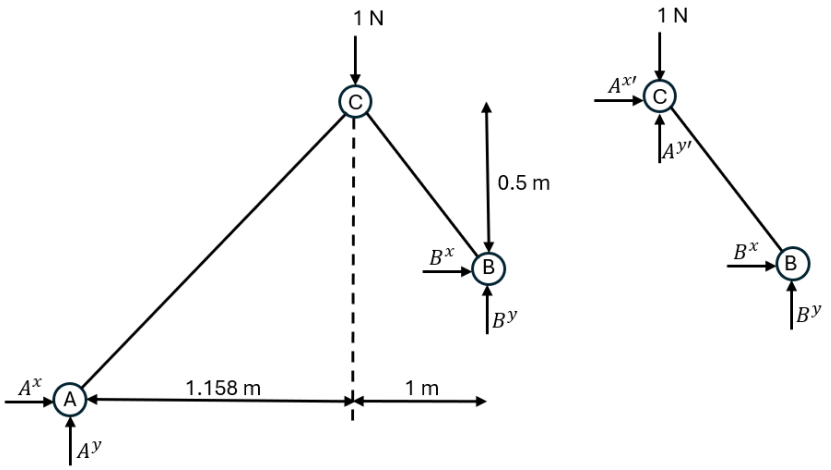

Figure 72. Bogie force distribution

$$\begin{cases} \sum F_x = 0 \\ \sum F_y = 0 \\ \sum M_A = 0 \\ \sum M_C = 0 \end{cases} = \begin{cases} A^x + B^x = 0 \\ A^y + B^y - 1 = 0 \\ -1 \times 1.158 + B^y \times 2.158 - B^x \times 0.5 = 0 \\ B^y \times 1 + B^x \times 0.5 = 0 \end{cases} = \begin{cases} A^x = 0.733\ N \\ A^y = 0.633\ N \\ B^x = -0.733\ N \\ B^y = 0.366\ N \end{cases} \quad (42)$$

Now that the calculation of the rocker is completed, the forces determined at point B will be used to calculate the remaining forces acting on the rocker. The distribution of these forces is illustrated in the Figure 73. The system of equations used to perform these calculations is presented in equation (43), which details the relationships and equilibrium conditions involved.

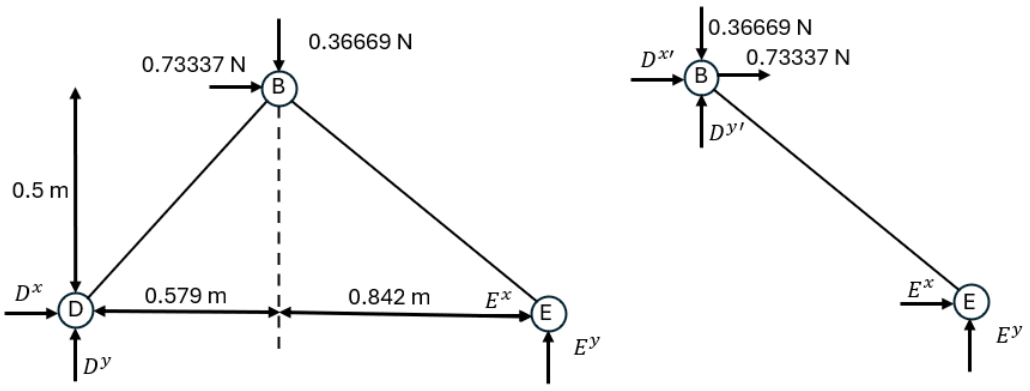

Figure 73. Rocker force distribution

$$\begin{cases} \sum F_x = 0 \\ \sum F_y = 0 \\ \sum M_D = 0 \\ \sum M_B = 0 \end{cases} = \begin{cases} D^x + E^x + 0.73337 = 0 \\ D^y + E^y - 0.36669 = 0 \\ -0.36669 \times 0.579 - 0.73337 \times 0.5 + E^y \times (0.579 + 0.842) = 0 \\ E^y \times 0.842 + E^x \times 0.5 = 0 \end{cases} \quad (43)$$

$$= \begin{cases} D^x = -0.0472\ N \\ D^y = -0.0407\ N \\ E^x = -0.686\ N \\ E^y = 0.407\ N \end{cases}$$

With the calculation of all forces now completed, it is possible to combine all the results and obtain the final diagram shown in Figure 74, where all the acting forces are represented. It is important to note that a unitary force of 1 N was used throughout the calculation process. Once all force magnitudes have been determined, they will be multiplied by the actual weight of the rover (in newtons - 5027.63 N) to obtain the correct acting force intensities.

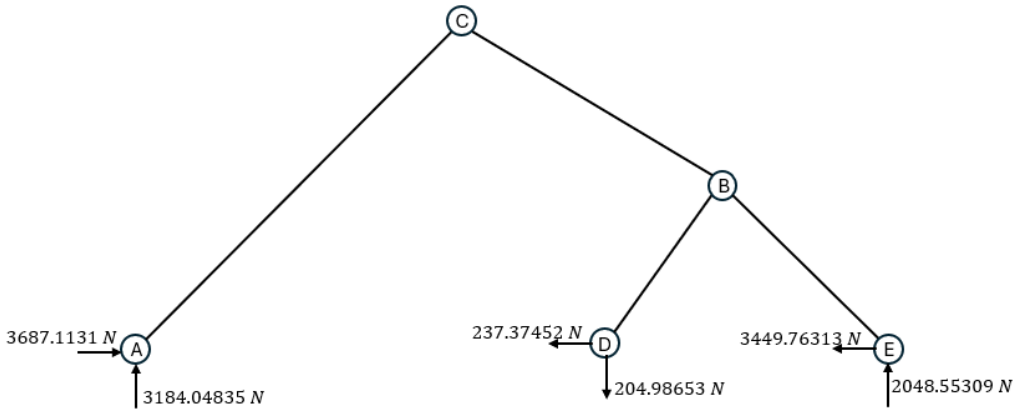

Figure 74. Force distribution sketch

6.2.3. Initial structural optimization

Using all the conditions defined in chapters 6.2.1 and 6.2.2 the first structural optimization was performed utilizing the NNRPIM method with only second-degree influence cells with a decrease ratio of 0.02 for the Bone remodelling method and a decrease ratio of 0.05 for BESO, since they were the ones that produced the most optimal results when analysing the example in chapter 5.2. No changes were made to any of the initial settings since the focus of the first optimization was to observe the structure behaviour under such conditions as well as if it was possible to obtain an ideal and efficient structure without interfering with the initial conditions. These first results serve as a starting point for comparison in future steps of the study. As it is possible to observe in Figure 75a), the suspension system of the rover was optimized using the Bone remodelling method. The obtained structure was aligned with the expectations and resembled the actual suspension system of the current rover. This highlights the effectiveness of the BONE method in generating efficient designs. As for Figure 75b), the optimization was

performed using the BESO method. As it is possible to observe, the BESO method produced a structure that partially resembles the original structure, as well as the structure generated by the BONE method. In summary, it can be stated that the BONE method produced the best structure.

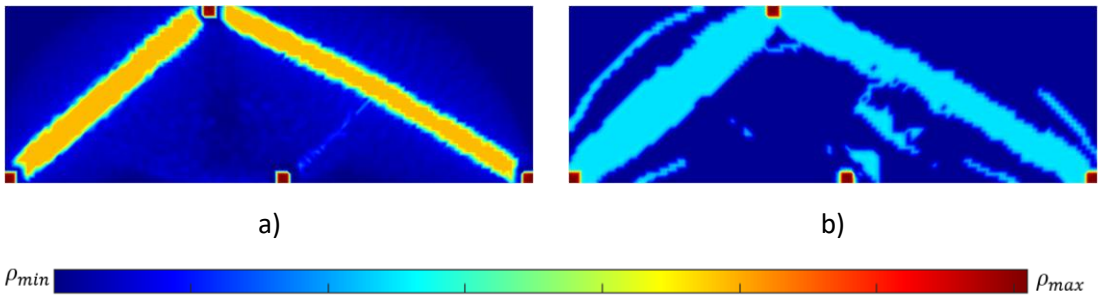

Figure 75. Structure with full reactions a) Bone Remodelling ($\rho_{ef\ max} = 4.43 g/cm^3$; $\rho_{ef\ min} = 0 g/cm^3$); b) BESO ($\rho_{ef\ max} = 4.43 g/cm^3$; $\rho_{ef\ min} = 0\ g/cm^3$)

In order to understand how the structure would behave in different loading scenarios, the reactions in the x-direction, previously calculated, were removed. Such can be interesting if there is the need of a configuration that removes the freedom across wheels, adding a reinforcement between them. The obtained structures with bone remodelling and the BESO method can be observed in Figure 76a) and Figure 76b), respectively.

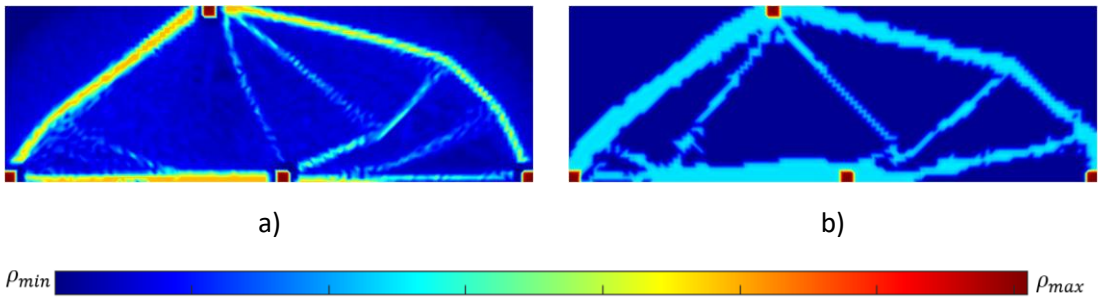

Figure 76. Structure without the x-direction reactions a) Bone Remodelling ($\rho_{ef\ max} = 4.43 g/cm^3$; $\rho_{ef\ min} = 0 g/cm^3$); b) BESO ($\rho_{ef\ max} = 4.43 g/cm^3$; $\rho_{ef\ min} = 0 g/cm^3$)

Analysing both the results obtained in Figure 76 it is possible to observe that the requirements were met, resulting in a structure with no wheel freedom, when compared to the structures obtained in Figure 75.

6.2.4. Elastostatic studies

With all optimizations completed, it is now possible to analyse the most optimal suspension system structures obtained. Notably, the BONE method demonstrated superior performance in the case involving reaction forces in both the *x* and *y* directions, yielding a more efficient structural configuration (see Figure 75a)). In contrast, for the scenario considering only vertical forces, both methods were able to produce comparably optimal structures, as it is possible to observe in Figure 76. The main objective of this analysis is to understand the stress distribution throughout the structure and the evaluate the structures' maximum Von Misses stress. In Figure 77 it is possible to observe the studies referent to the structure obtained in Figure 75a),

whereas Figure 79 and Figure 81 represent both the structures described in Figure 76a) and Figure 76b) respectively.

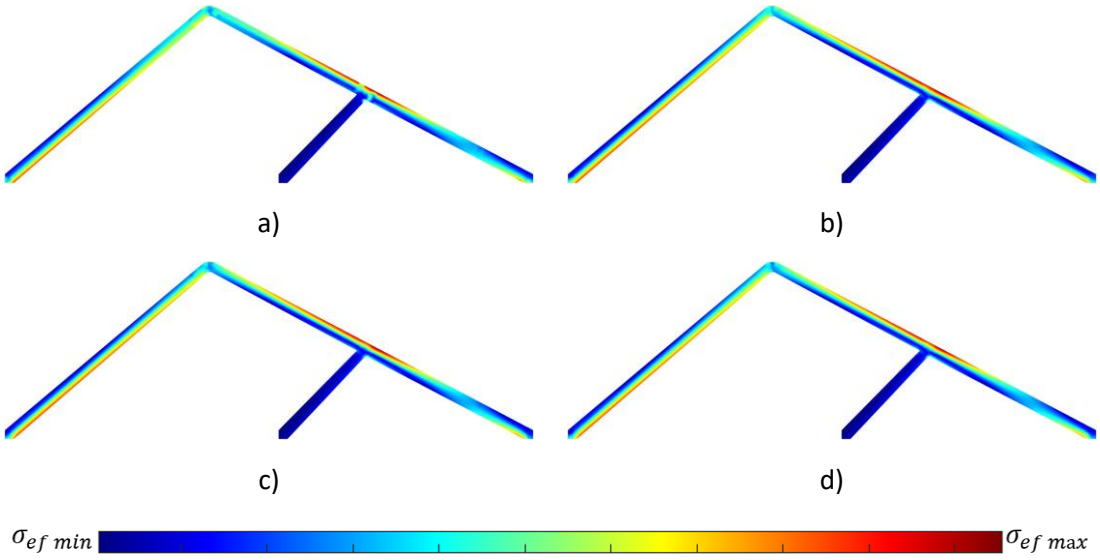

Figure 77. BONE with both reactions (Von Misses stress). a) FEM ($\sigma_{ef\ max} = 3.86 \times 10^6\ Pa;\ \sigma_{ef\ min} = 1.67 \times 10^4\ Pa$); b) RPIM ($\sigma_{ef\ max} = 3.82 \times 10^6\ Pa;\ \sigma_{ef\ min} = 1.93 \times 10^4\ Pa$); c) NNRPIM V1 ($\sigma_{ef\ max} = 3.85 \times 10^6\ Pa;\ \sigma_{ef\ min} = 1.94 \times 10^4\ Pa$); d) NNRPIM V2 ($\sigma_{ef\ max} = 3.91 \times 10^6\ Pa;\ \sigma_{ef\ min} = 1.90 \times 10^4\ Pa$)

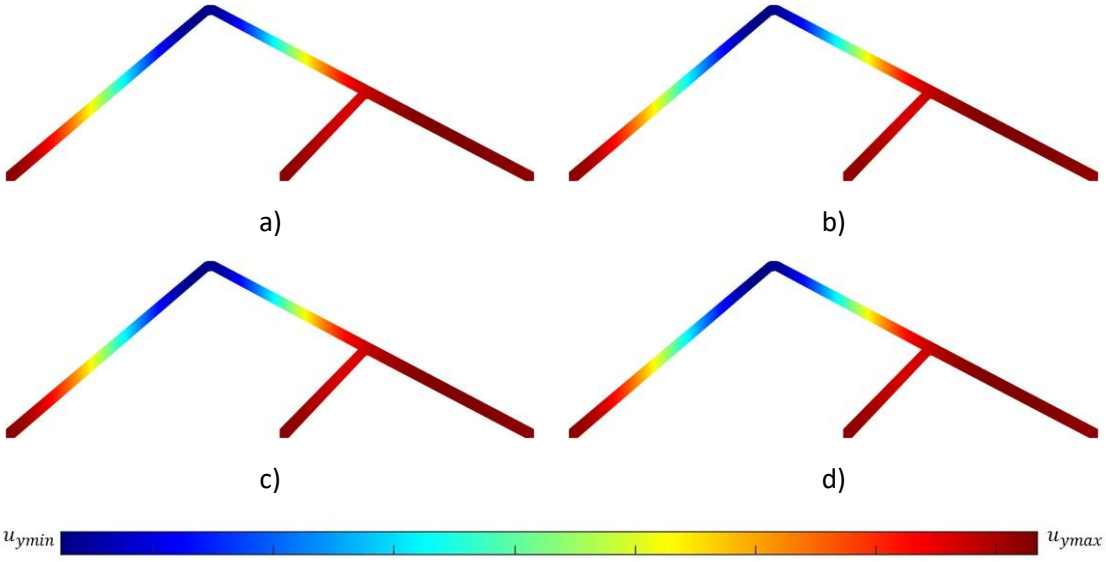

Figure 78. BONE with both reactions (Displacements). a) FEM ($u_{max} = 0;\ u_{min} = -2.18 \times 10^{-3} m$); b) RPIM ($u_{max} = 0;\ u_{min} = -2.61 \times 10^{-3} m$); c) NNRPIM V1 ($u_{max} = 0;\ u_{min} = -2.78 \times 10^{-3} m$); d) NNRPIM V2 ($u_{max} = 0;\ u_{min} = -2.45 \times 10^{-3} m$)

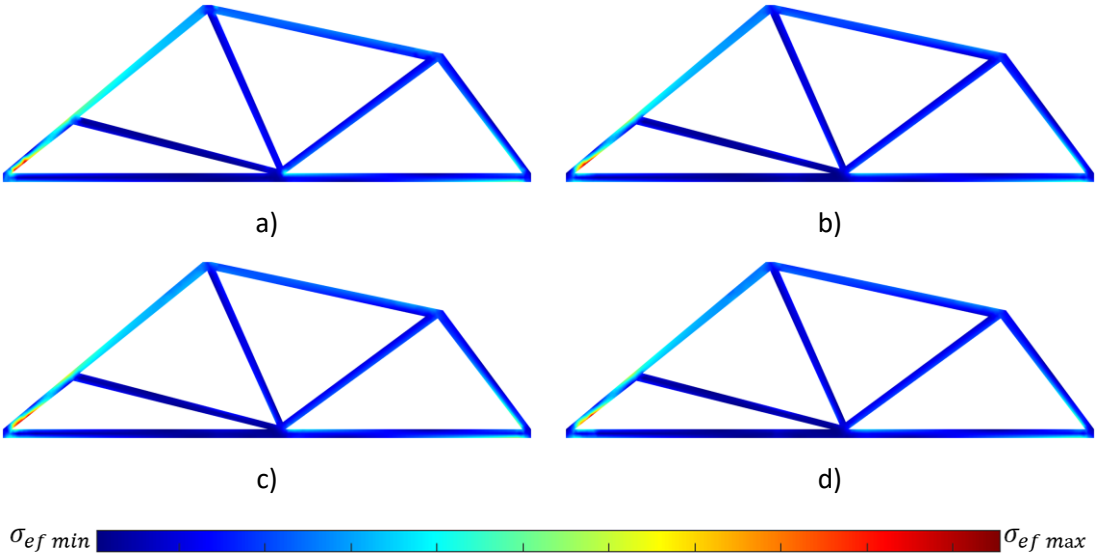

Figure 79. BONE with vertical reactions (Von Misses stress). a) FEM ($\sigma_{ef\ max} = 6.25 \times 10^6\ Pa;\ \sigma_{ef\ min} = 4.06 \times 10^4\ Pa$); b) RPIM ($\sigma_{ef\ max} = 7.20 \times 10^6\ Pa;\ \sigma_{ef\ min} = 4.58 \times 10^4\ Pa$); c) NNRPIM V1 ($\sigma_{ef\ max} = 6.61 \times 10^6\ Pa;\ \sigma_{ef\ min} = 2.21 \times 10^4\ Pa$); d) NNRPIM V2 ($\sigma_{ef\ max} = 7.09 \times 10^6\ Pa;\ \sigma_{ef\ min} = 4.72 \times 10^4\ Pa$)

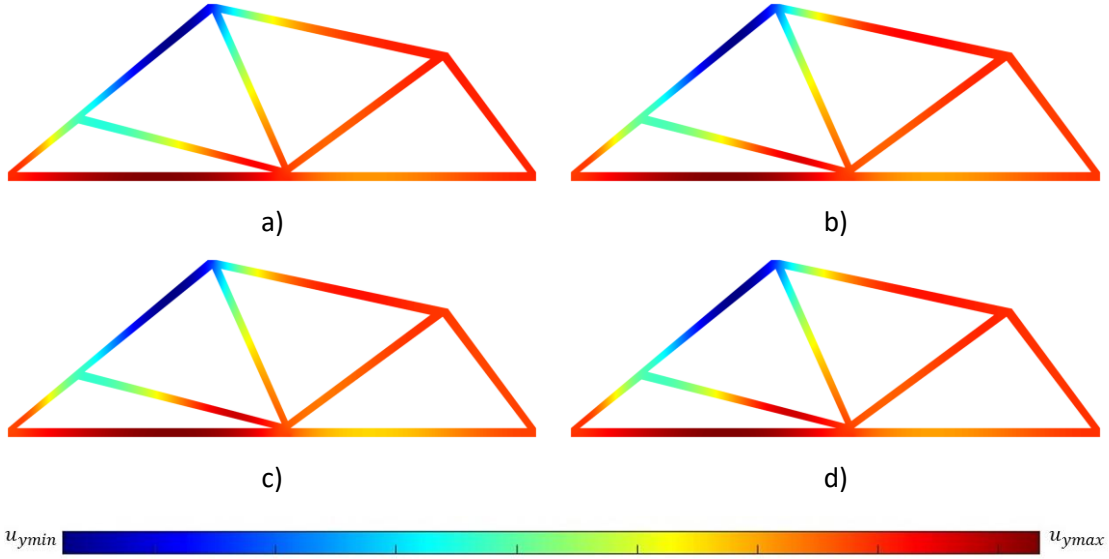

Figure 80. BONE with vertical reactions (Displacements). a) FEM ($u_{max} = 0;\ u_{min} = -2.35 \times 10^{-5} m$); b) RPIM ($u_{max} = 0;\ u_{min} = -2.40 \times 10^{-5} m$); c) NNRPIM V1 ($u_{max} = 0;\ u_{min} = -2.40 \times 10^{-5} m$); d) NNRPIM V2 ($u_{max} = 0;\ u_{min} = -2.30 \times 10^{-5} m$)

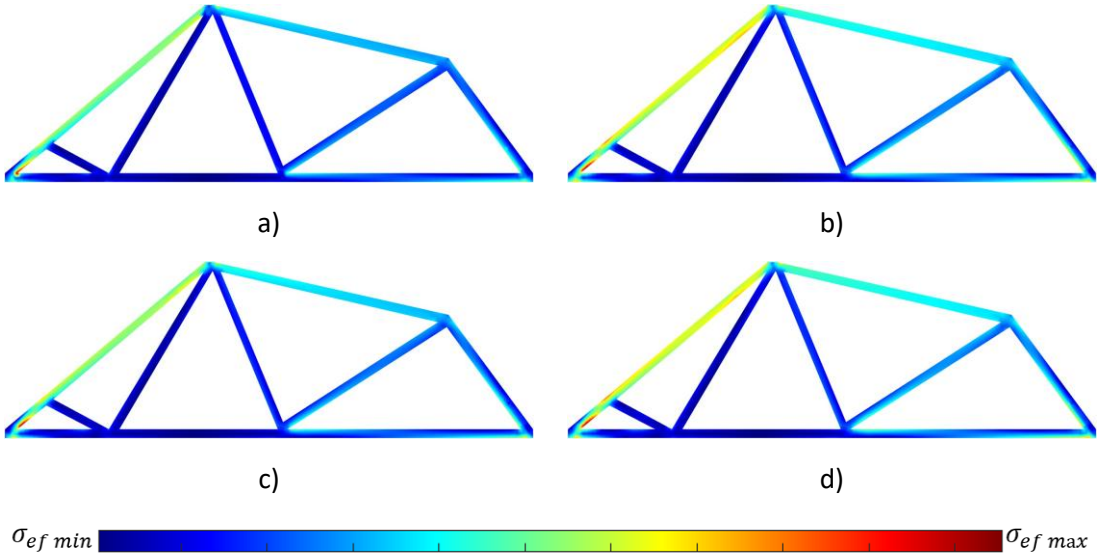

Figure 81. BESO with vertical reactions (Von Misses stress). a) FEM ($\sigma_{ef\ max} = 4.27 \times 10^6\ Pa;\ \sigma_{ef\ min} = 1.47 \times 10^4\ Pa$); b) RPIM ($\sigma_{ef\ max} = 3.59 \times 10^6\ Pa;\ \sigma_{ef\ min} = 6.36 \times 10^3\ Pa$); c) NNRPIM V1 ($\sigma_{ef\ max} = 3.95 \times 10^6\ Pa;\ \sigma_{ef\ min} = 1.67 \times 10^4\ Pa$); d) NNRPIM V2 ($\sigma_{ef\ max} = 3.47 \times 10^6\ Pa;\ \sigma_{ef\ min} = 2.01 \times 10^4\ Pa$)

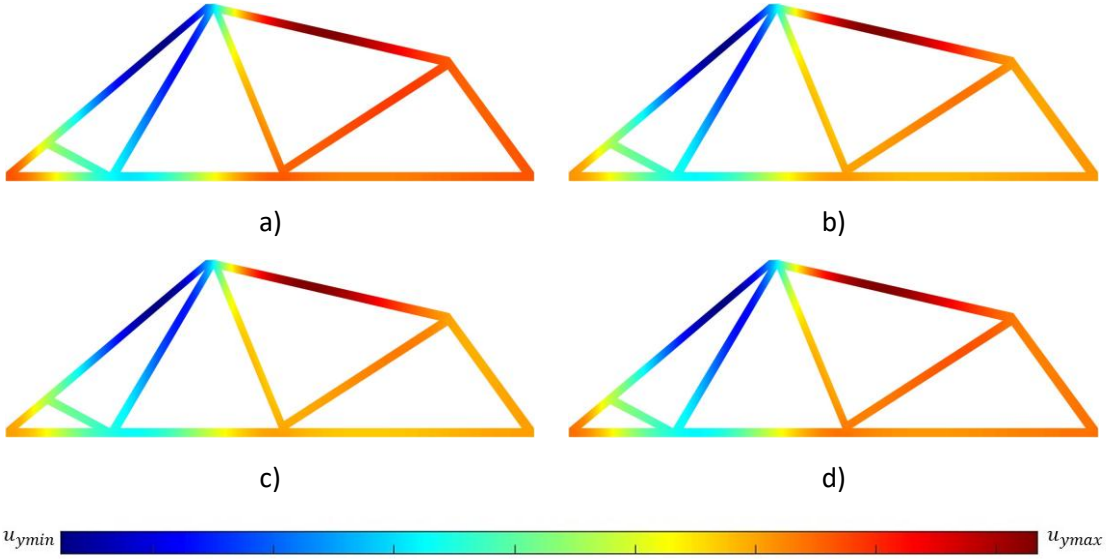

Figure 82. BESO with vertical reactions (Displacements). a) FEM ($u_{max} = 0;\ u_{min} = -2.32 \times 10^{-5} m$); b) RPIM ($u_{max} = 0;\ u_{min} = -2.40 \times 10^{-5} m$); c) NNRPIM V1 ($u_{max} = 0;\ u_{min} = -2.50 \times 10^{-5} m$); d) NNRPIM V2 ($u_{max} = 0;\ u_{min} = -2.40 \times 10^{-5} m$)

As can be observed in Figure 77, the maximum von Mises stress evaluated by each method shows minor differences, indicating strong consistency across all approaches. Although the NNRPIM V2 method was chosen to generate the optimized structures, it was the one that exhibited the highest von Mises stress in elastostatic analysis. When analysing Figure 79, it is evident that the structure obtained using the BONE method, considering only vertical reactions, exhibits the highest maximum von Mises stress values, when compared to the structures presented in Figure 77 and Figure 81. On the other hand, in Figure 81d) it is possible to

understand that the structure created by the BESO method yields the lower Von Misses stress value of every method and structure. This furthermore proves that the NNRPIM V2 method produces feasible results when generating optimized structures. Comparing each structure obtained, with the original suspension system, presented across Figure 83a) to Figure 83d), it becomes evident that every structure generated through the optimization method not only exhibits a lower maximum von Mises stress than the original design, but also remains well below the material's yield strength. Such proves that the optimized structures obtained are coherent and are fully capable of maintaining the rovers' safety while operating.

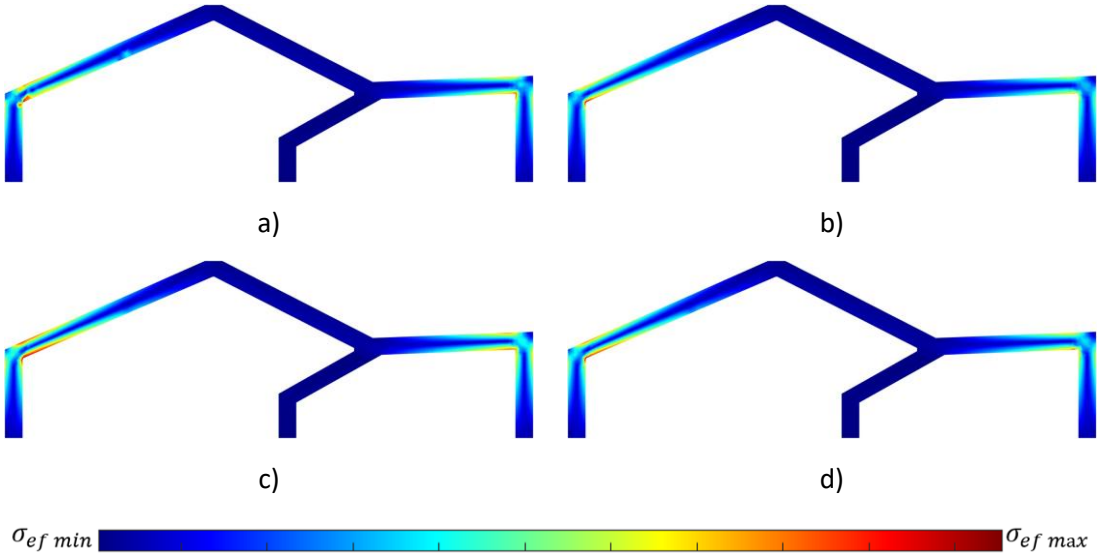

Figure 83. Original suspension system. a) FEM ($\sigma_{ef\ max} = 1.39 \times 10^7\ Pa;\ \sigma_{ef\ min} = 1.54 \times 10^4\ Pa$); b) RPIM ($\sigma_{ef\ max} = 1.55 \times 10^7\ Pa;\ \sigma_{ef\ min} = 2.66 \times 10^4\ Pa$); c) NNRPIM V1 ($\sigma_{ef\ max} = 1.28 \times 10^7\ Pa;\ \sigma_{ef\ min} = 2.28 \times 10^4\ Pa$); d) NNRPIM V2 ($\sigma_{ef\ max} = 1.40 \times 10^7\ Pa;\ \sigma_{ef\ min} = 2.48 \times 10^4\ Pa$)

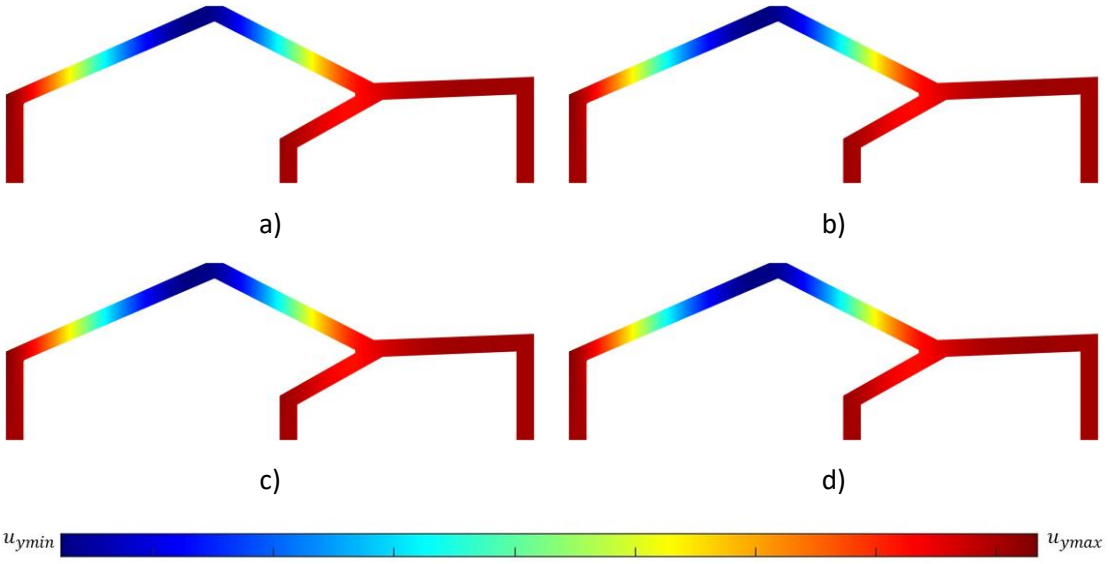

Figure 84. Original suspension system displacements. a) FEM ($u_{max} = 0;\ u_{min} = -3.39 \times 10^{-4} m$); b) RPIM ($u_{max} = 0;\ u_{min} = -3.66 \times 10^{-4} m$); c) NNRPIM V1 ($u_{max} = 0;\ u_{min} = -3.76 \times 10^{-4} m$); d) NNRPIM V2 ($u_{max} = 0;\ u_{min} = -3.58 \times 10^{-4} m$)

Despite the maximum Von misses stress being a key indicator on whether a structure is mechanically capable or not, analysing the stiffness of the structure is also relevant. Since the optimized structures exhibit different masses, a normalized stiffness will be determined to enable a reasonable comparison. This normalized stiffness is obtained by dividing the structure stiffness by its mass.

Table 7. Suspension systems normalized stiffnesses

STIFFNESS [N/mm/kg]				
Structure	FEM	RPIM	NNRPIM V1	NNRPIM V2
BONE with both reactions	38.66	32.39	30.37	34.49
BONE with vertical reactions	2120.43	2115.27	2057.01	2135.89
BESO with vertical reactions	2036.45	1989.11	1892.82	1992.92
Original structure	71.13	65.79	64.11	67.66

From Table 7, it can be observed that the structure presented in Figure 77 yields a normalized stiffness that is roughly half of the original suspension system. This reduction is primarily due to its similar geometry, however with bars of approximately half the dimensions which lowers its stiffness. On the contrary, the structures of Figure 79 and Figure 81 dispose of a much more complex design. Therefore, its experienced a drastic increase in the normalized stiffness of the suspension system. Such occurs due to the incorporation of a higher number of bars, thereby the addition of material and strength.

6.2.5. 3D structures

With the 2D structure analysis completed, it is now possible, through FEMAP, to assign a width parameter to create a 3D representation of the structure by extruding the 2D model in the normal axis to the 2D plane. This approach allows the conversion of initially planar models into three dimensional structures while maintaining the required geometric and mechanical properties. The original structure is modelled with a width of 0.1 m, and the remaining structures are modelled with a width of 0.05 m. The primary objective of this 3D analysis is to verify that the results are of the same order of magnitude and consistent with those obtained from the 2D analysis, in order to reinforce that the structures generated are coherent as well as the methods employed to generate and analyse them.

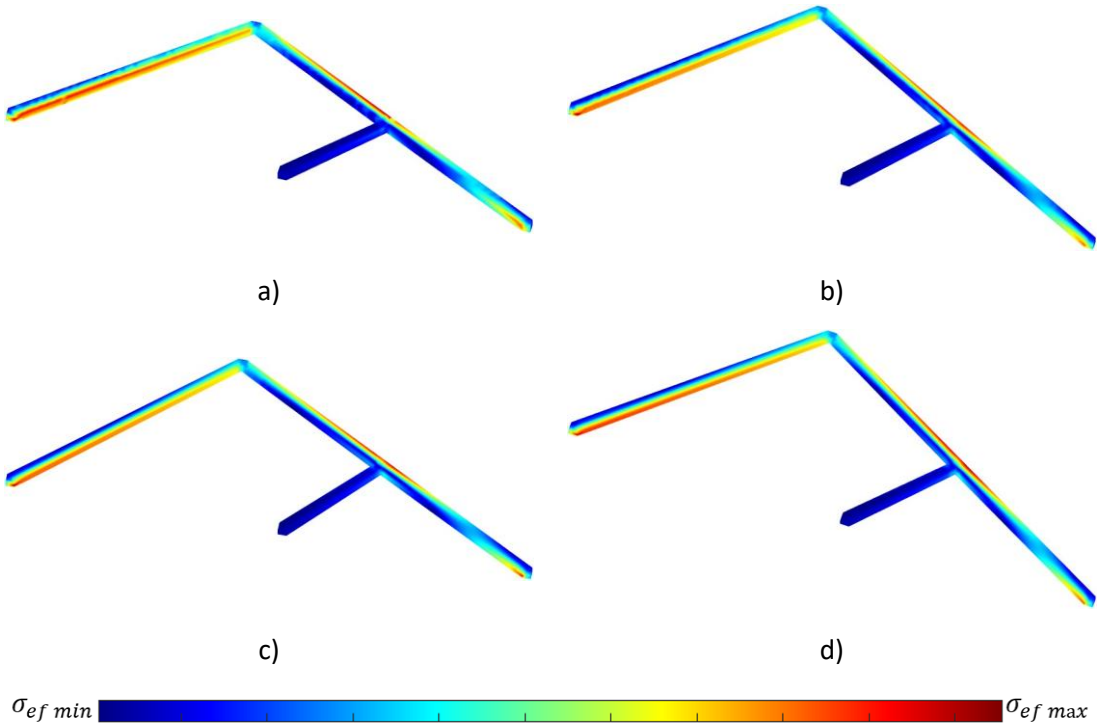

Figure 85. BONE with both reactions (Von Misses stress). a) FEM ($\sigma_{ef\ max} = 3.96 \times 10^6\ Pa;\ \sigma_{ef\ min} = 1.35 \times 10^4\ Pa$); b) RPIM ($\sigma_{ef\ max} = 4.02 \times 10^6\ Pa;\ \sigma_{ef\ min} = 1.70 \times 10^4\ Pa$); c) NNRPIM V1 ($\sigma_{ef\ max} = 4.01 \times 10^6\ Pa;\ \sigma_{ef\ min} = 1.88 \times 10^4\ Pa$); d) NNRPIM V2 ($\sigma_{ef\ max} = 3.75 \times 10^6\ Pa;\ \sigma_{ef\ min} = 1.61 \times 10^4\ Pa$)

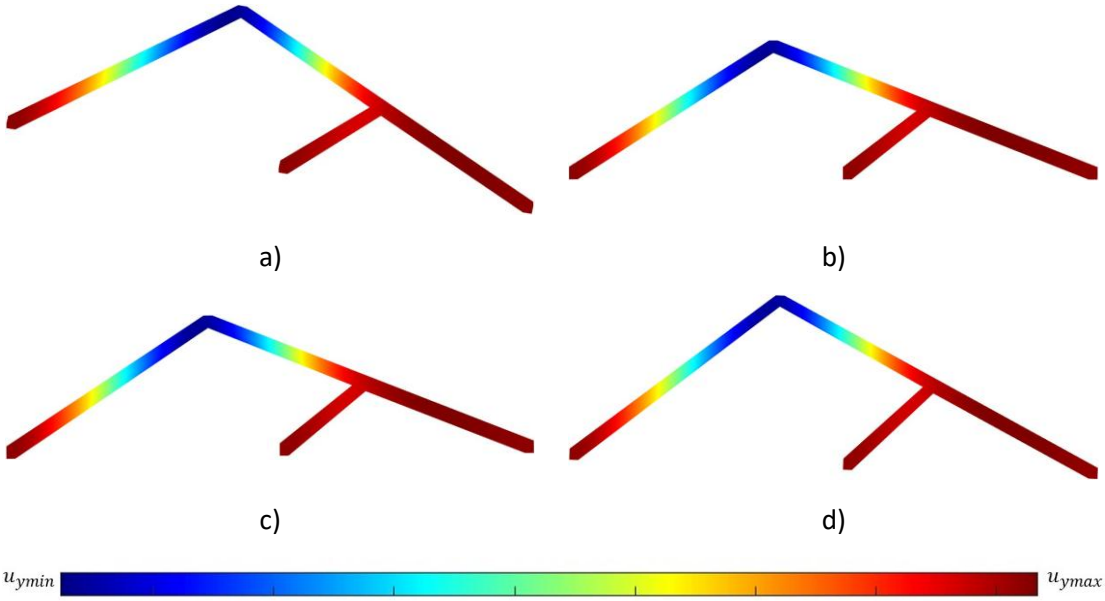

Figure 86. BONE with both reactions (Displacements). a) FEM ($u_{max} = 0;\ u_{min} = -2.12 \times 10^{-3} m$); b) RPIM ($u_{max} = 0;\ u_{min} = -2.60 \times 10^{-3} m$); c) NNRPIM V1 ($u_{max} = 0;\ u_{min} = -2.68 \times 10^{-3} m$); d) NNRPIM V2 ($u_{max} = 0;\ u_{min} = -2.53 \times 10^{-3} m$)

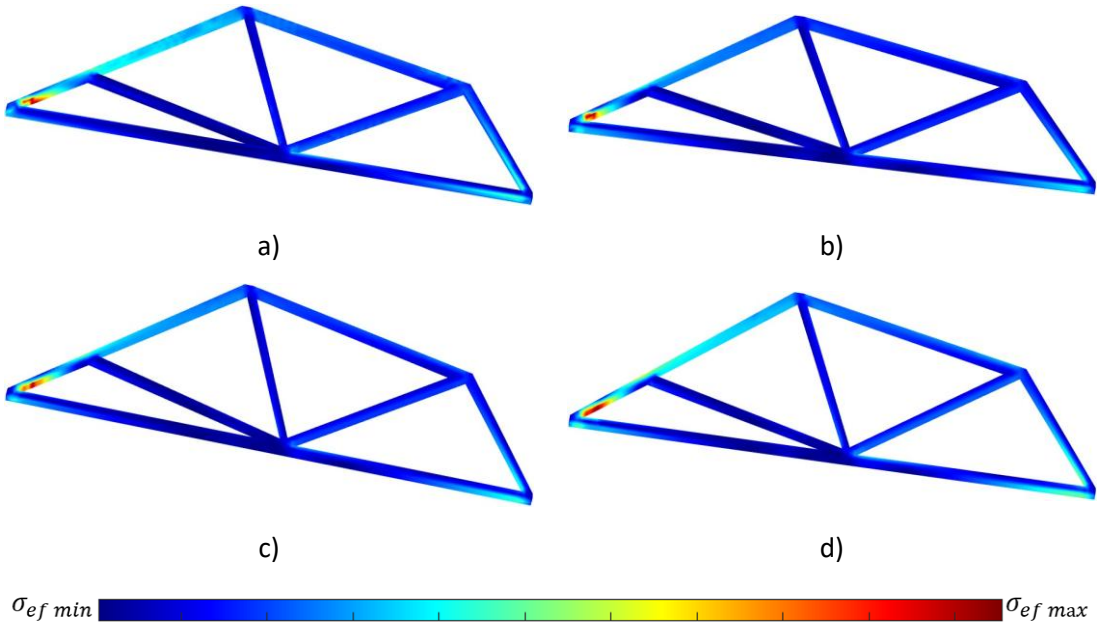

Figure 87. BONE with vertical reactions (Von Misses stress). a) FEM ($\sigma_{ef\ max} = 6.27 \times 10^6\ Pa;\ \sigma_{ef\ min} = 3.27 \times 10^4\ Pa$); b) RPIM ($\sigma_{ef\ max} = 8.82 \times 10^6\ Pa;\ \sigma_{ef\ min} = 1.71 \times 10^4\ Pa$); c) NNRPIM V1 ($\sigma_{ef\ max} = 7.90 \times 10^6\ Pa;\ \sigma_{ef\ min} = 2.78 \times 10^4\ Pa$); d) NNRPIM V2 ($\sigma_{ef\ max} = 6.38 \times 10^6\ Pa;\ \sigma_{ef\ min} = 1.38 \times 10^4\ Pa$)

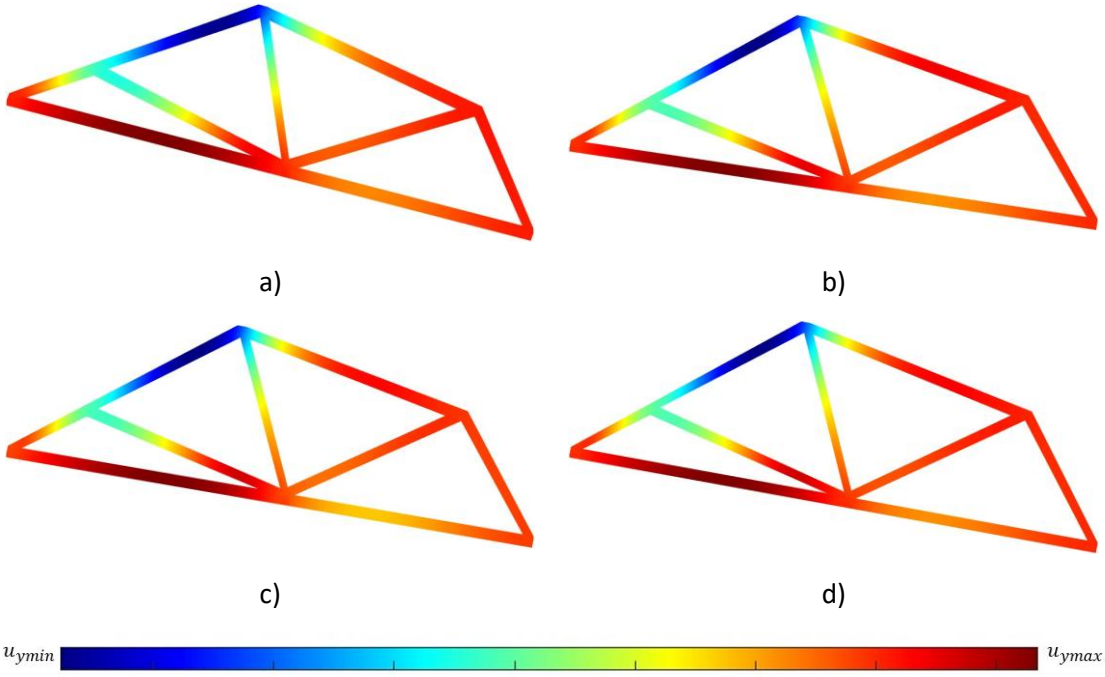

Figure 88. BONE with vertical reactions (Displacements). a) FEM ($u_{max} = 0;\ u_{min} = -2.49 \times 10^{-5} m$); b) RPIM ($u_{max} = 0;\ u_{min} = -2.50 \times 10^{-5} m$); c) NNRPIM V1 ($u_{max} = 0;\ u_{min} = -2.50 \times 10^{-5} m$); d) NNRPIM V2 ($u_{max} = 0;\ u_{min} = -2.40 \times 10^{-5} m$)

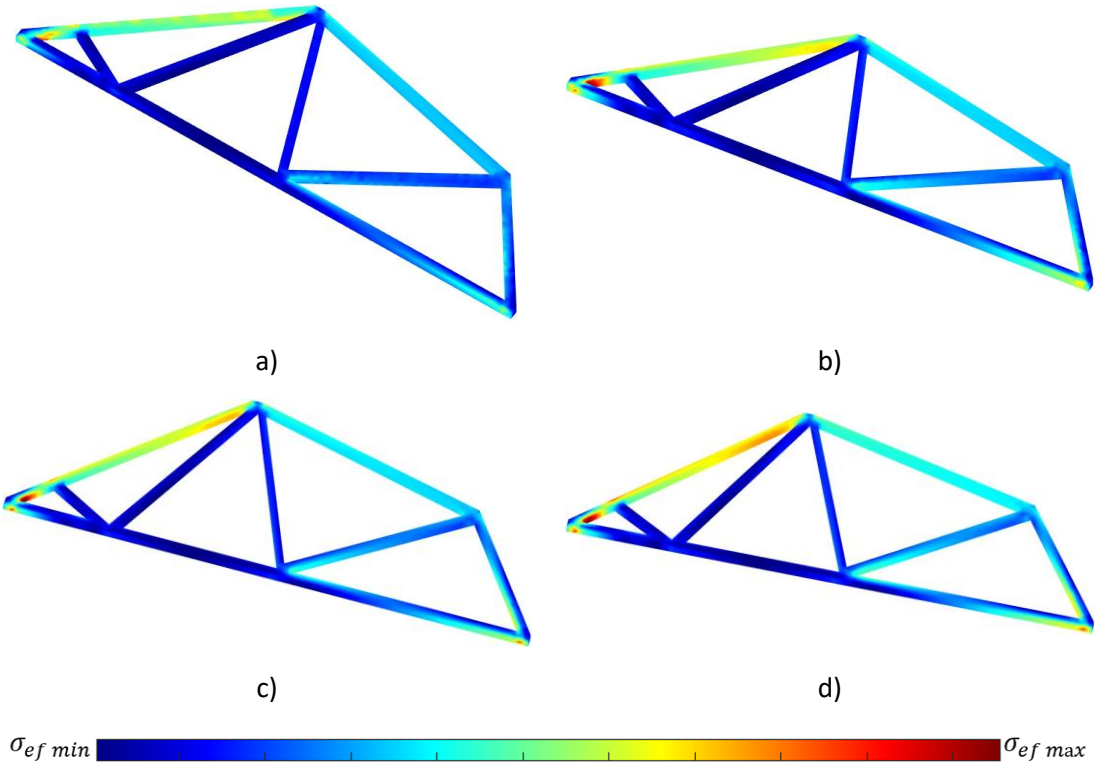

Figure 89. BESO with vertical reactions (Von Misses stress). a) FEM ($\sigma_{ef\ max} = 4.24 \times 10^6\ Pa;\ \sigma_{ef\ min} = 1.24 \times 10^4\ Pa$); b) RPIM ($\sigma_{ef\ max} = 3.86 \times 10^6\ Pa;\ \sigma_{ef\ min} = 1.32 \times 10^4\ Pa$); c) NNRPIM V1 ($\sigma_{ef\ max} = 3.80 \times 10^6\ Pa;\ \sigma_{ef\ min} = 1.39 \times 10^4\ Pa$); d) NNRPIM V2 ($\sigma_{ef\ max} = 3.44 \times 10^6\ Pa;\ \sigma_{ef\ min} = 1.69 \times 10^4\ Pa$)

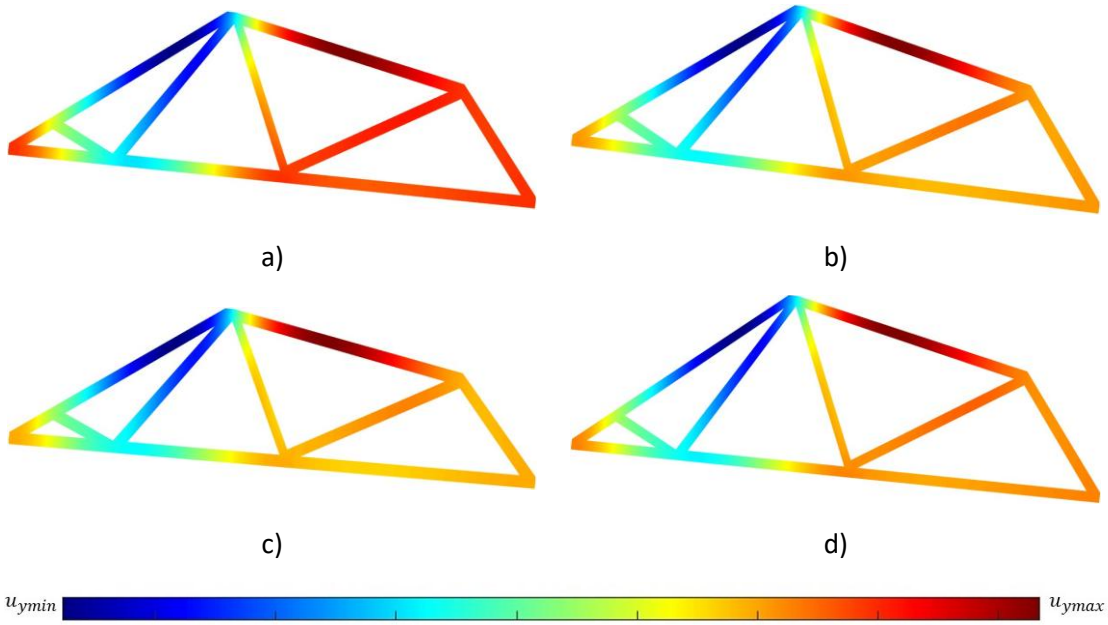

Figure 90. BESO with vertical reactions (Displacements). a) FEM ($u_{max} = 0;\ u_{min} = -2.47 \times 10^{-5} m$); b) RPIM ($u_{max} = 0;\ u_{min} = -2.50 \times 10^{-5} m$); c) NNRPIM V1 ($u_{max} = 0;\ u_{min} = -2.60 \times 10^{-5} m$); d) NNRPIM V2 ($u_{max} = 0;\ u_{min} = -2.40 \times 10^{-5} m$)

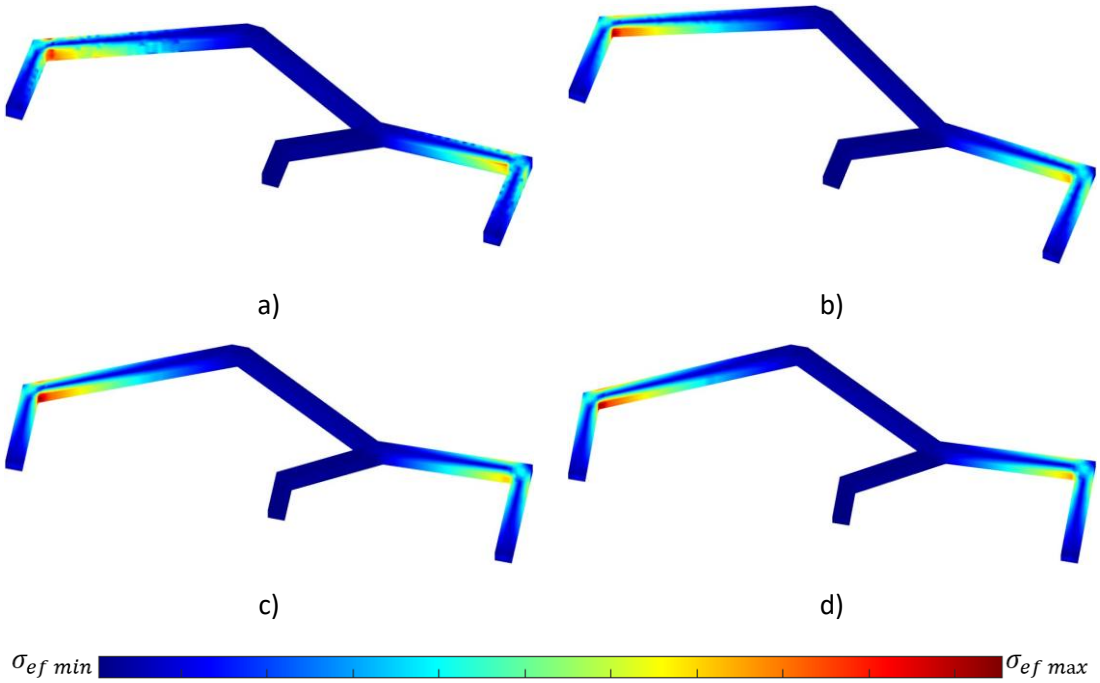

Figure 91. Original suspension system. a) FEM ($\sigma_{ef\ max} = 1.32 \times 10^7\ Pa;\ \sigma_{ef\ min} = 1.44 \times 10^4\ Pa$); b) RPIM ($\sigma_{ef\ max} = 1.44 \times 10^7\ Pa;\ \sigma_{ef\ min} = 1.86 \times 10^4\ Pa$); c) NNRPIM V1 ($\sigma_{ef\ max} = 1.45 \times 10^7\ Pa;\ \sigma_{ef\ min} = 1.68 \times 10^4\ Pa$); d) NNRPIM V2 ($\sigma_{ef\ max} = 1.39 \times 10^7\ Pa;\ \sigma_{ef\ min} = 2.06 \times 10^4\ Pa$)

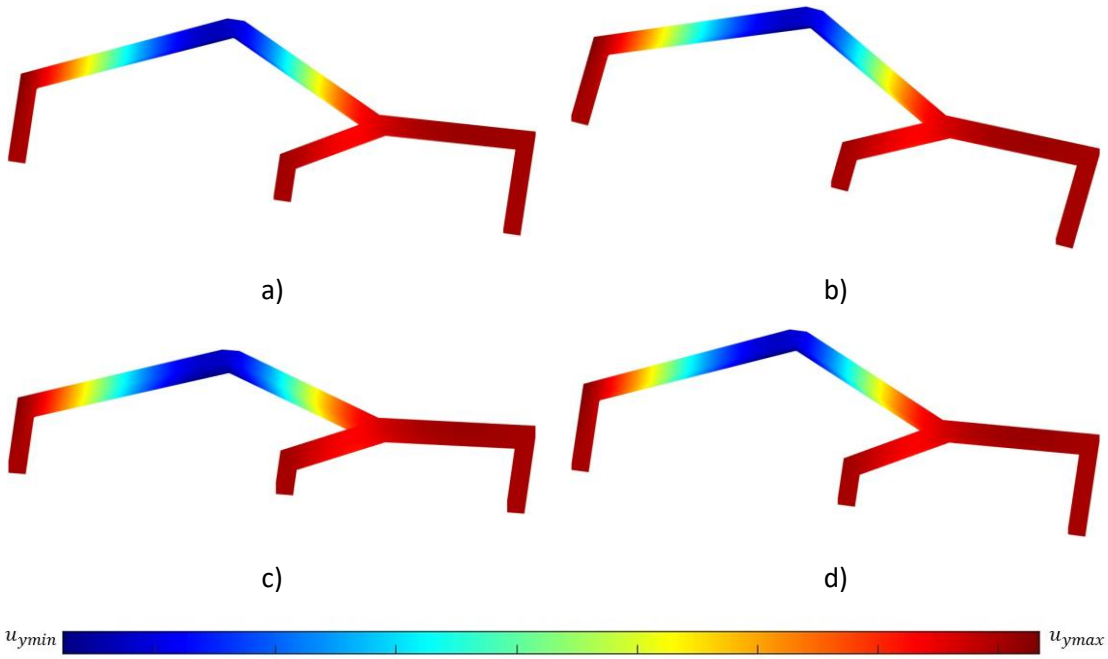

Figure 92. Original 3D suspension system displacements. a) FEM ($u_{max} = 0;\ u_{min} = -3.43 \times 10^{-4} m$); b) RPIM ($u_{max} = 0;\ u_{min} = -3.90 \times 10^{-4} m$); c) NNRPIM V1 ($u_{max} = 0;\ u_{min} = -4.02 \times 10^{-4} m$); d) NNRPIM V2 ($u_{max} = 0;\ u_{min} = -3.85 \times 10^{-4} m$)

As it is possible to observe across Figure 85 to Figure 91, all the 3D structures analysed presented Von Misses stress values that were very similar to those obtained in the 2D analysis. Such confirms that the transition from 2D to 3D modelling did not significantly alter the stress distribution and that the results remain within the same order of magnitude. However, the structures shown in Figure 79 and Figure 87 exhibit a more noticeable difference in Von misses stress values. Overall, despite these variations, the general consistency between the 2D and 3D results reinforces the reliability of the numerical methods used to generate the structures.

Table 8. 3D Suspension systems normalized stiffnesses

STIFFNESS [N/mm/kg]				
Structure	FEM	RPIM	NNRPIM V1	NNRPIM V2
BONE with both reactions	39.72	32.44	29.46	33.31
BONE with vertical reactions	1996.68	2022.67	1996.10	2053.68
BESO with vertical reactions	1916.02	1897.49	1852.98	1935.22
Original structure	70.37	61.78	60.01	62.56

When comparing the normalized stiffness values of the 2D suspension systems with those of the 3D structures (Table 8), the results indicate a strong overall consistency between both analyses. The percentual difference summarised in Table 9 show that, for the majority of the structures, the 3D stiffness values remain within a few percent of the 2D results, typically bellow about 6%. Such confirms that introducing a width parameter to generate 3D structures did not substantially alter the global mechanical response. As it is possible to observe in Table 9, the structures presented in Figure 83 and Figure 91, when analysed with the NNRPIM V2 method, exhibit the highest deviance, whereas Figure 77 and Figure 85 with the RPIM method yields the lower percentual difference when compared to the other studies.

Table 9. Percentual difference between stiffnesses

Difference between stiffnesses [%]				
Structure	FEM	RPIM	NNRPIM V1	NNRPIM V2
BONE with both reactions	2.74	0.15	3.00	3.42
BONE with vertical reactions	5.84	4.38	2.96	3.85
BESO with vertical reactions	5.91	4.61	2.10	2.90
Original structures	1.07	6.10	6.40	7.54

7. Conclusions

This section presents the conclusion of the thesis, summarizing the key findings and insights gained throughout the study. Additionally, the limitations encountered throughout this thesis, as well as suggestions for future work based on the present study, are discussed in the following chapters.

7.1. Conclusions

The focus of this thesis is to structurally optimize the suspensions system of the NASA Perseverance Rover, while validating the efficiency of finite element and meshless methods with the assistance of benchmark examples.

When analysing the evolution of the costs when designing the space rover, it is concluded that nowadays rovers are developed with a low-cost strategy, reflecting technological advances that allow optimized and cheaper designs. Despite this, they are equipped with enhanced technology to meet governmental and military interests. The USA and Russia remain the main leaders in space innovation. The rocker-bogie suspension system is widely preferred due to its efficiency on difficult terrains, often combined with six-wheel mobility systems that ensure manoeuvrability and precise turns thanks to independent power for each wheel. Finally, communication satellites with navigation functions reduce costs by combining two purposes in a single structure.

When comparing the mathematic formulation behind both numerical methods, it is notable that meshless methods present a much more complex formulation. Such was expected due to the fact that meshless methods dispose of the capacity to analyse geometries and engineering problems that involve a higher complexity. Meshless methods also have the capacity to, in the same cell, have a variable number of integration points, in contrast to FEM. Additionally, meshless methods produce much more accurate results and simulations if compared to the results obtained when utilizing FEM, however its computational time is significantly higher.

Overall, all methods used in the benchmark analysis demonstrated convergence toward the analytical solution. However, when analysing vertical displacement, the NNRPIM methods exhibited a faster convergence rate compared to the others. On the contrary, in terms of stress distribution along the beam, the FEM showed superior convergence behaviour. It is worth noting that, although all methods indicated convergence in the 3D analysis, a slight deviation

was observed. This deviation is primarily attributed to the lower nodal density used in the model. Therefore, increasing the number of nodes is essential to achieve more accurate and reliable results. Regarding the structural optimization performed in the benchmark analysis using the Bio-Inspired method, all numerical methods were successfully validated, as the results closely matched the benchmark reference. It is also noteworthy that the NNRPIM variants produced optimized structures that closely mirrored the benchmark configuration. However, this came at the cost of increased computational time, due to the more complex nature of the method. In the context of Bone Remodelling optimization, it was observed that using a higher decrease ratio led to results that more closely aligned with the benchmark examples, with the material removal process being faster therefore reducing the computational time.

For the BESO optimization, both FEM and RPIM benefited from a higher decrease ratio (DR = 0.05), which accelerated convergence and resulted in optimal structures. On the contrary, lower DRs were less effective in these methods. Nonetheless, by modifying the underlying optimization code to increase the iteration interval, it was possible to further enhance the structural performance of some FEM and RPIM cases. In contrast, all NNRPIM variants proved to be robust across different DR values, consistently generating optimal structural configurations. Finally, after analysing the most promising structures, it was concluded that NNRPIM V2 yielded the lowest maximum Von Mises stress, making it the selected method for the structural optimization of the Perseverance Rovers' suspension system.

Regarding the structural optimizations of the Rovers' suspension system, it is important to note that the use of the BONE method proved to be effective in generating an optimized geometry that aligns well with the current system. When considering the input of both horizontal and vertical force components (x and y), the resulting structure closely resembles the existing suspension system. Furthermore, one of the main objectives of this study was to evaluate the potential of generating structurally optimized configurations. By utilizing only vertical reactions, this goal was successfully achieved, as the BONE and BESO methods were able to produce more refined geometries under these constraints. These structures present a more complex internal topology, suggesting an enhanced structural efficiency. Among the configurations, the structure obtained using both horizontal and vertical reaction forces stands out for presenting the lowest maximum Von Mises stress. However, despite this advantage, it exhibits a lower normalized stiffness compared to the original design. On the other hand, the configurations obtained using only vertical reactions show a different scenario. Due to their more robust and complex geometrical arrangements, they achieve significantly higher normalized stiffness values than the original structure. Moreover, when analysing the 3D optimized designs, it was possible to affirm that the change from 2D to 3D did not interfere with the stress values as well the normalized stiffness since the values maintained the same order of magnitude. Such furthermore validates the effectiveness of the methods utilized to generate the structures.

To summarize, every method utilized in the benchmark analysis as well as the rovers' suspension system optimization proved to be capable of efficiently predict the behaviour of a structure under loading conditions in addition to optimizing it. Moreover, the main objectives of this thesis were successfully achieved, being able to validate each method utilized

beforehand as well as optimizing the suspension system into a more complex structure although more mechanically stiff.

7.2. Limitations

Despite the satisfactory results obtained in this study, it is important to acknowledge certain limitations that affect the scope of the finding. One of the main difficulties encountered during the development of this study was the limitation of available hardware resources. Due to these constraints, it was necessary to adopt a coarser mesh arrangement, specifically in the 3D structures, which inevitably reduced the level of detail in the simulations. As a result, conducting a more refined and precise structural analysis was not feasible within the available computational capacity. Moreover, the limited processing power led to longer computational times, especially in simulations involving complex geometries or meshfree methods. These factors posed significant challenges in achieving even better results and constrained the overall scope of the numerical experiments.

7.3. Future works

To further advance knowledge and investigations in future works on the topic presented in this thesis, adjustments to certain parameters, and even a change in the hardware, could significantly enhance the potential for new contributions to the scientific literature. By employing the same methodologies while considering material nonlinearity, it would be possible to develop more sophisticated and realistic structural models. This would result in a more accurate optimization and stress analysis, better reflecting real-world scenarios. Tubes could be employed instead in the elastostatic studies, leading to a more accurate representation the stress distribution due to the fact that the original rover utilizes tubes in its suspension system. Such could also significantly reduce the overall mass of the structure. To achieve a more accurate and realistic study, future works could consider the environmental conditions on Mars. As is well known, Mars is subject to far more extreme temperature variations than those found on Earth. Incorporating these conditions into the analysis would provide a more comprehensive understanding of the structural behaviour and performance of the system, making the results more representative of real operational scenarios. Another potential direction for future work could be to explore the use of different materials and the resulting structural configurations. This difference in material properties and structural behaviour could lead to designs with improved weight to stiffness ratios. Additionally, it could be possible to reveal more cost-effective solutions without compromising the structures' performance under working conditions.

References

[1] M. Macdonald and V. Badescu, *The International Handbook of Space Technology*. Berlin, Heidelberg: Springer Berlin Heidelberg, 2014. doi: 10.1007/978-3-642-41101-4.

[2] Ehlmann, BL, Culbert, CJ, Fraeman, and al, 'Revolutionizing Access to the Mars Surface: A Strategy: Frequent, Affordable & Bold', no. March, 2022, doi: 10.7907/d1sm-mj77.

[3] M. D. G. J. R. French, 'SPACE VEHICLE DESIGN', 2nd editio., American Institute of Aeronautics and Astronautics, 2004, p. ISBN: 1563475391.

[4] Q. Zhao *et al.*, 'An Overview of the Applications of Earth Observation Satellite Data: Impacts and Future Trends', *Remote Sens.*, vol. 14, no. 8, p. 1863, Apr. 2022, doi: 10.3390/rs14081863.

[5] X. Wang, G. Wu, L. Xing, and W. Pedrycz, 'Agile Earth Observation Satellite Scheduling Over 20 Years: Formulations, Methods, and Future Directions', *IEEE Syst. J.*, vol. 15, no. 3, pp. 3881–3892, Sep. 2021, doi: 10.1109/JSYST.2020.2997050.

[6] C. Han, Y. Gu, G. Wu, and X. Wang, 'Simulated Annealing-Based Heuristic for Multiple Agile Satellites Scheduling Under Cloud Coverage Uncertainty', *IEEE Trans. Syst. Man, Cybern. Syst.*, vol. 53, no. 5, pp. 2863–2874, May 2023, doi: 10.1109/TSMC.2022.3220534.

[7] G. Ai, H. Shi, H. Wu, Z. Li, and J. Guo, 'The principle of the positioning system based on communication satellites', *Sci. China Ser. G Physics, Mech. Astron.*, vol. 52, no. 3, pp. 472–488, Mar. 2009, doi: 10.1007/s11433-009-0065-6.

[8] B. Wilcox *et al.*, 'Robotic vehicles for planetary exploration', in *Proceedings 1992 IEEE International Conference on Robotics and Automation*, IEEE Comput. Soc. Press, 1992, pp. 175–180. doi: 10.1109/ROBOT.1992.220266.

[9] Y. Gao and S. Chien, 'Review on space robotics: Toward top-level science through space exploration', *Sci. Robot.*, vol. 2, no. 7, Jun. 2017, doi: 10.1126/scirobotics.aan5074.

[10] A. Seeni, B. Schfer, and G. Hirzinger, 'Robot Mobility Systems for Planetary Surface Exploration – State-of-the-Art and Future Outlook: A Literature Survey', in *Aerospace Technologies Advancements*, no. January, InTech, 2010. doi: 10.5772/6930.

[11] A. Seeni, B. Schafer, B. Rebele, and N. Tolyarenko, 'Robot Mobility Concepts for Extraterrestrial Surface Exploration', in *2008 IEEE Aerospace Conference*, IEEE, Mar. 2008, pp. 1–14. doi: 10.1109/AERO.2008.4526237.

[12] A. Singh and P. K. Jain, 'A Study on Rocker-Bogie Suspension for a Planetary Rover

Prototype', *Int. J. Adv. Res. Innov.*, vol. 8, no. 3, pp. 27–39, 2020, doi: 10.51976/ijari.832006.

[13] A. Bogatcbev, V. Koutcberenko, M. Malenkov, and S. Matrossov, 'Developments of Track Locomotion Systems for Planetary Mobile Robots', *IFAC Proc. Vol.*, vol. 37, no. 7, pp. 153–158, Jun. 2004, doi: 10.1016/S1474-6670(17)32140-7.

[14] L. Bruzzone and G. Quaglia, 'Review article: locomotion systems for ground mobile robots in unstructured environments', *Mech. Sci.*, vol. 3, no. 2, pp. 49–62, Jul. 2012, doi: 10.5194/ms-3-49-2012.

[15] P. Fiorini, 'Ground mobility systems for planetary exploration', in *Proceedings 2000 ICRA. Millennium Conference. IEEE International Conference on Robotics and Automation. Symposia Proceedings (Cat. No.00CH37065)*, IEEE, 2000, pp. 908–913. doi: 10.1109/ROBOT.2000.844164.

[16] H. Benaroya, 'The lunar environment', in *Building Habitats on the Moon*, Cham: Springer International Publishing, 2018, pp. 42–84. doi: 10.1007/978-3-319-68244-0_3.

[17] J. Zakrajsek *et al.*, 'Exploration Rover Concepts and Development Challenges', in *1st Space Exploration Conference: Continuing the Voyage of Discovery*, Reston, Virigina: American Institute of Aeronautics and Astronautics, Jan. 2005, pp. 258–280. doi: 10.2514/6.2005-2525.

[18] G. Sharma, J. Gautam, and S. Gurusideswar, 'Material selection and its characterization for Mars environment and a study on full field strain analysis', in *AIP Conference Proceedings*, 2021, p. 020045. doi: 10.1063/5.0036265.

[19] X. You *et al.*, 'A review of research on aluminum alloy materials in structural engineering', *Dev. Built Environ.*, vol. 17, no. March, p. 100319, Mar. 2024, doi: 10.1016/j.dibe.2023.100319.

[20] B. Harris, 'Engineering Composite Materials', in *High Voltage Power Network Construction*, Institution of Engineering and Technology, 2018, pp. 689–703. doi: 10.1049/PBPO110E_ch26.

[21] Z. S. Toor, 'Space Applications of Composite Materials', vol. 8, no. 524, Journal of Space Tech nology, 2018, pp. 65–70. doi: 10.1201/b17135-4.

[22] J. J. Wijker, *Spacecraft Structures*. Berlin, Heidelberg: Springer Berlin Heidelberg, 2008. doi: 10.1007/978-3-540-75553-1.

[23] 'https://www.nasa.gov'. Accessed: Oct. 25, 2024. [Online]. Available: https://science.nasa.gov/mission/mars-2020-perseverance/rover-components/

[24] J. Belinha, *Meshless Methods in Biomechanics*, vol. 16. in Lecture Notes in Computational Vision and Biomechanics, vol. 16. Cham: Springer International Publishing, 2014. doi: 10.1007/978-3-319-06400-0.

[25] J. Belinha, 'Multiscale Analysis of Sandwich Beams with Polyurethane Foam Core: A Comparative Study of Finite Element Methods and Radial Point Interpolation Method', *Materials (Basel).*, vol. 17, no. 18, p. 4466, Sep. 2024, doi: 10.3390/ma17184466.

[26] O. Askour, S. Mesmoudi, and B. Braikat, 'On the use of Radial Point Interpolation Method (RPIM) in a high order continuation for the resolution of the geometrically nonlinear elasticity problems', *Eng. Anal. Bound. Elem.*, vol. 110, no. April 2019, pp. 69–79, Jan. 2020, doi: 10.1016/j.enganabound.2019.09.015.

[27] J. Belinha, 'Extending the Natural Neighbour Radial Point Interpolation Meshless Method to the Multiscale Analysis of Sandwich Beams with Polyurethane Foam Core', *Appl. Sci.*, vol. 14, no. 20, p. 9214, Oct. 2024, doi: 10.3390/app14209214.

[28] J. Belinha, L. M. J. S. Dinis, and R. M. Natal Jorge, 'The analysis of the bone remodelling around femoral stems: A meshless approach', *Math. Comput. Simul.*, vol. 121, pp. 64–94, 2016, doi: 10.1016/j.matcom.2015.09.002.

[29] D. C. Gonçalves, J. D. F. Lopes, R. D. S. G. Campilho, and J. Belinha, 'The Radial Point Interpolation Method combined with a bi-directional structural topology optimization algorithm', *Eng. Comput.*, vol. 38, no. 6, pp. 5137–5151, 2022, doi: 10.1007/s00366-021-01556-8.

[30] W. K. Liu, S. Li, and H. S. Park, 'Eighty Years of the Finite Element Method: Birth, Evolution, and Future', *Arch. Comput. Methods Eng.*, vol. 29, no. 6, pp. 4431–4453, Oct. 2022, doi: 10.1007/s11831-022-09740-9.

[31] A. Hrennikoff, 'Solution of Problems of Elasticity by the Framework Method', *J. Appl. Mech.*, vol. 8, no. 3, pp. 169–175, Sep. 1941, doi: 10.1115/1.4009210.

[32] M. J. TURNER, R. W. CLOUGH, H. C. MARTIN, and L. J. TOPP, 'Stiffness and Deflection Analysis of Complex Structures', *J. Aeronaut. Sci.*, vol. 23, no. 9, pp. 805–823, Sep. 1956, doi: 10.2514/8.3664.

[33] 'https://www.sciencedirect.com'. Accessed: Oct. 24, 2024. [Online]. Available: https://www.sciencedirect.com/search?qs=Finite elements methods&tak=%22Finite element method%22&date=2014-2024

[34] V. P. Nguyen, T. Rabczuk, S. Bordas, and M. Duflot, 'Meshless methods: A review and computer implementation aspects', *Math. Comput. Simul.*, vol. 79, no. 3, pp. 763–813, Dec. 2008, doi: 10.1016/j.matcom.2008.01.003.

[35] V. G. Patel and N. V. Rachchh, 'Meshless method – Review on recent developments', *Mater. Today Proc.*, vol. 26, no. xxxx, pp. 1598–1603, 2020, doi: 10.1016/j.matpr.2020.02.328.

[36] S. N. Atluri and S. Shen, 'The Meshless Local Petrov-Galerkin (MLPG) Method: A Simple & Less-costly Alternative to the Finite Element and Boundary Element Methods', *Adv. Comput. Math.*, vol. 3, no. 1–2, pp. 11–51, Jul. 2002, doi: 10.3970/cmes.2002.003.011.

[37] 'https://www.sciencedirect.com'. Accessed: Oct. 24, 2024. [Online]. Available: https://www.sciencedirect.com/search?qs=meshless methods&tak=meshless methods&date=2021-2024

[38] M. Contreras, C.-Y. Peng, D. Wang, and J.-S. Chen, 'Determining Wheel-Soil Interaction Loads using a Meshfree Finite Element Approach Assisting Future Missions with Rover Wheel Design', in *AIAA Modeling and Simulation Technologies Conference*, Reston, Virigina: American Institute of Aeronautics and Astronautics, Aug. 2012, pp. 1–10. doi: 10.2514/6.2012-4562.

[39] J. B. Johnson *et al.*, 'Discrete element method simulations of Mars Exploration Rover wheel performance', *J. Terramechanics*, vol. 62, pp. 31–40, Dec. 2015, doi: 10.1016/j.jterra.2015.02.004.

[40] M. Zou *et al.*, 'Design and mechanical behavior evaluation of flexible metal wheel for crewed lunar rover', *Acta Astronaut.*, vol. 176, pp. 69–76, Nov. 2020, doi: 10.1016/j.actaastro.2020.06.010.

[41] E. Łazuka and M. Łazuka, ‘APPLICATION OF ANSYS IN TEACHING FEM ON THE EXAMPLE OF A LOADED MARS ROVER CHASSIS’, *Adv. Sci. Technol. Res. J.*, vol. 10, no. 32, pp. 269–274, Dec. 2016, doi: 10.12913/22998624/66682.

[42] M. Pierzgalski, P. Ptak, D. Cekus, and K. Sokół, ‘Modeling and Stress Analysis of a Manipulator Mounted on a Mars Rover’, *Procedia Eng.*, vol. 177, pp. 121–126, 2017, doi: 10.1016/j.proeng.2017.02.199.

[43] J. Cepeda-Rizo and D. Tuman, ‘Mars 2020 Rover Laser Power Supply Thermomechanical Analysis’, in *2018 IEEE 68th Electronic Components and Technology Conference (ECTC)*, IEEE, May 2018, pp. 1371–1374. doi: 10.1109/ECTC.2018.00209.

[44] J. J. Nunez-Quispe, J. Lleren-Sernaque, and E. Lara-Chavez, ‘Mechanical Design of a ROVER prototype for Exploration tasks on Mars: Structural and Transient Dynamics simulation analysis’, in *2021 IEEE MIT Undergraduate Research Technology Conference (URTC)*, IEEE, Oct. 2021, pp. 1–5. doi: 10.1109/URTC54388.2021.9701623.

[45] W. Guo *et al.*, ‘Configuration design and numerical analysis of a Martian dust storm simulation wind tunnel for Mars airplanes and rovers’, in *2016 IEEE International Conference on Advanced Intelligent Mechatronics (AIM)*, IEEE, Jul. 2016, pp. 1497–1502. doi: 10.1109/AIM.2016.7576982.

[46] R. Bardera *et al.*, ‘Experimental and Numerical Characterization of the Flow Around the Mars 2020 Rover’, *J. Spacecr. Rockets*, vol. 55, no. 5, pp. 1136–1143, Sep. 2018, doi: 10.2514/1.A34217.

[47] X. Huang and Y. M. Xie, *Evolutionary Topology Optimization of Continuum Structures*, 1st ed. Wiley, 2010. doi: 10.1002/9780470689486.

[48] ‘https://www.tsm-titanium.com/’. Accessed: May 22, 2025. [Online]. Available: https://www.tsm-titanium.com/info/the-comprehensive-guide-to-ti-6al-4v-103118495.html

[49] ‘https://asm.matweb.com/’. Accessed: May 22, 2025. [Online]. Available: https://asm.matweb.com/search/specificmaterial.asp?bassnum=mtp642

Declaração de Integridade

Declaro ter conduzido este trabalho académico com integridade. Não plagiei ou apliquei qualquer forma de uso indevido de informações ou falsificação de resultados ao longo do processo que levou à sua elaboração.

Declaro que o trabalho apresentado neste documento é original e de minha autoria, não tendo sido utilizado anteriormente para nenhum outro fim.

Declaro ainda que tenho pleno conhecimento do Código de Conduta Ética do P.PORTO.

NOME: João Pedro Basílio Silva

ISEP, Porto, 10 de janeiro de 2025